Numerical and experimental analysis of check valves in fuel systems

Master Thesis of

cand. mach M.Sc. Jörg Baumgartner

at the Department of Mechanical Engineering
Lehrstuhl für mobile Arbeitsmaschinen
and the ANDREAS STIHL AG & Co. KG

Reviewer:	Prof. Dr.-Ing. M. Geimer
Advisor:	Dipl.-Ing. Danilo Engelmann
Second advisor:	Dipl.-Ing. Giovanni Leccese

February 1st, 2017 – May 31st, 2017

Karlsruher Institut für Technologie
Institut für Fahrzeugsystemtechnik
Teilinstitut Mobile Arbeitsmaschinen
Rintheimer Querallee 2
D-76131 Karlsruhe

I declare that I have developed and written the enclosed thesis completely by myself, and have not used sources or means without declaration in the text.

. . . . . .
Jörg Baumgartner
Karlsruhe, 31.05.2017

Non-disclosure notice

This work contains confidential data about ANDREAS STIHL AG & Co. KG, Waiblingen, as well as their affiliates.
Within five years after the submission of this work, it shall not be made accessible for third parties in the purpose of information, dissemination and publication. Reproduction and copying, also in part, are not permitted. All copies of this work are to be kept in places inaccessible to the public. Exceptions require the written permission of ANDREAS STIHL AG & Co. KG.
Due to confidentiality, some results, values or other information are suppressed in this version.

Abstract

The objective of this thesis is to obtain a profound understanding about the effects in check valves of carburetors and to integrate it in a one-dimensional analogous model. To review the model quality, a validation is being performed. For this purpose the results of 1D-simulations are compared to appropriate 3D-simulations. This shows a good qualitative and quantitative agreement. In addition, the validation is performed by means of measurements on a pulsation test bed. This reveals major deviations between measurements and 1D-simulation. Discussing potential reasons for these deviations leads to the presentation of a new concept for the test bed.

Keywords: 1D-simulation, check valve, validation, pulsation test bed

Abstracto

El objetivo de esta tesis es generar una profunda comprensión acerca del funcionamiento de las válvulas de retención de carburadores e integrarla en un modelo análogo unidimensional. Con el fin de garantizar la calidad del modelo, los resultados de simulaciones 1D y 3D, serán comparados. Este método permitirá incrementar la exactitud de los resultados tanto desde el punto de vista cualitativo así también como cuantitativo. Además, mediciones generadas en un banco de pruebas de pulsación serán usadas para validar el modelo. Considerables desviaciones entre las mediciones y la simulación 1D serán evidenciadas por medio de este procedimiento de medición. La discusión acerca de las posibles causas de estas desviaciones conduce a la presentación de un nuevo concepto para el banco de pruebas.

Palabras clave: 1D-simulación, válvula de retención, validación, banco de pruebas de pulsación

Kurzfassung

Das Ziel der vorliegenden Arbeit ist es, ein tieferes Verständnis über die Vorgänge in Rückschlagventilen von Vergasern zu erlangen und dies in einem eindimensionalen Ersatzmodell festzuhalten. Zur Überprüfung der Modellqualität wird eine Validierung durchgeführt. Dazu findet ein Vergleich der Ergebnisse aus 1D-Simulationen und entsprechenden 3D-Simulationen statt. Dabei zeigt sich eine gute qualitative und quantitative Übereinstimmung zwischen beiden Berechnungen. Außerdem werden für die Validierung Messungen an einem Pulsationsprüfstand durchgeführt. Hierbei werden allerdings große Unterschiede zwischen den Messungen und den Ergebnissen der 1D-Simulation deutlich. Die Diskussion potentieller Gründe für diese Abweichungen führt zur Vorstellung eines veränderten Konzeptes für den Prüfstand.

Schlagwörter: 1D-Simulation, Rückschlagventil, Validierung, Pulsationsprüfstand

Contents

Nomenclature

Latin symbols

A	[m^2]	Area
E	[J]	Energy content
F	[N]	Force
$\hat{F}$	[N]	Amplitude of Force
$\dot{Q}$	[W]	Heat flow
T	[s]	Period
S	[m^2]	Surface
V	[m^3]	Volume
$\dot{V}$	[$\frac{m^3}{s}$]	Volume flow
a	[$\frac{m}{s^2}$]	Acceleration
c	[$\frac{N}{m}$]	Spring stiffness
d	[$\frac{kg}{s}$]	Damping Coefficient
f	[Hz]	Frequency
f	[N/kg]	Specific volume force
g	[$\frac{m}{s^2}$]	gravitational acceleration
h	[m]	Height
k_{SF}	[-]	Oscillation frequency factor
m	[kg]	Mass
$\dot{m}$	[$\frac{kg}{s}$]	Mass flow
$\vec{n}$	[m]	Normal vector
p_{stat}	[Pa]	Static pressure
p_{dyn}	[Pa]	Dynamic pressure
p_{total}	[Pa]	Total pressure

$\hat{p}$	[Pa]	Amplitude of pressure
r	[m]	Radius
t	[s]	Time
v	$[\frac{\mathrm{m}}{\mathrm{s}}]$	Velocity
x, y, z	[m, m, m]	Cartesian coordinates
$\dot{x}$	$[\frac{\mathrm{m}}{\mathrm{s}}]$	Velocity in x-Direction
$\ddot{x}$	$[\frac{\mathrm{m}}{\mathrm{s}^2}]$	Acceleration in x-Direction

Greek symbols

α	[°]	Crank angle
ξ	[-]	Pressure loss coefficient
η	$[\frac{\mathrm{kg}}{\mathrm{m\,s}}]$	dynamic viscosity
λ	[m]	Wavelength
ν	$[\frac{\mathrm{m}^2}{\mathrm{s}}]$	Kinematic Viscosity
π	[-]	Pi
ρ	$[\frac{\mathrm{kg}}{\mathrm{m}^3}]$	Density
ϕ	[rad]	Phase angle

Abbreviations

const.	constant
rpm	Revolutions per minute

List of Figures

List of Tables

1 Introduction

STIHL's portfolio includes a large number of hand-held tools. Many of these are operated with two-stroke ottomotors, due to various reasons. The lowest possible overall weight of the machine is to be aspired as the user has to carry it during use. With their low specific weight or the high power density, the two-stroke ottomotor provides significant advantages over the four-stroke engine [Pis02a].

Hand-held tools also require reliable operation regardless of the operating position. For this reason, it must be ensured that an ignitable mixture is formed and fed into the cylinder in every operating position. A decisive component for fulfilling this criterion is the carburetor. Membrane gasifiers are particularly suitable, since they are less sensitive to changes in the position than, for example, float gasifiers [Bas15]. The fuel metering and mixture formation takes place here by means of gas-dynamic or flow-mechanical effects. The carburetor is a self-regulating system which, with an ideal design, does not require any additional components or sensors to determine the necessary fuel quantity.

Some effects in the carburetor are still not fully understood despite the advanced state of research at STIHL. For example, in the case of some check valves a drop in the amount of fuel supplied at the start-up rotational speed is not yet explained. The same effect was detected when the machine is operated upside down. In order to better analyze such observations and predict the effects, a reliable model of these check valves is required. With regard to the saving of time and costs, the proportion of simulations compared to experimental investigations in the development and optimization is to be increased. The aim of this master thesis is therefore to complete and validate a one-dimensional model, which considers the essential effects and thus serves as the basis for the development of optimally designed check valves.

Such a model is implemented in the one-dimensional STIHL internal simulation code DAVE+. A validation of the 1D model is necessary to determine and evaluate the model quality. Comparison parameters are the pressure profiles, the mass flow through the valve

and the movement of the valve disc. Here, stationary and periodic-stationary cases are considered.

On the one hand, the validation takes place on the basis of 3D simulations with ANSYS Fluent. For this purpose, the 1D model is matched geometrically and mechanically to the 3D model. In this matching, the 1D model is throttled with the aid of pressure loss coefficients in such a way that it takes into account three-dimensional effects such as sudden cross-sections or directional changes due to pressure losses and reproduces the mass flow and the pressure distribution of the 3D simulation. This adjustment is performed in a stationary and periodic-stationary manner. This is followed by the validation of the reconciled model by means of a further periodic-stationary 3D simulation.

On the other hand, the check valves are tested experimentally. For this purpose, measurements are carried out on a test bed which reconstructs the pressure conditions at check valves in the carburetor. These measurements are also compared with corresponding calculations of the 1D model for validation purposes.

2 Principles

This chapter describes the operation principle of internal combustion engines. The two-stroke engines are then dealt with more precisely in order to explain the function of a carburetor. In the closer inspection of carburetors the focus is on the check valves to create a corresponding basis for the further work. Within the second part of this chapter, the theoretical principles of fluid dynamics are shown so that the basic functionality of STIHL's one-dimensional in-house flow solver DAVE+ can be described.

2.1 Internal Combustion Engines

An internal combustion engine is a machine which convert chemical energy into mechanical energy. In this process, the energy chemically bound in the fuel is released by a combustion process and converted into thermal energy. By taking advantage of the resulting gas dynamic effects, this can be converted by the engine to mechanical energy in the form of a rotational movement of the crankshaft [KF06]. Combustion engines can be categorized on the basis of various aspects. For a detailed overview of the categorization of combustion engines, see Merker [MS12] and van Basshuysen [Bas15]. An important aspect is the distinction in the nature of the working procedure. Basically two-stroke and four-stroke engines are distinguished. Since only two-stroke gasoline engines are of interest for the present work, only these are treated in more detail below.

2.1.1 Two-Stroke Gasoline Engines

In the case of a two-stroke engine, the compression and expansion stages, which are shown schematically in Figures 2.1a and 2.1b, are distinguished. From top dead center (TDC) the piston moves downwards in the direction of bottom dead center (BDC) during the *expansion stroke*. This is done by burning the fuel/air mixture (red arrows in Figure 2.1a) in the combustion chamber. The combustion is triggered by a spark generated by the spark plug. Pressure and temperature in the combustion chamber are strongly increased, which leads to a pressure force moving the piston towards the bottom dead center. During the

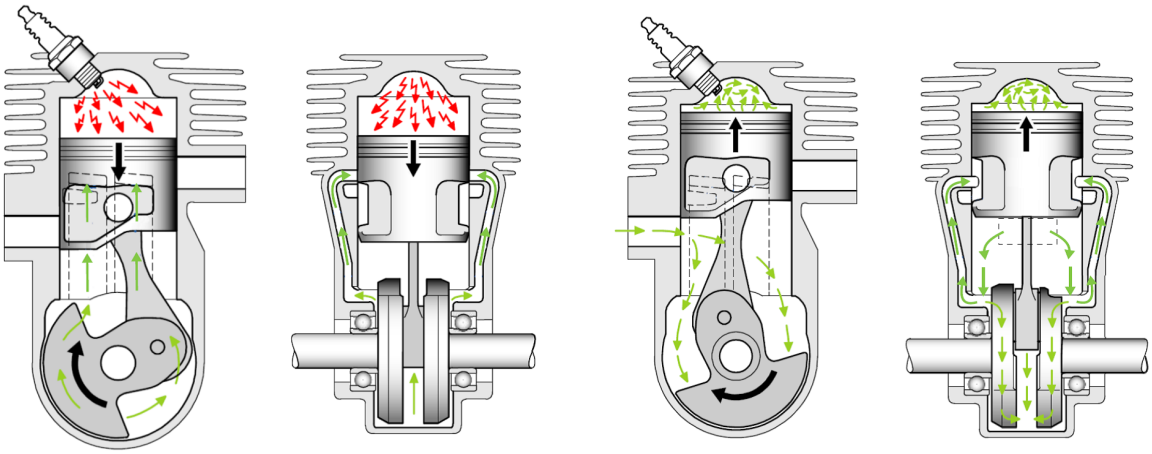

(a) Expansion stroke

(b) Compression stroke

Figure 2.1: Strokes of a two-stroke gasoline engine [Lag16]

downward movement, the piston performs work on the crankshaft [Pis02b]. In doing so, it first sweeps the inlet slot and closes it, so that no fresh fuel/air mixture (green arrows) can flow from the intake channel into the crankcase. This time is shown in Figure 2.1a. By the downward movement of the piston, the pressure in the closed crankcase increases and the mixture in the crankcase is precompressed. The piston then sweeps the outlet slot and releases it, whereby the combusted gas flows out of the combustion chamber and a pressure decrease in the combustion chamber occurs. Afterwards the piston opens the transfer ports. Due to the pressure difference between crankcase and combustion chamber, the precompressed fresh gas flows from the crankcase into the combustion chamber via the released transfer channels.

The compression stroke starts from the bottom dead center. First, the transfer ports are closed before the piston closes the outlet of the combustion chamber. With the upward movement, the piston increases the pressure of the fresh fuel/air mixture present in the combustion chamber. At the same time, the upward movement creates a negative pressure in the still closed crankcase until the inlet is swept by the piston. When the inlet is opened, fresh mixture is sucked into the crankcase. This time is shown in figure 2.1b. In the top dead center, the ignition spark is then ignited and a new working cycle begins.

The charge exchange takes place between these working cycles by the flushing process when the piston is near the bottom dead center and thus releases the outlet. The exhaust gases are pushed out of the combustion chamber because of the high pressure. In addition, the fresh fuel/air mixture, which flows into the combustion chamber via the transfer ports, pushes the exhaust gas (black arrows) out of the combustion chamber. The aim here is to displace all the exhaust gas from the combustion chamber. In order to ensure this without

a fresh mixture leaving the combustion chamber unburnt even before the outlet is closed, stratified scavenging is used. As shown in figure 2.2, the principle is that the transfer ports are first filled with pure fresh air (blue arrows) instead of fresh fuel/air mixture. This fresh air enters the piston pockets via a seperate channel from the surrounding area and is preloaded there. When opening the transfer ports (Figure 2.3), it displaces the exhaust gas from the combustion chamber and does not cause any losses when leaving the combustion chamber before closing the outlet (Figure 2.4).

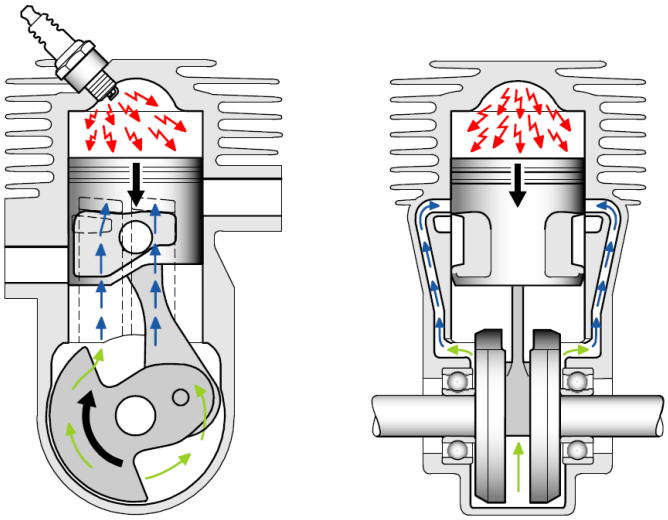

Figure 2.2: Pure fresh air in the transfer ports following [Lag16]

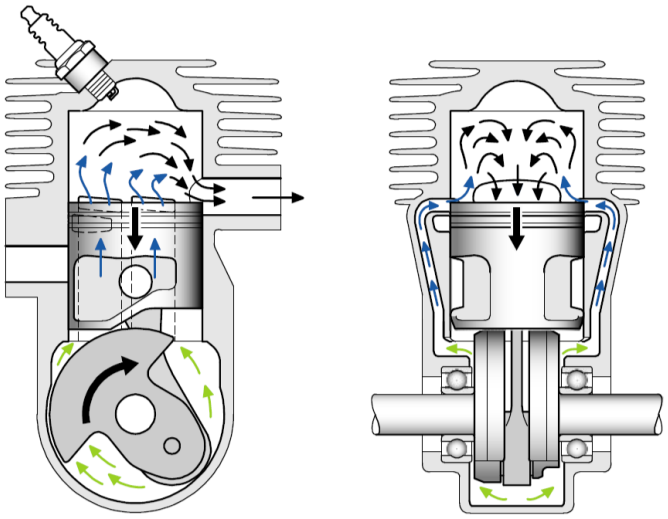

Figure 2.3: Fresh air entering combustion chamber following [Lag16]

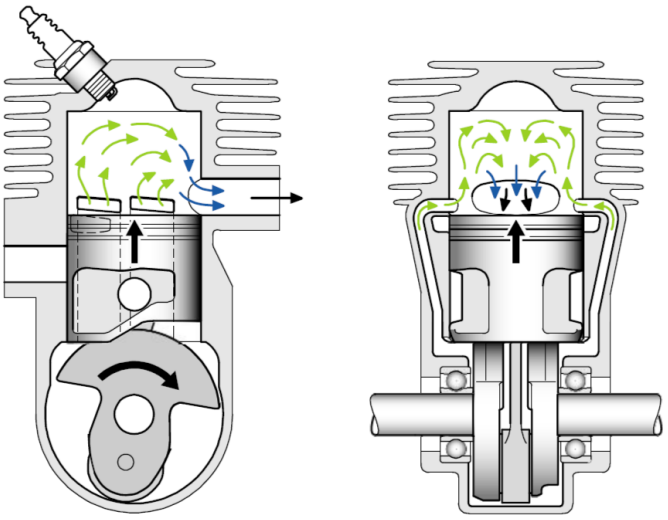

Figure 2.4: Pushing out exhaust gases following [Lag16]

2.1.2 Carburetor

The mixture formation in STIHL devices takes place by means of membrane carburetors. These are hardly sensitive to changes in position with respect to gravity [Bas15], what makes them suitable for mobile working devices like chainsaws or hedge trimmers. Figure 2.5 shows the schematic structure of such a carburetor.

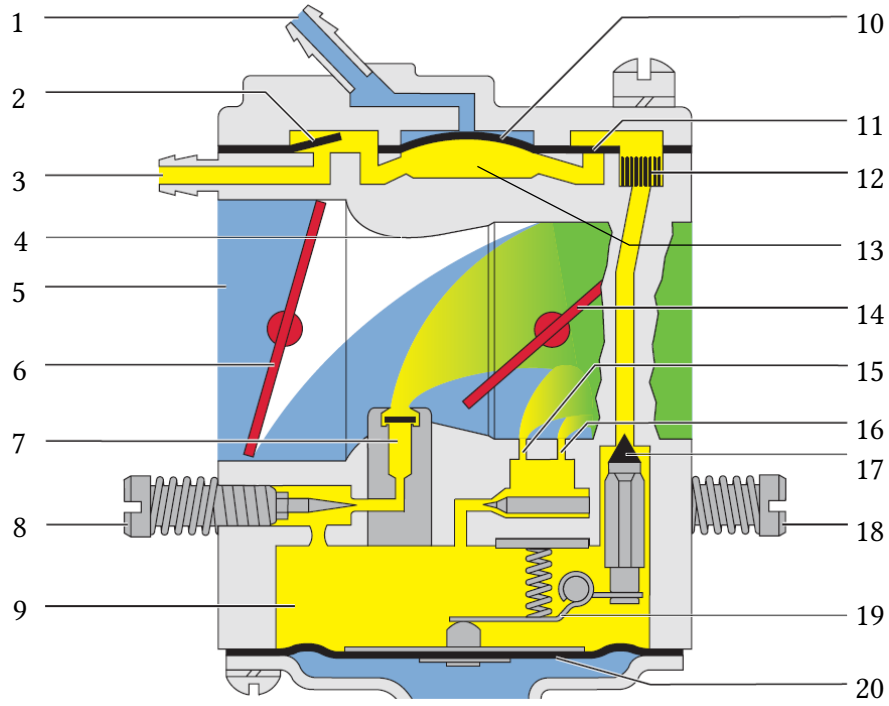

Figure 2.5: Schematical configuration of a carburetor following [Han12]

During the compression stroke of the engine, the intake port is opened and the volume of the crankcase is being increased by the upward movement of the piston. This results in a flow from left to right in the intake duct (5) in figure 2.5 into the direction of the crankcase. By means of a venturi-shaped constriction (4) in the intake duct, a local pressure change is generated in the region of the main nozzle (7). This can be described in simplified form with the continuity equation and the Bernoulli equation for friction-free, incompressible fluids [Jr17] [BE05]:

$$\dot{m} = \rho v A = const. \tag{2.1}$$

$$p_{total} = const. = p_{stat} + p_{dyn} = p + \rho g z + 1/2 \rho v^2 \tag{2.2}$$

According to equation 2.1 and quasi-one-dimensional view, the flow in the narrowest cross-section $A_{Venturi}$ has a higher velocity than the intake channel with the cross-section

$A_{intakeduct} > A_{Venturi}$. Since the total pressure is constant according to equation 2.2, the dynamic pressure proportion increases as the velocity increases, while the static fraction decreases. The lower static pressure causes the fuel to be sucked into the intake duct. The quantity of fuel supplied thus depends on the negative pressure formed, which is coupled to the air mass flow in the intake duct.

The fuel is initially supplied via a pump membrane (Figure 2.5, 10), to which the pressure oscillations of the crankcase are transmitted via an air-filled pulse duct (1). During the compression stroke, the pressure in the pulse duct is lower than the pressure in the yellow coloured fuel channel, whereby the pump membrane bulges outwards and increases the volume of the pump chamber (13). The exhaust valve (11) closes as the intake valve (2) opens. The fuel flows from the tank into the pump chamber from the fuel intake port (3). During the expansion stroke the pump membrane bulges inwards due to the overpressure in the impulse channel and thus displaces fuel located in the pump chamber. In this case, since the intake valve closes and the exhaust valve opens, the fuel is supplied into the control chamber (9) via the fuel sieve (12) and the fuel channel.

There is a constant pressure in the control chamber. This is kept constant by means of a control system consisting of a regulating needle, a control lever and a spring, and is thus decoupled from the engine speed as well as piston-dependent pressure pulses. The regulating membrane (20) delimits the control system from the environment. It bulges inwards when fuel is sucked from the control chamber into the intake duct. By this movement, the control lever (19) is raised, which in turn pushes the regulating needle (17) downwards and thus opens the transition from the fuel channel to the control chamber. The inflowing fuel compensates for the volume change caused by the membrane curvature, so that the control chamber pressure settles to a value. This control chamber pressure is essentially dependent on the spring strength and the lever ratios. By means of this control system, the carburetor is a self-regulating system which supplies a defined quantity of fuel to a certain air mass flow.

The fuel/air ratio can be adjusted via the main adjusting screw (8) and the idle adjusting screw (18). The outflow cross section to the main nozzle or to the idle nozzle (16) and bypass nozzles (15) is increased by tighten the relevant screw, as a result of which more fuel is supplied to the nozzles and the mixture becomes enriched. Correspondingly, the loosening of the adjusting screws causes a leaner mixture. The throttle flap (14), which is connected to the gas lever, serves as the control element. Its position determines the flow

area through the intake duct and thus the amount of air sucked in and the fuel supplied. This allows the user to continuously adjust the desired motor load. The possible operating points are briefly explained in the following, since they have a great influence on the behavior of the check valves considered in the work.

2.1.2.1 Choke/Starting the engine

In order to ensure a reliable starting of the engine, the fuel-air mixture is enriched for a short time. This is achieved by the choke flap (Figure 2.5, 6), which is located in the intake duct at the main nozzle and operates according to the same principle as the throttle flap. In figure 2.5 the start process is shown. When the throttle flap is open, the choke flap is almost completely closed, which in combination with the negative pressure generated in the crankcase leads to an increased pressure difference between the control chamber and the intake duct. The state in which the control chamber side pressure is higher than the pressure in the intake duct is referred to as *positive pressure gradient* in the following. A *negative pressure gradient* accordingly describes the state in which the control chamber side pressure is lower than the pressure in the intake duct. Due to the high positive pressure gradient caused by the opened choke flap, more fuel is sucked into the intake duct via the main nozzle and the mixture becomes rich. The choke flap is only closed for starting the engine and is open for all other operating points.

2.1.2.2 Idling operation

The engine speed in idling operation of STIHL engines is about [redacted]* rpm. As shown in Figure 2.6, during the idle state the throttle flap (1) is closed.

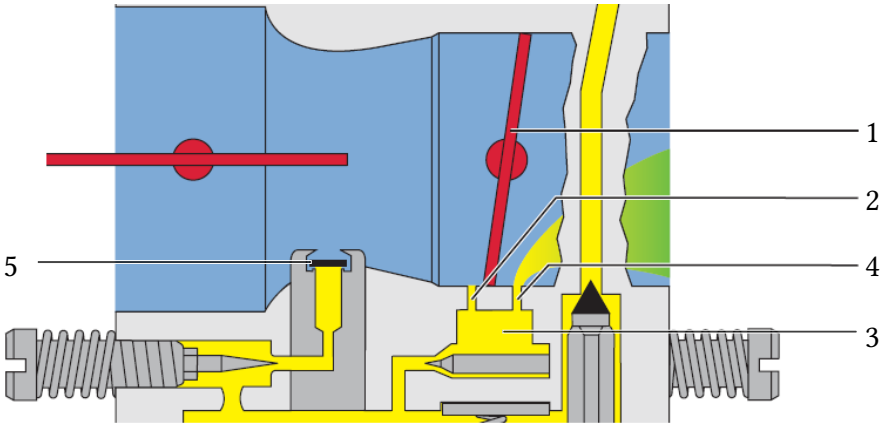

Figure 2.6: Idling operation of a carburetor following [Han12]

*Information surpressed due to confidentiality

A negative pressure in the crankcase is therefore applied behind the throttle flap. Because of the cross-section of the intake duct, which is closed by the throttle flap, the air evades into the bypasses (2), via which it enters the mixing chamber (3) and blends with fuel. The mixture then flows into the intake duct and to the crankcase via the idle discharge bore (4). Due to the very low air mass flow in the intake duct during idling operation, almost ambient pressure is at the main nozzle. Since the control chamber pressure is approximately [redacted]* mbar below the ambient pressure, a negative pressure gradient is applied across the check valve of the main nozzle, as a result of which the valve disc (5) closes the valve.

2.1.2.3 Full load operation

Figure 2.7 shows the carburetor during full load operation.

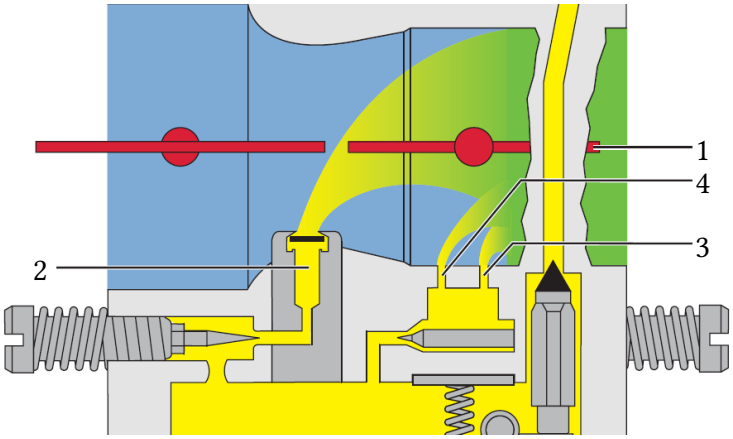

Figure 2.7: Carburetor during full load operation following [Han12]

The throttle flap (1) is fully open. Since it now has hardly any throttling effect, the air throughput is very high. With the associated high velocity of the air flow, a low static pressure is applied to the main nozzle (2) as well as to the idle (3) and bypass nozzles (4). As a result, a large positive pressure gradient is applied to all the nozzles and the fuel throughput is maximized. Approximately [redacted]* % of the fuel supplied in this operating condition is introduced via the main nozzle and [redacted]* % by the idle nozzles. The full load speed of STIHL engines varies according to the type and model of the device being operated, but is usually in the range between [redacted]* rpm and [redacted]* rpm.

*Information surpressed due to confidentiality

2.1.2.4 Partial load operation

When the operating state changes from idle to full load, the partial load range is passed through, which includes all the rotational speeds between the idle and the full-load rotational speed. When accelerating, the throttle valve is opened broader. Figure 2.8 shows an operating state in the partial load near the idle.

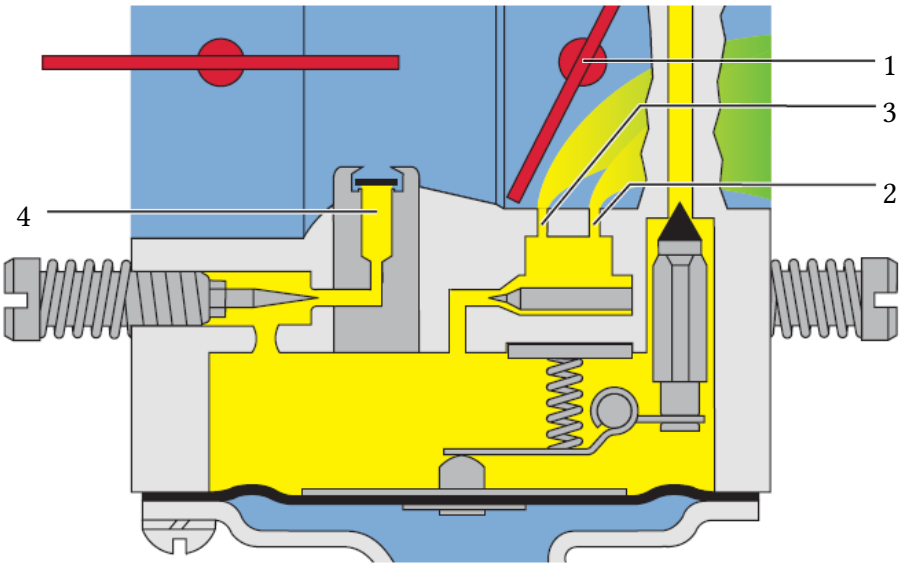

Figure 2.8: Carburetor in partial load operation following [Han12]

The throttle flap (1) is only slightly open. The throttle effect is large at the idle (2) and bypass nozzles (3), here the crankcase pressure is applied. Because of the large negative pressure, a lot of fuel is sucked through these nozzles. On the other hand, at the main nozzle (4) almost ambient air pressure is caused by the position of the throttle flap, which means a negative pressure gradient. Thus, the check valve in the main nozzle is closed and no fuel is sucked through it. In the higher partial load range the throttle flap is opened further, which leads to an increasing air mass flow and positive pressure gradient at the main nozzle. This opens the check valve and leads to a fuel mass flow from the control chamber through the main nozzle into the intake duct. During the expansion stroke of the engine, however, an overpressure is present in the venturi with regard to the control chamber. In order to prevent the inflow of air into the control chamber in the event of a negative pressure gradient, check valves are used in the main nozzle and the idle nozzle.

2.1.3 Check Vales

Check valves are used to prevent unwanted backflow of a fluid. Thus, a fluid movement against the targeted flow direction must ensure that the valve closes. This can, for example, be implemented by a rotatably mounted flap. This principle is used in the carburetor at the exhaust valve in the fuel channel, as shown in Figure 2.9.

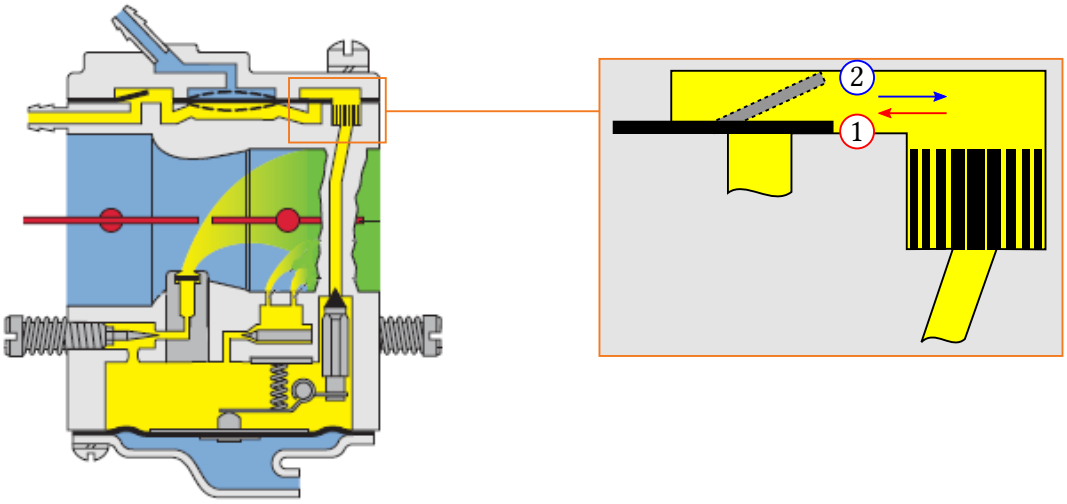

Figure 2.9: Check valve in the fuel channel

In the case of a positive flow direction (blue arrow), the flow pushes the flap upwards (2) and releases the flow cross-section. Applying a negative flow direction (red arrow), the flap is pressed against the valve seat (1) and the flow cross-section is closed. An alternative design of a check valve is shown in the main nozzle of a carburetor, as shown in Figure 2.10.

In this case, a disc is installed in such a way that it opens a cross-section in the case of a positive direction of flow (blue arrow) and closes with a negative flow direction (red arrow).

For a closer look, Figure 2.11 shows the section through such a check valve. A circular disc (2) is mounted freely movably between a retainer (1) and the valve seat (3). The fuel is at a constant pressure of approximately $p_{controlchamber}$, while downstream the valve a pressure osciallation is applied, generated by the crank chamber. The present work deals exclusively with these check valves.

If the disc is located on the valve seat, the valve is closed and no fuel flows from the control chamber into the intake duct. To seal as good as possible, the valve seat is designed circular so that a line contact with the disc is obtained. This position is for the further work defined as the zero point of the disc movement as Figure 2.11 shows. As soon as the

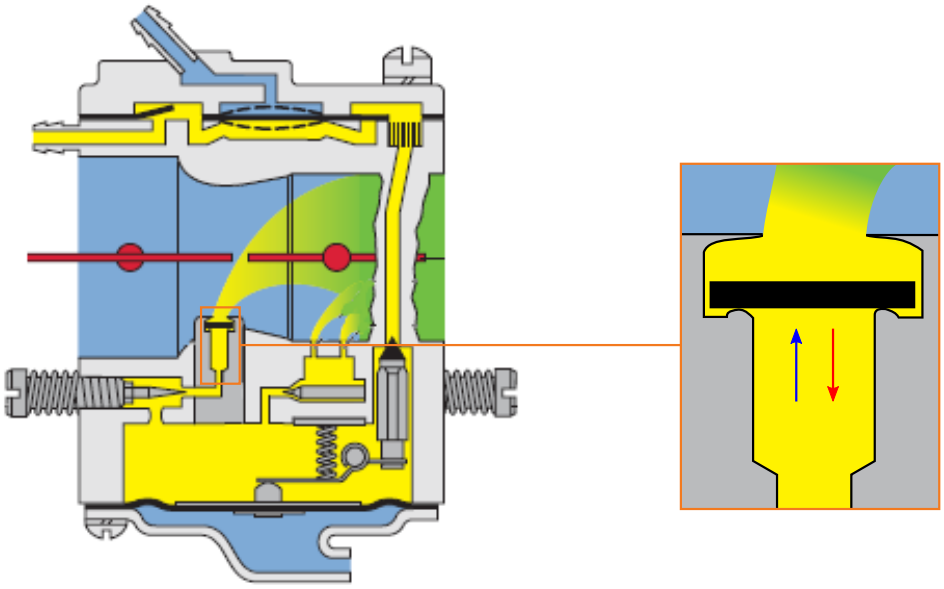

Figure 2.10: Check valve in the main nozzle of a carburetor

disc rises from the valve seat, a flow cross-section is released and the fluid flows into the direction of the intake duct. The retainer defines the maximum stroke of the disc. When the disc is pressed against the retainer, the maximum flow cross-section is opened. This allows the geometry of the retainer, which is sketched in Figure 2.12 three-dimensionally with the disc fully open. Illustrative stream lines of three fluid particles are indicated by way of illustration.

In principle, a large number of forces act on the disc, which cause and influence its movement. The pressure force which is the result of the pressure difference upstream and downstream of the disc is decisive for the movement. In the case of a positive pressure gradient, the pressure force acts on the plate towards the retainer, in the event of a negative pressure drop towards the valve seat. To ensure that the disc follows the flow as good as possible and thus closes so quickly in case of a return flow that no air enters the control chamber, the plate is made of light plastic. With the small mass, the inertial force of the disc is small. Furthermore, the graviation force acts on the disc, which is also negligibly small because of the low mass. In addition, vibrational influences and secondary effects from the two-phase flow between fuel and air influence the predominantly pressure-controlled movement of the disc.

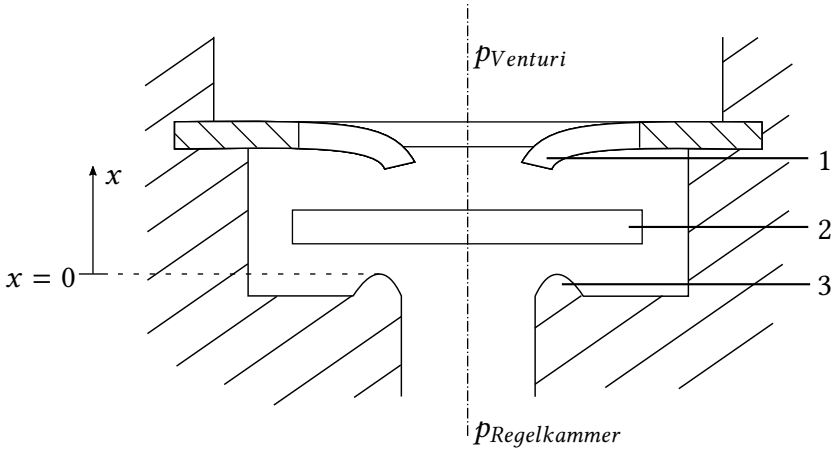

Figure 2.11: Section through a check valve

2.2 One-dimensional simulation using DAVE+

The 1D simulation is implemented in the DAVE+ (Dynamic Analysis of Virtual Engines) program developed by STIHL. With this software the complete one-dimensional conservation equations can be solved and thus complex systems can be simulated relatively simply, quickly and cost-effectively. In contrast to time-consuming and CPU-intensive 3D simulations, comprehensive parameter studies can be performed very quickly in one-dimensional computations. The basic structure and function of the C++ based program are briefly described in the following [RK13].

2.2.1 Structure and operating principles

Different types of text files form the basis of a model calculation in DAVE+. Their structure and links are shown in Figure 2.13.

Thus, the actual network of the system is defined in the template file <*template-name*>.tpl with the links and functions. The generic structure of all STIHL motors is contained in a template file. Model parameters such as geometric variables are stored in a model file <*model-name*>.mdl. The model files are used to transfer engine-specific variables to the template. If a variable is assigned a numeric value both in the template and in the model, the value from the model file is used for the calculation. From the template and the model file, an input file <*input-name*>.inp is generated by the Dave-Input-Generator. With this input file DAVE+ finally calculates the results and represents a specific STIHL machine by combining the generic setup and the specific motor variables. Instead of generating the input file through template and model, it can also be written directly for simple 1D

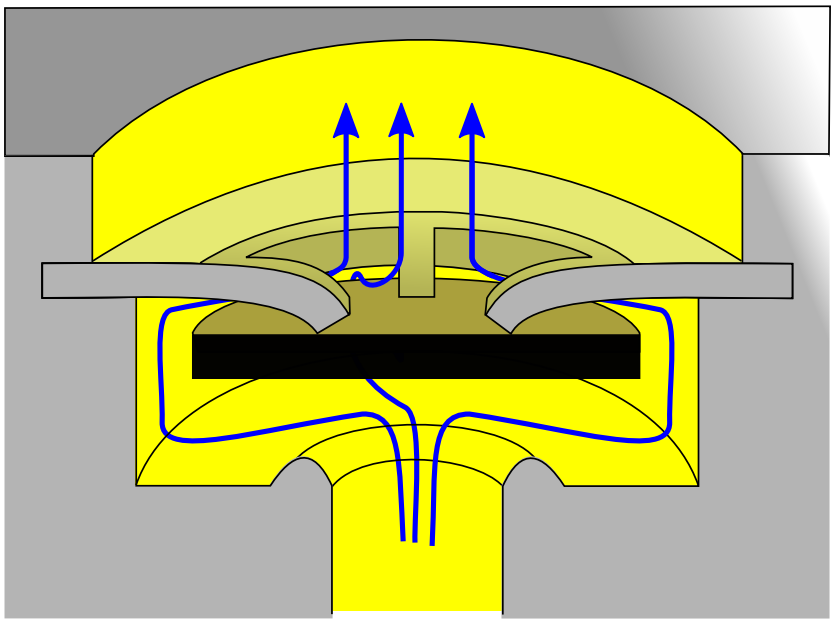

Figure 2.12: 3D-Sketch of a fully open check valve

simulations. In addition, there is an include file <*include-name*>.inc which simplifies parameter studies. You can define any number of values for maximum two independent variables, which override the values in the model file. DAVE+ then calculates all possible combinations of thes variable values.

Basically, DAVE+ creates the following files for a compilation run: <*name*>.proto is a log file in ASCII format which contains the input values and the interconnections of the elements. The binary file <*name*>.restart contains the state vector of the last time step so that the computation can be resumed at this point. All calculation results of the defined memory period are stored in binary form in the <*name*>.all.gz file. Furthermore, you can use the AUSWERTUNG function to specify in the template what exactly should be saved. In this way, the user can, for example, specify that a file is created for each element which contains all or only selected state variables for each point in time.

The tools **davePlot** and **dave2d**, also developed by STIHL, allow visualization of the calculation results. Alternatively, conventional data processing programs can also be used for the evaluation and visualization of the result files. The program **daveLink** is suitable to display the interconnection of the elements from the input file. This program has also been used to create 2.14.

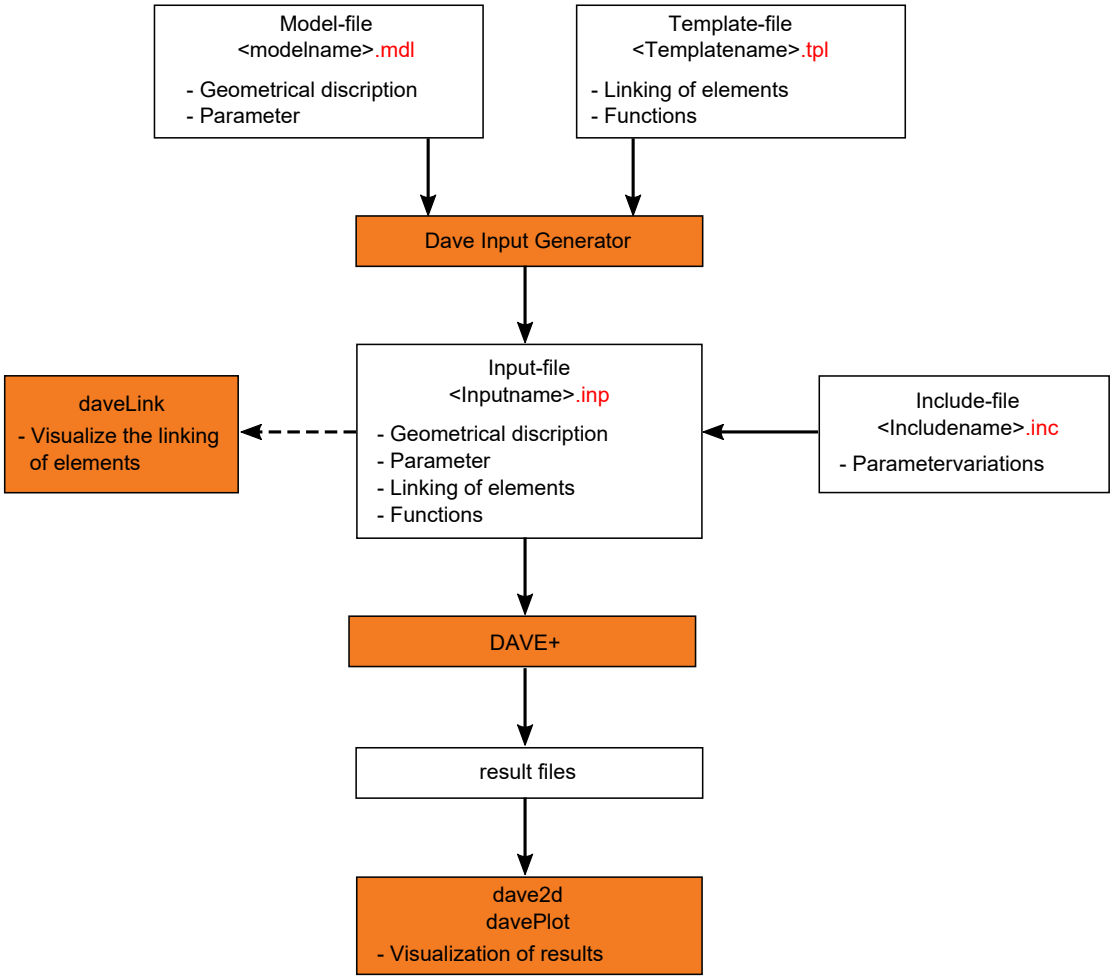

Figure 2.13: File structure in DAVE+ following [Lec14]

2.2.2 Elements und interconnections

Basically, a system in DAVE+ consists of a network of pipes, volumes and boundaries. Figure 2.14 shows a very simple example of such a network with two boundary conditions (*OFT* and *outflow*), three pipes (*Messpunkt*, *Schlauch* and *Schlauch1*) and one volume (*Behaelt*).

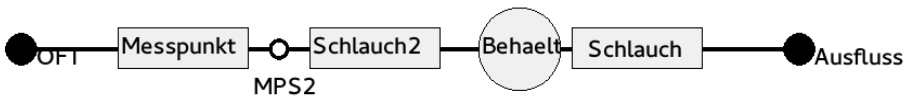

Figure 2.14: Display of a network in DaveLink

Pipes can be connected to volumes, boundaries or other pipes. Furthermore, a pipe can be divided into cells to achieve a higher resolution. For pipes, a variety of properties

such as name, number of cells or entry and exit cross-section can be defined. Multi-dimensional flow effects, such as the pressure loss caused by vortex formation due to changes of the cross section, can be taken into account in the 1D simulation in the form of pressure loss coefficients.

Volumes can only be connected to pipes, not to other volumes or to boundaries. The number of connected pipes is not limited. As for pipes, different properties such as name, volume and state variables such as pressure and temperature can also be defined for volumes.

Boundary conditions (short: Boundaries) are the constant or variable state variables at the boundaries of the system. The boundary values themselves are not affected by the calculation. Boundary conditions can only be connected to pipes, not to volumes.

The size of the volumes and the cross-sections of pipes can be constant or defined as a function. State variables for the definition of functions are the time and the crank angle. The boundaries can also be constant or time-/crank-angle-dependent. Since DAVE+ is a one-dimensional view, geometric variables such as the cross-section or volumes are to be viewed as functional variables rather than as multi-dimensional forms.

Furthermore, the interaction of flow and mechanics can be modeled by elements such as bending bars or elastic walls. For example, an **elastic wall** must be switched between two elements. Possible connection elements are volumes and boundaries. The elastic wall between two volumes corresponds to a second order motion equation, which is composed of the inertia, the damping and restoring force of the wall as well as the pressure force of adjacent volumes and other external forces:

$$m\ddot{x} + d\dot{x} + cx = (p_{Vu} - p_{Vl}) \cdot A + F_{Ext} \tag{2.3}$$

Where m is the mass, d is the damping constant, c is the stiffness, and A is the area of the wall. When the wall moves between an upper volume V_u and a lower volume V_l, the size of both volumes also changes according to the motion x of the wall. Therefore, the volume change for the upper volume is calculated as follows:

$$\begin{aligned} V_{u,1} &= V_{u,0} + Ax \\ \dot{V}_{u,1} &= V_{u,0} + A\dot{x} \\ \ddot{V}_{u,1} &= V_{u,0} + A\ddot{x} \end{aligned} \tag{2.4}$$

A flow through a system is described by the variables pressure p, velocity v and temperature T. The result files contain the mean values of these and other derived variables for each element or for each cell. The type of fluids in the system can also be defined and is usually composed of air, fuel and exhaust gas for the simulation of engine systems. Alternatively, water can also be used as an incompressible medium for test purposes. For a compressible fluid, in addition to the conservation equations for mass, energy and momentum, the ideal gas equation and the caloric equilibrium must also be calculated. For incompressible media only the conservation equations for mass, energy and momentum are necessary. Since this work is only dealing with systems with fuel in the case of the carburetor or with water in the case of the test bench, only these conservation equations are now addressed.

2.2.3 Conservation equations and implementation in DAVE+

Mass conservation is considered using the continuity equation. This means that mass can neither be produced nor destroyed. Accordingly, the mass change in a control volume is always the sum of the inflowing and outflowing masses. Formula (2.5) describes this in an integral form for a time-variable control volume $V(t)$ [SA06].

$$\frac{\mathrm{d}}{\mathrm{d}t}\int_{V(t)}\rho\,\mathrm{d}V = \int_{S(t)}\rho(u_S - u)n_S\,\mathrm{d}S \tag{2.5}$$

Where $S(t)$ is the time-varying surface of the control volume, ρ the density of the fluid, v_S the velocity on the surface, and n_S the outward normal vector. Equation (2.5) is calculated by DAVE+ in discretized form. As an example, the control volume V shown in Figure 2.15 is given.

The dashed line segments represent an interface i with the corresponding density ρ_i, the sign s_i, the velocity v_i, and the connection cross-section A_i. Within the control volume the mean pressure p, mean density ρ and the mean temperature T are assigned. By using $\dot{m}_i = \rho_i s_i w_i A_i$ the discrete continuity equation after transposing the equation results in

$$\frac{\mathrm{d}\rho}{\mathrm{d}t} = -\frac{s_d\sum_{i=1}^{n}\dot{m}_i + \rho\frac{dV}{dt}}{V}. \tag{2.6}$$

A detailed derivation can be found in [RK13]. In addition to the mass, the energy is also a conservation parameter. In a closed system, the total energy remains constant over time. However, it may exist in various forms, such as kinetic energy or heat. In an open system, the temporal energy change can be expressed as the sum of heat flux $\dot{Q}$ across the system boundaries and the volume change work $\dot{W}$:

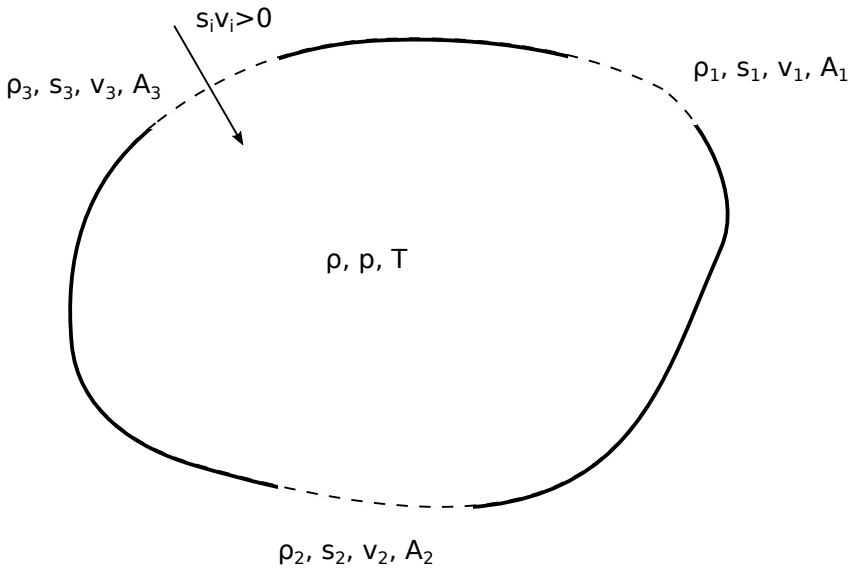

Figure 2.15: Control volume for the conservation of mass following [RK13]

$$\frac{\mathrm{d}E}{\mathrm{d}t} = \dot{Q} + \dot{W} \tag{2.7}$$

The momentum equation in a differential, one-dimensional form for each cross-section through which the mean velocity v passes results in

$$\frac{\partial w}{\partial t} = -\frac{1}{\rho}\frac{\partial p}{\partial x} - w\frac{\partial w}{\partial x} + \frac{f}{\rho} + g + \frac{1}{\rho}\frac{\partial p_v}{\partial x} \tag{2.8}$$

Where f is a volume force and g an acceleration by external forces. The last summand takes into account the pressure losses p_V by friction effects. In order to be able to calculate the momentum equation discreetly more easily, this is first converted to

$$\frac{\partial w}{\partial t} = -\frac{1}{\rho}\frac{\partial (p - p_v)}{\partial x} - \frac{1}{2}\frac{\partial w^2}{\partial x} + \frac{f}{\rho} + g \tag{2.9}$$

The discretization is illustrated by the example of a through-flow aperture, which is shown schematically in figure 2.16 [RK13].

In this case the equation (2.9) leads to the discrete form

$$\frac{\mathrm{d}w_c}{\mathrm{d}t} = \frac{1}{\rho_c}\left[-\frac{(p_r + p_{v,r}) - (p_l + p_{v,l})}{\delta x_{lr}} + f\right] - \frac{1}{2}\frac{w_r^2 - w_l^2}{\delta x_{lr}} + g \tag{2.10}$$

with the pressure losses

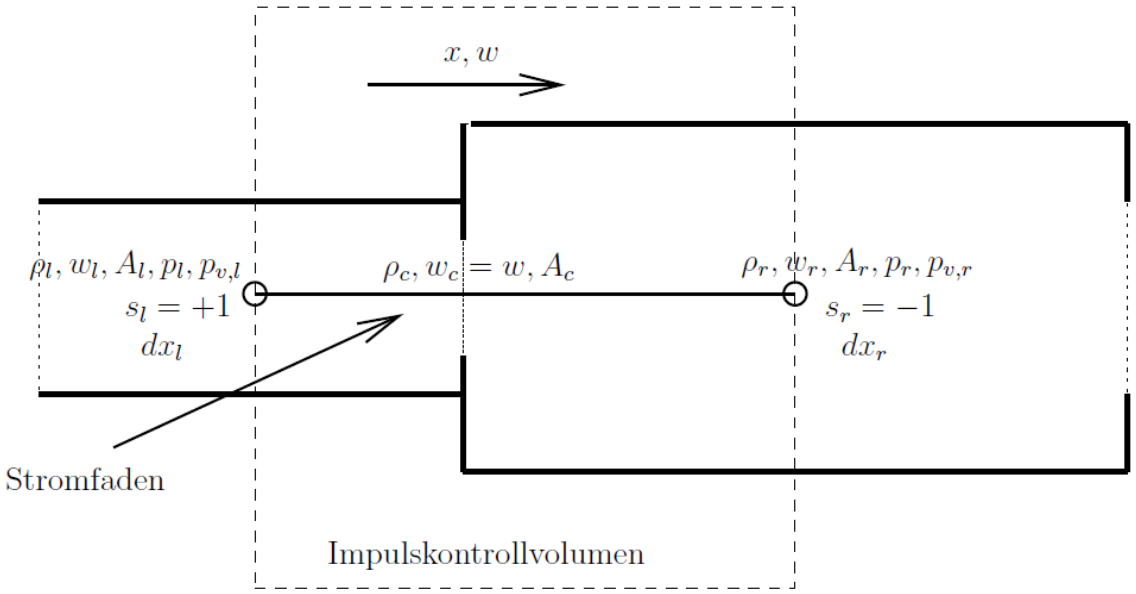

Figure 2.16: Flow through a aperture following [RK13]

$$p_{v,r} = \begin{cases} 0 & \text{für } w_c < 0 \\ \xi \frac{\rho_c}{2} w_c^2 & \text{für} w_c \geq 0 \end{cases} \tag{2.11}$$

and

$$p_{v,l} = \begin{cases} \xi \frac{\rho_c}{2} w_c^2 & \text{für } w_c < 0 \\ 0 & \text{für} w_c \geq 0 \end{cases} \tag{2.12}$$

Applying those to equation (2.10) leads to the discrete, one-dimensional momentum conservation equation

$$\frac{\mathrm{d}w_c}{\mathrm{d}t} = \frac{1}{\rho_c}\left[-\frac{p_r - p_l}{\delta x_{lr}} + f\right] - \frac{1}{2}\frac{w_r^2 - w_l^2 - sign(w_c)\xi w_c^2}{\delta x_{lr}} + g \tag{2.13}$$

For a stationary flow through the aperture ($f = 0, g = 0, w_l = 0, w_r = 0, dw_c/dt = 0$) this equation is reduced to the known formula for the pressure loss

$$p_l - p_r = sign(w_c)\xi \frac{\rho_c}{2} w_c^2 \tag{2.14}$$

3 One-dimensional Model

One-dimensional modeling of systems has the advantage of being able to provide estimates for optimization and design in a short time, in contrast to time- and cost-intensive multi-dimensional simulations. This is particularly beneficial with regard to extensive parameter studies in the development process. This chapter presents the one-dimensional model of the check valve in DAVE+, which is investigated in further the work.

3.1 Structure of the model

Figure 3.1 shows the geometry of the investigated check valve. The retainer (1), the disc (2) and the valve seat (3) can be seen in addition to the shaded edges of the valve, which are referred to as *valve wall*. The zero point for the disc motion x is defined at the valve seat. The disc position $x = 0$ thus corresponds to the closed state of the valve and an opening movement of the plate corresponds to a movement in the positive x direction.

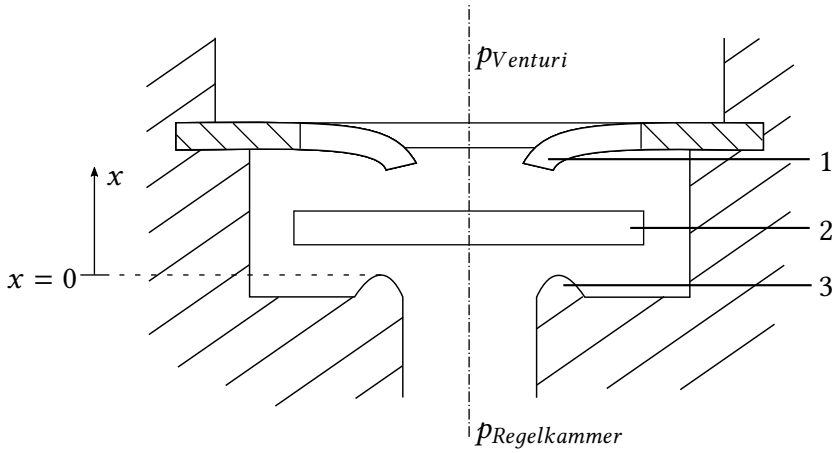

Figure 3.1: Cross-section of the check valve

The division of the flow through the valve into the elements and the resulting structure in DAVE+ is shown in Figure 3.2.

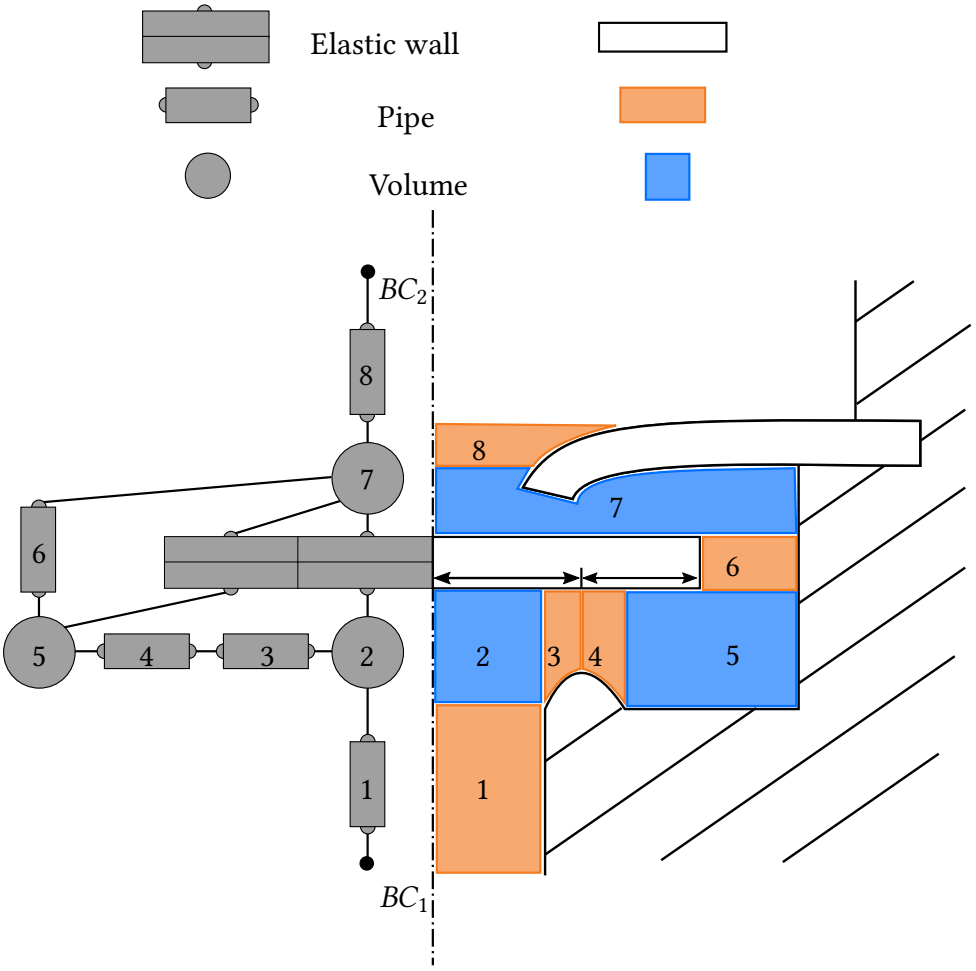

Figure 3.2: Geometrical (right) and structural division in DAVE+ (left)

A boundary condition BC_1 specifies a constant pressure which corresponds to the pressure in the control chamber. This is followed by a pipe *Duese* (1), which is divided into three sections and maps the cross-sections of the valve feed. This is where the actual valve starts. First, the fluid flows through the *Ventilraum1* (2). This section is modeled as volume, since the accumulation of the flow on the disc corresponds to a complete impulse loss. In Dave+, the impulse loss during the inflow into a volume element is specified by definition. Thus, a volume best represents the flow path shown in Figure 3.2. If the disc is not in contact with the valve seat, the valve is open and fluid can pass from *Ventilraum1* to the *Ventilraum2* (5) via the two pipes *Dichtung1* (3) and *Dichtung2* (4). The disc is modeled in DAVE+ using two elastic walls that are coupled. The background for dividing the disc into two parts is the more precise discretization of the pressure conditions on the disc. The inner disc part has the same radius as the valve seat, the outer disc part adjoins

thereto and is limited outside by the outer radius of the disc. Thus, on this side of the disc, the pressure $p_{Ventilraum1}$ causes a compressive force on the inner part of the disc, the pressure $p_{Ventilraum2}$ effects a compressive force on the outer part of the disc. Due to the high pressure drop at the constriction between *Dichtung1* and *Dichtung2*, $p_{Ventilraum1}$ and $p_{Ventilraum2}$ can be very different from each other.

The coupling of the two elastic wall parts is realized by very stiff spring connections. This ensures a harmonic disc movement in which the two wall parts are at each time at the same position x. The disc can move freely between the two stops on the retainer and the valve seat. In the following, the state *"fully opened"* indicates the position of the disc on the retainer and the state *"closed"* the position of the disc on the valve seat. Both impacts are mapped with an artificial function. If the disc reaches the maximum stroke x_{max} or the smallest possible stroke $x_{min} = 0$, this artificial function is activated. It acts as a spring-damper system and brakes the disc movement so that x_{max} and x_{min} are not exceeded or fallen below. Since the pipe cross-section at the valve seat is dependent on the disc position x, it is modeled as a controlling cross-section with a function $Q(x)$. It results from the circumference of the valve seat multiplied by the current disc stroke. From *Ventilraum2*, the fluid enters the *Ventilraum3* (7) via another pipe *VentilB* (6). For reasons of symmetry, compressive forces on the disc perpendicular to the x direction are substantially equal and therefore neglected. The resulting compressive forces on the disc parts can be calculated according to equation (3.1).

$$\begin{aligned} F_{pressure,inner} &= (p_{Ventilraum1} - p_{Ventilraum3}) \cdot A_{inner} \\ F_{pressure,outer} &= (p_{Ventilraum2} - p_{Ventilraum3}) \cdot A_{outer} \end{aligned} \tag{3.1}$$

Ventilraum3 is again connected to the pressure boundary condition BC_2 via a geometry-describing pipe *HDA* (8). This pressure boundary condition describes the pressure profile at the throat in the intake duct of the carburetor. In the overall model of the carburetor, the described model of the valve is linked to the rest of the geometry. Instead of the boundary condition BC_1, the next carburetor-specific element is connected. The pressure boundary condition for BC_2 is taken from the corresponding engine model of the carburetor. An exemplary pressure curve from a motor model at a speed of $n =$ [redacted]* rpm shows figure 3.3.

*Information surpressed due to confidentiality

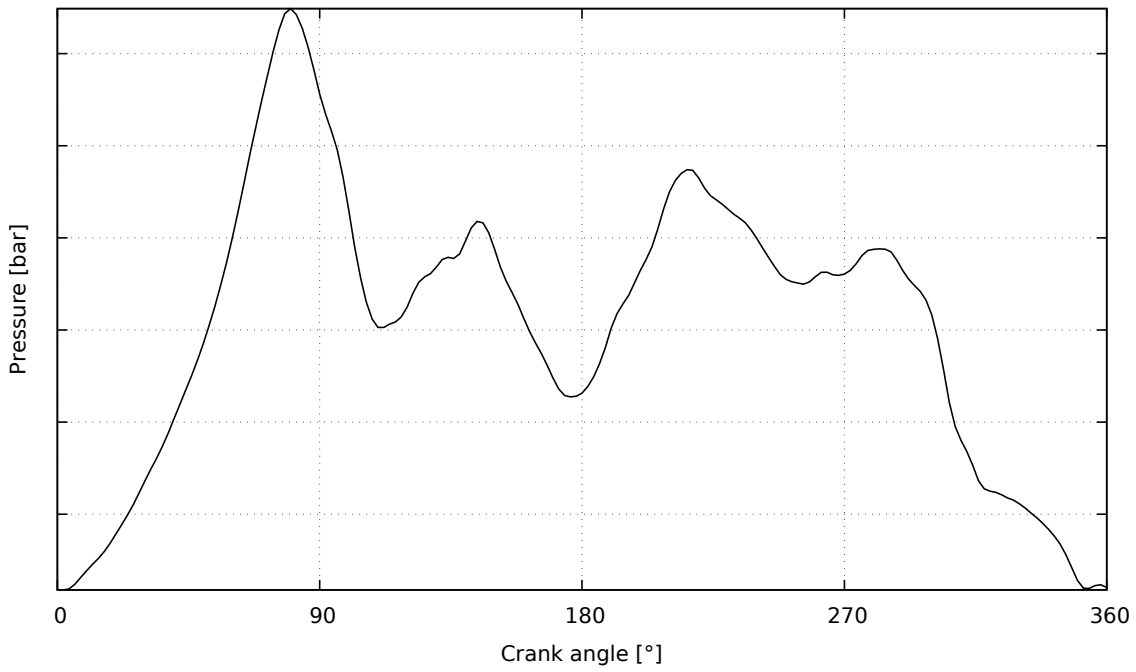

Figure 3.3: Example for the pressure profile in the intake duct (pressure values surpressed due to confidentiality)

The suction process can be seen up to about a crank angle of 60. During this period, the inlet slot is opened into the crankcase and the piston generates a negative pressure therein by the upward movement. This also creates a negative pressure in the intake channel, which sucks in air. A pressure oscillation is produced by accumulation processes and the backflow caused by the piston movement. Reopening the inlet slot at about 290° crank angle will start the suction process again and result in a negative pressure in the venturi.

3.2 Evaluation of simulation results

In order to check the functionality of the 1D model, several test runs with different pressure conditions and rotational speeds were carried out. For the first tests, simplified sinusoidal pressure curves of the form $p(\alpha) = p_1 + \hat{p} \cdot sin(\alpha)$ with the mean pressure p_1, the pressure amplitude $\hat{p}$ and the crank angle α. For the speed $n =$ [redacted]* rpm and the pressure amplitude $\hat{p} =$ [redacted]* mbar, the pressure difference across the disc, the disc movement and the mass flow are shown in Figure 3.4. The pressure difference $\Delta p = p_{Ventilraum1} - p_{Ventilraum3}$ between *Ventilraum1* and *Ventilraum3* is referred to as *pressure difference over the disc.*

*Information surpressed due to confidentiality

If this pressure difference is positive, a positive pressure gradient prevails, a negative pressure difference corresponds to a negative pressure gradient.

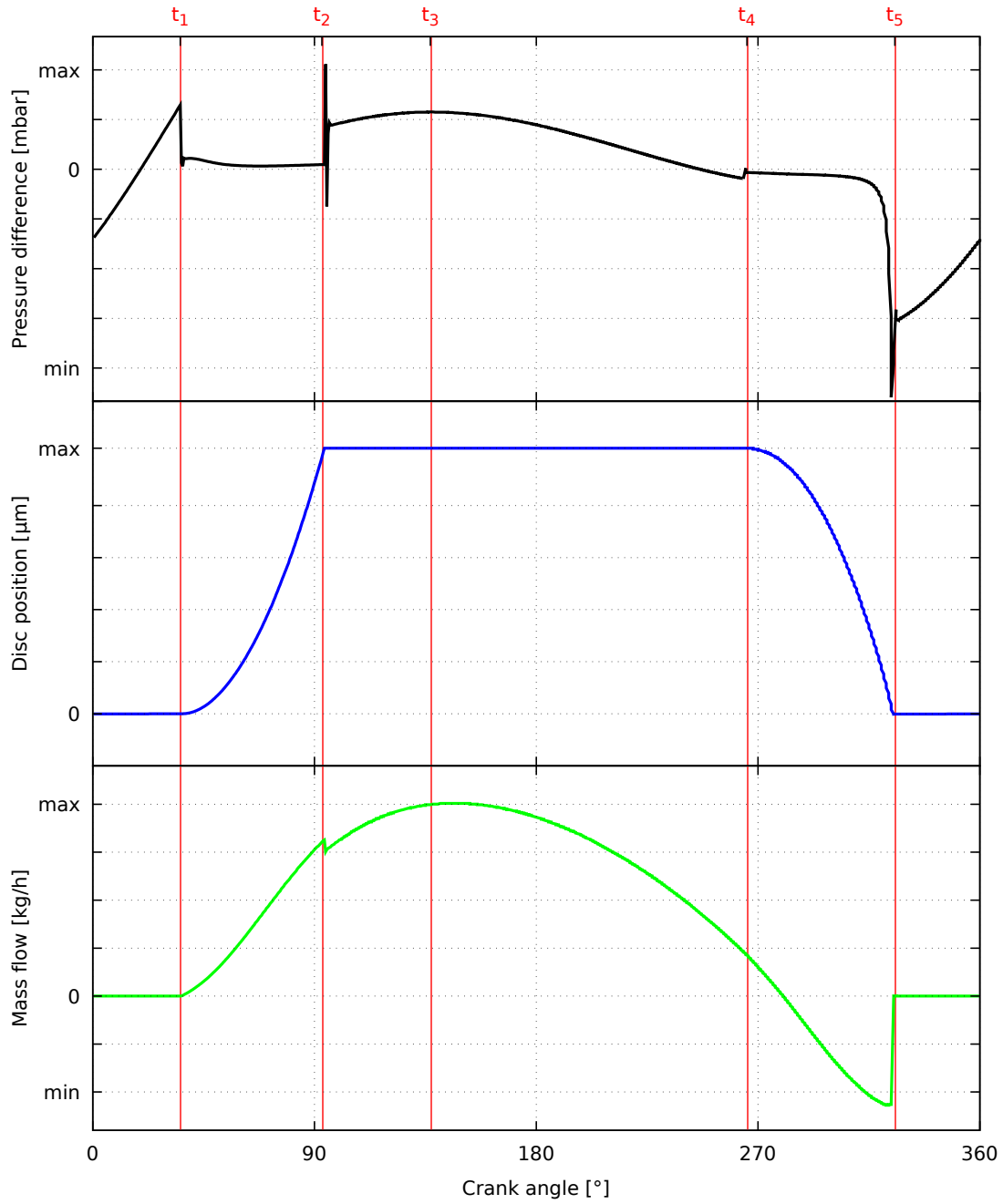

Figure 3.4: Example calculation (values for pressure, movement and mass flow surpressed due to confidentiality)

At the beginning of the rotation shown in figure 3.4 the disc is closed (disc position $x = 0$) and there is no mass flow through the valve ($\dot{m} = 0$ kg/s). The pressure gradient is

negative, which means a compressive force in the negative x direction. Thus, the disc is pressed against the valve seat. However, the pressure gradient increases during the further course of the rotation and becomes positive. When the pressure gradient is positive, the pressure force reverses and presses in the direction of the retainer. However, it does not become large enough to raise the disc from the valve seat until t_1. From this point onwards, a mass flow flows through the valve ($\dot{m} > 0$) and increases with increasing valve opening. The pressure difference remains initially nearly constant, since *Ventilraum1* expands with the disc movement. Only when the disc hits the retainer at the time t_2, the pressure in *Ventilraum1* and therefore the pressure difference is increased abruptly. Up to the time t_3, the pressure difference continues to increase according to the pressure boundary condition, and the mass flow also increases with a constant opening cross-section. From t_3 the pressure gradient and thus the mass flow decreases again until the pressure difference becomes negative at time t_4. Due to the inertia of the fluid, the mass flow only reverses a little later. The disc also moves in the negative x-direction, reduces the opening cross-section and completely closes at time t_5. From this point onwards, no mass flow will flow, and the negative pressure difference will increase again until a new pressure turns it back into a positive pressure drop and the disc opens.

The diagram shows a negative mass flow between t_3 and t_4, which indicates the intake of air and fuel into the carburetor. In fact, the valve can not close infinitly quickly, and it can be assumed that small amounts of air and fuel are also sucked in the real case. Under the assumption that the air volume remains low, this is emitted again in the next cycle and does not get caught in the pipe system of the carburetor. However, the model is not quite true of reality. Due to the hard specification of the boundary conditions, escaping fuel in the model is "destroyed". Only air can flow back from the boundary. Not considered are surface stresses which lead to drop formation and can reduce the proportion of sucked-in air.

3.3 Integration of a simple mass oscillator

From further calculations with the model, however, it becomes clear that there are difficulties with the periodicity. An example of this problem is shown in figure 3.5, where aperiodic results were achieved for periodic pressure boundary conditions with a pressure amplitude of [redacted]* Pa.

*Information surpressed due to confidentiality

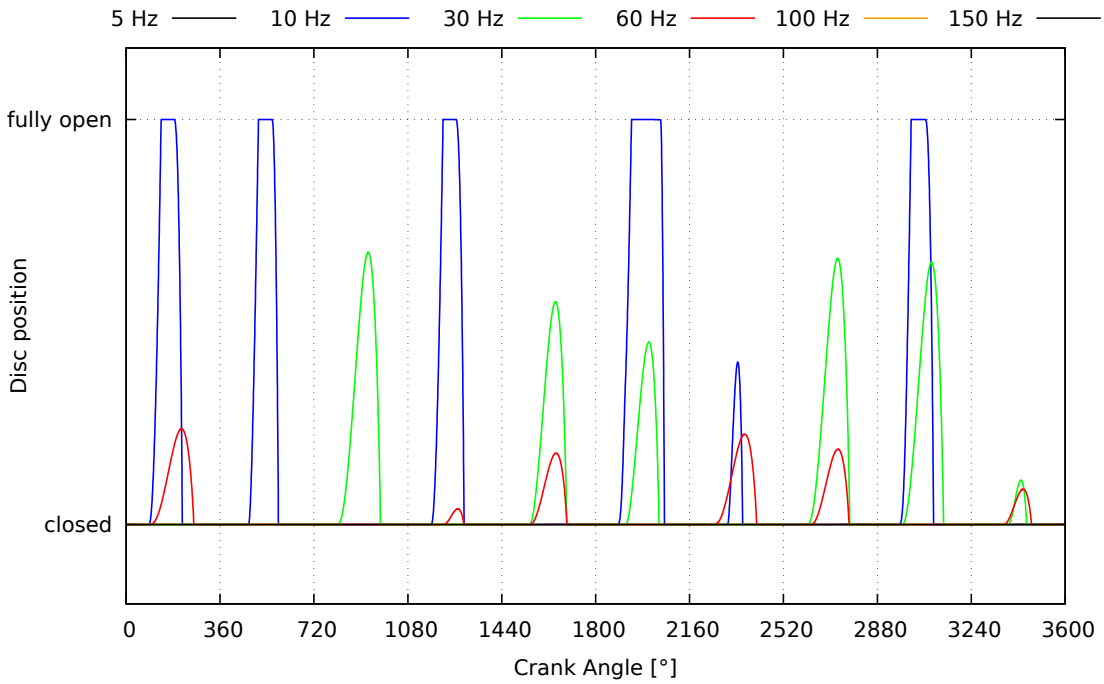

Figure 3.5: Aperiodic Behaviour despite periodic boundary condition (values for disc positions surpressed due to confidentiality)

The aperiodic behavior is due to a too large time step in the calculation. Thus, the solver misses temporal changes in the boundary conditions, leading to the dropouts in Figure 3.5. Thus for the 10 Hz curve the movement of the disc is absent at five out of ten periods. In the periods in which the disc opens, the opening times are different. For the frequencies 30 Hz and 60 Hz, the disc starts to open, but its direction of movement changes at different positions in the different periods. With the higher frequencies of 100 Hz and 150 Hz no disc movement is calculated, the valve remains permanently closed. This may be physically justified, since these frequencies could already be too great to overcome the inertia of the fluid and cause a fluid or disc movement. However, the time step problem is to be considered as a potential reason since the rapid change in the boundary condition at these frequencies could be missed by the solver. Whether the absence of the disc movement is physically or numerically justified is examined below.

Since in DAVE+ the time step can not be trivially assigned with any value but is calculated based on the highest frequency in the system, an undamped simple mass oscillator is built into the system. As shown in figure 3.6, this mass oscillator consists of a mass m, which is clamped between two springs and is deflected by a sinusoidal force F. The higher

the frequency of the force and thus the oscillation frequency of the mass oscillator, the smaller the time step in the 1D simulation.

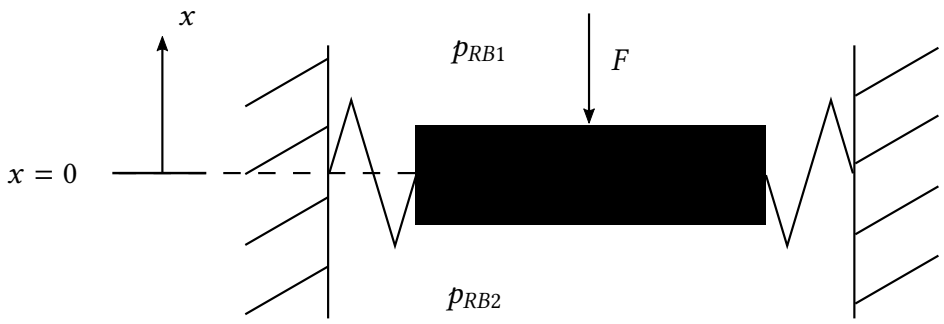

Figure 3.6: Simple mass oscillator

Therefore, a distinction is made between two frequencies. The pressure frequency $f_{pressure}$ denotes the frequency of the sinusoidal pressure boundary condition and corresponds to the motor frequency during operation. On the other hand, the oscillation frequency $f_{oscillation}$ describes the frequency of the periodic force, which deflects the single mass oscillator in the positive and negative x-direction. As a proportionality factor between the two frequencies, the oscillation frequency factor k_{SF} is introduced so that the relation $f_{oscillation} = k_{SF} \cdot f_{pressure}$ holds. With this method, the periodic behavior shown in figure 3.7 as a comparison to the same calculations without a mass oscillator is obtained for the previously performed calculations with the same boundary conditions. An oscillation frequency factor of $k_{SF} = 10^6$ was chosen.

It can be clearly seen that the results for all pressure frequencies with the single mass oscillator are periodic and do not contain any dropouts, as without mass oscillator. Also for the high frequencies of 100 Hz and 150 Hz, a disc movement is calculated, which has remained completely closed without a mass oscillator. It can be derived from this that the absence of the disc movement at these pressure frequencies without a mass oscillator is due to the time step problem and has no physical background.

3.3.1 Influence on CPU-Time

Due to the additionally introduced mass oscillator, the computational effort increases first. For this purpose, a number of examinations are carried out. For certain pressure conditions, the required calculation time for 30 revolutions is determined as a function of the frequency of the mass oscillator. The aim of the study is to determine an oscillation

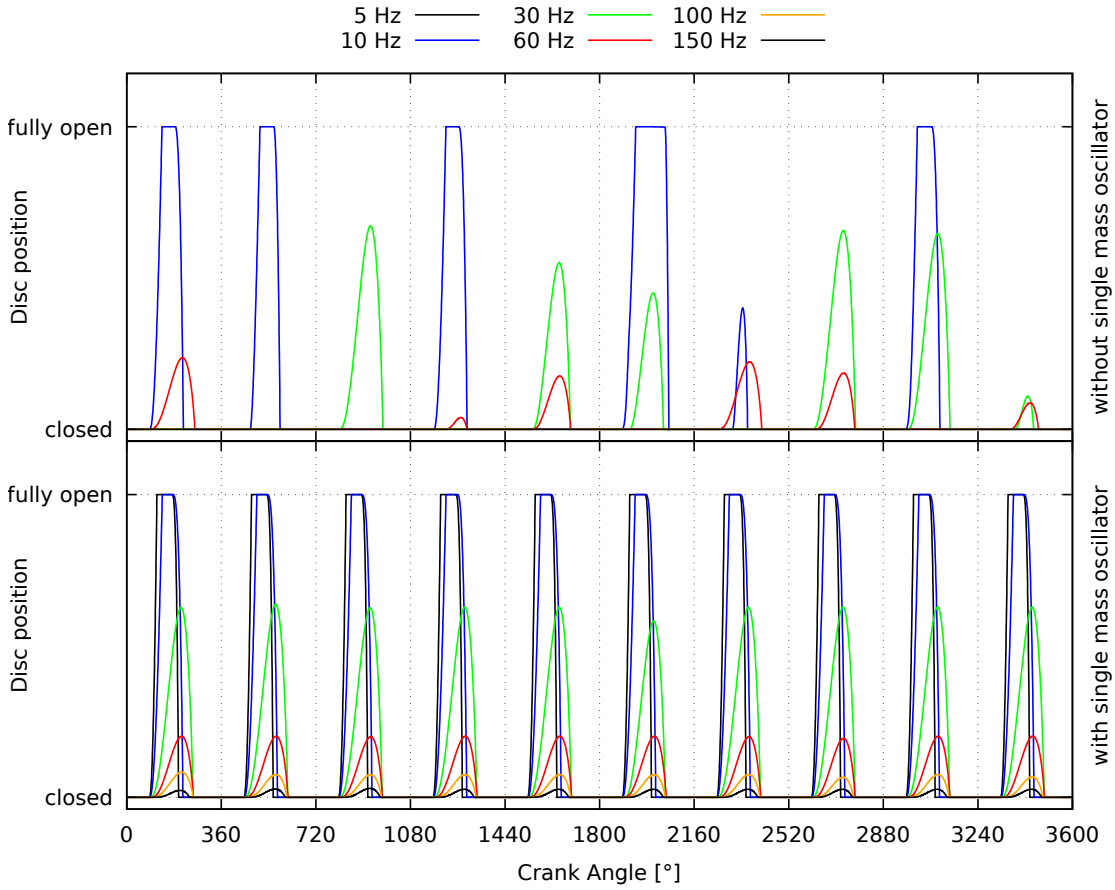

Figure 3.7: Comparison of calculation results without and with mass oscillator (values for disc position surpressed due to confidentiality)

frequency of the single mass oscillator, which ensures an adequate periodicity with an acceptable increase in the computation time. For a sinusoidal pressure boundary condition with two different amplitudes* the examinations are exemplarily shown in the figures 3.8a and 3.8b.

It can be clearly seen that for each pressure frequency the computational effort increases initially with an increased oscillation frequency of the simple mass oscillator before reaching a maximum at a oscillation frequency f_{limit} which is different for each pressure frequency. From the consideration of the respective calculation results it can be seen that the periodicity is increased with increasing oscillation frequencies. The maximum of the various curves marks the corresponding oscillation frequency for each pressure frequency, from which a sufficiently periodic solution is reached at the latest. Since the computational

*Values surpressed due to confidentiality

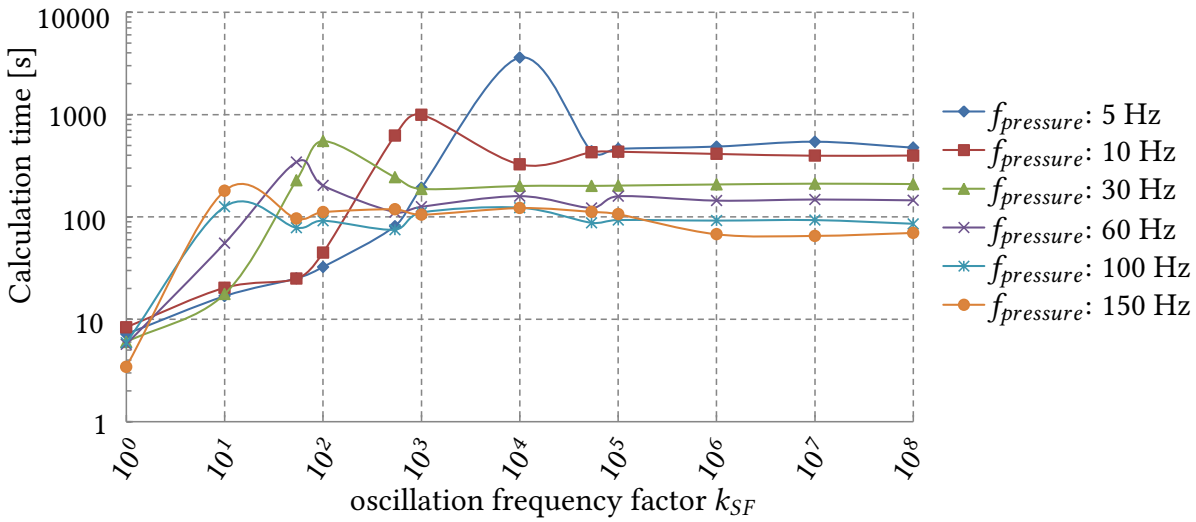

(a) Pressure amplitude 1 (value surpressed due to confidentiality)

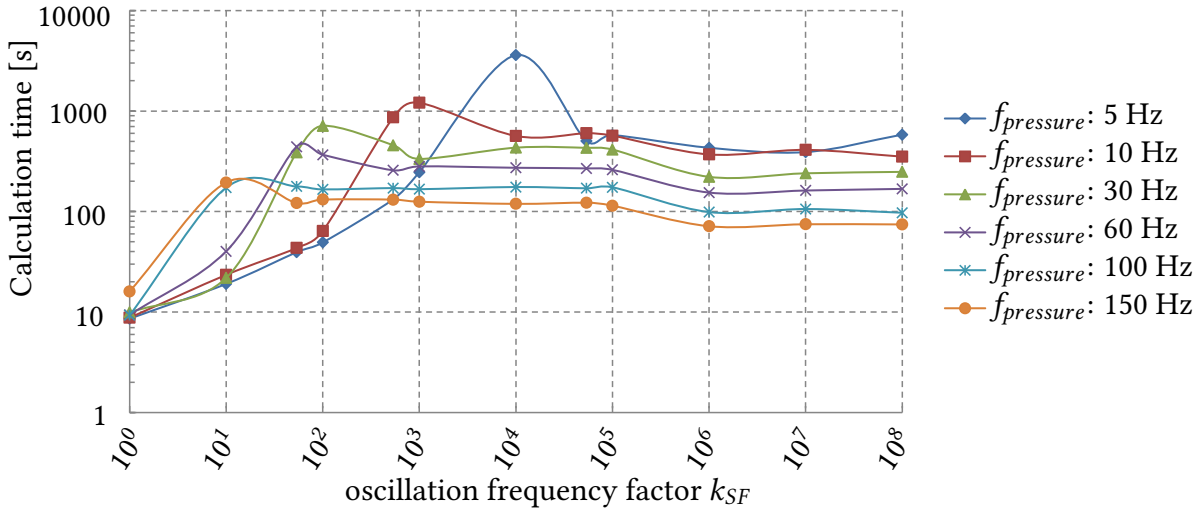

(b) Pressure amplitude 2 (value surpressed due to confidentiality)

Figure 3.8: Computational effort with respect to the pressure frequency and oscillation frequency

effort for even higher oscillation frequencies drops again and then remains at a constant level, the limit frequency of the lowest pressure frequency is decisive. Thus, for the mass oscillator in the model of the check valve, an oscillation frequency factor of $k_{SF} = 10^6$ is selected.

However, when using high pressure amplitudes, it is advisable to carry out the calculation first without the simple mass oscillator and to add it only in the case of non-periodic results. Furthermore, the previous investigations relate only to the model which contains only the check valve. In the overall model of the carburetor in which the model of the check valve to be developed is to be integrated, there are, in addition to the check valve, further components with different frequencies so that the time step in the overall model can be sufficiently small even without the single mass oscillator.

4 Experimental investigation

To investigate the valve behavior and to validate the simulations, a test bed was designed to simulate the pressure and flow conditions at the check valve in the carburetor. A flexible design allows the investigation of different operating points and geometries as explained in the following.

4.1 Structure and operating principle

In order to simulate a realistic image of the carburetor valves on the test bed, the test bed is constructed according to the figure 4.1.

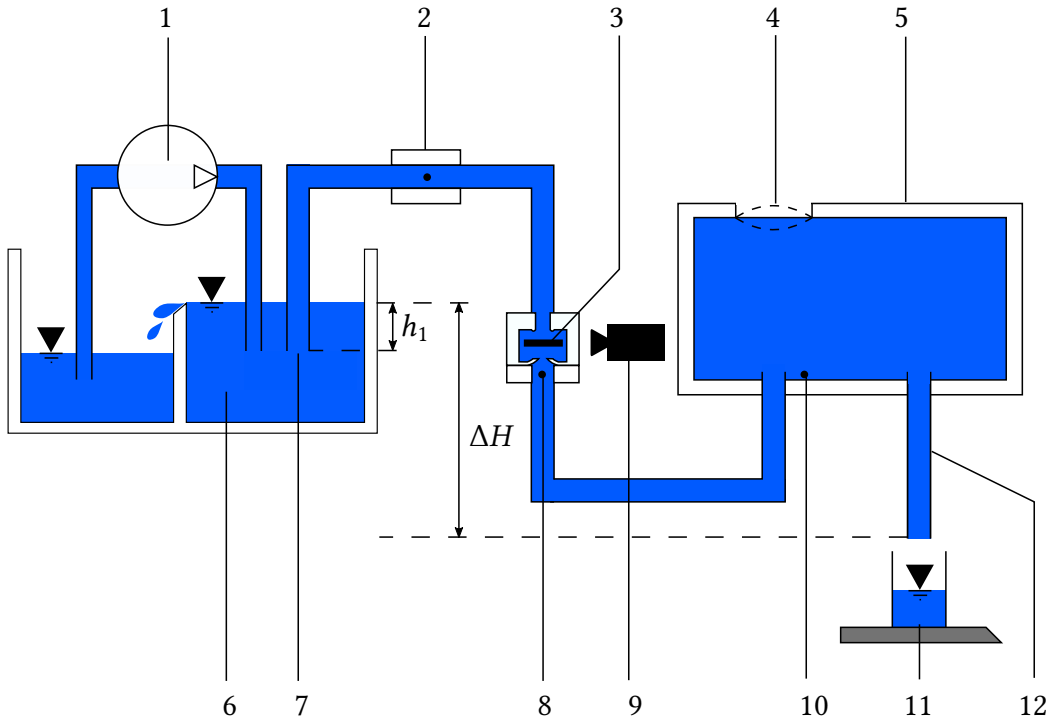

Figure 4.1: Schematic structure of the test bed

The basic idea is, in analogy to the real application of the carburetor valve, to produce a constant pressure upstream of the valve as a simulation of the control chamber and a pressure oscillation downstream of the valve as an illustration of the pressure conditions in the intake duct. The constant pressure is applied using an overflow basin (6) as in the figure 4.1. A pump (1) ensures that the water level is always at the same height so that the constant pressure is present before the inlet (7) of the hose. In order to generate pressure oscillations behind the valve, a pressure vessel (5) is selected, which changes its volume temporally via a membrane (4) and thus generates pressure oscillations. If the membrane bulges outwards or rather upwards, the volume of the container becomes larger. This causes water to be sucked, which corresponds to a negative pressure downstream of the valve (3). The disc opens through the positive pressure gradient and water can flow from the overflow basin through the valve towards the pressure vessel. If the membrane is deflected inwards or rather downwards, the volume of the vessel is reduced and water is displaced and pushed into the hoses. This creates an overpressure downstream of the valve, closes the plate, and no more flow through the valve is possible. This means that the displaced water flows through the outflow hose (12).

There are three pressure measuring points in the system to which a pressure sensor is attached. *Pressure sensor 1* is located within the pressure vessel (10), *pressure sensor 2* downstream of the valve (8) and *pressure sensor 3* upstream of the valve (2). The flow-through valve geometry corresponds to the geometry of the check valves actually installed in the carburetors. In order to be able to observe the disc movement with a high-speed camera (9), transparent test carriers made of Plexiglas are used. Such a test carrier is shown in Figure 1 with the disc (1) and the pressure measuring point (2) downstream of the valve.

From the videos recorded with the camera, the disc motions can be derived using the program *VW-9000 MotionAnalyzer*, so that a curve for the disc path over time is created. In addition to the pressures and the disc path, the average mass flow $\dot{m} = m_t/t$ is also determined. For this purpose, a fine measuring scale is used, which weighs the water mass m_t issuing from the outflow hose within the measuring time t. Due to the adjustable height difference ΔH between the water level in the overflow tank and the outflow hose, a medium pressure difference can be set across the valve.

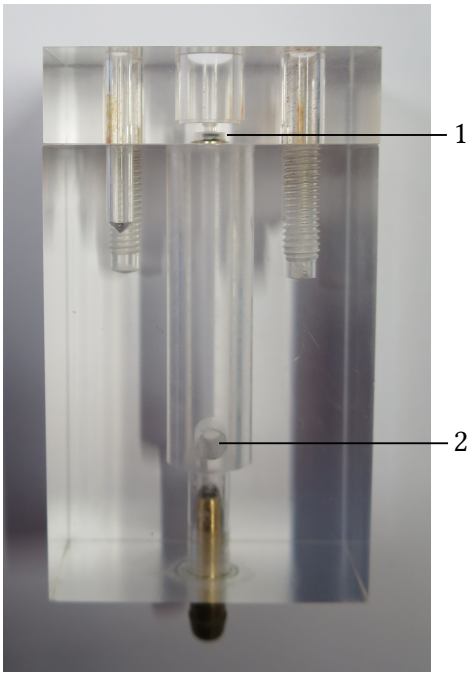

Figure 4.2: Transparent check valve for the observation with high-speed camera

4.2 Measurement instrumentation

The pressure sensors *Pressure Transducer XTEL-6-140M-1.7BARA* of *Kulite Semiconductor Products Inc.* are used for the pressure measurement at the intended measuring points. These pressure sensors are screwed to the desired location in the system using an M3.5 thread. The compact size makes it possible to use them with small flow cross sections. For example, they can be used in the channel below the check valve from the figure 4.2, which has a diameter of only 3 mm. The measurement technique is based on the principle of piezoresistive pressure sensors. For this purpose, the pressure sensors have a diaphragm made of silicon, on which electrical resistances are placed. With an elastic deformation of the diaphragm by pressure changes, the electrical resistances change linearly. This results in a proportional change in the electrical voltage signal, which is conducted from the pressure sensor to the measuring amplifier. From the measuring amplifier, the amplified voltage pulses are subsequently passed to an evaluation medium (for example a storage oscilloscope), in which the voltage profile over time is recorded. Before the pressure sensors can be used, they must be calibrated so that the measured voltage values can be assigned to a pressure value. For this purpose, each sensor is subjected to various defined pressures in order to be able to determine a relationship between measured voltage and applied pressure. Therefore a calibration system is constructed, which is shown in Figure 4.4.

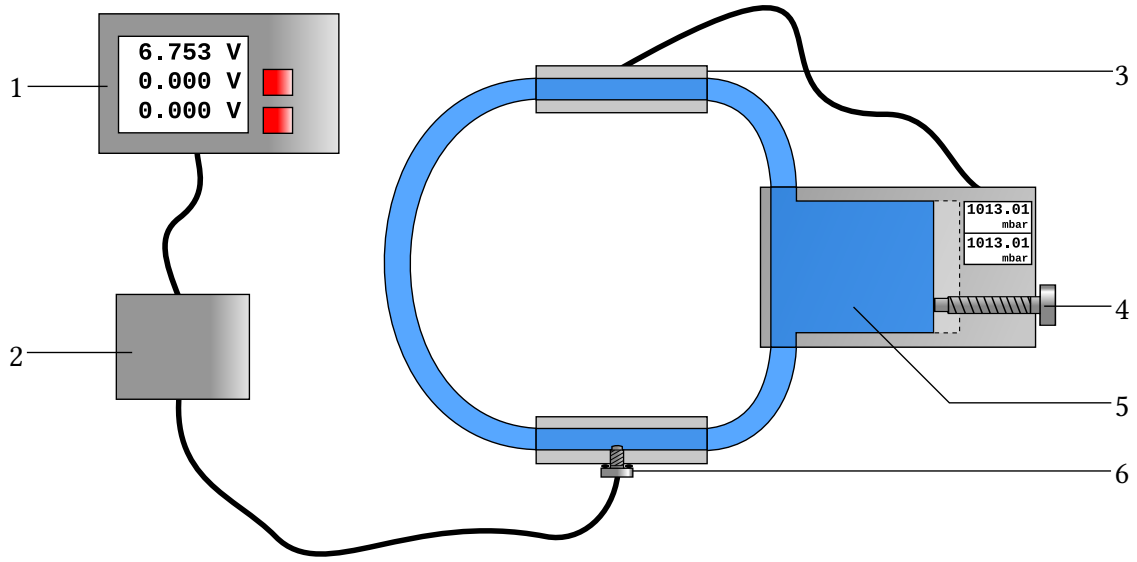

Figure 4.3: Structure of the calibration system for pressure sensors

The sensor (6) to be calibrated is screwed vertically into a hose in order to measure the pressure therein. This hose is connected on one side to the pressure chamber of the pressure calibrator *DPI610* (5), and on the other side to an external pressure sensor (3). This external pressure sensor is connected to the pressure calibrator. Thus the pressure sensor to be calibrated is located in a closed, air-filled system. By means of a pump, the pressure in the pressure chamber can be increased or decreased. Rotating an adjusting screw (4) changes the volume of the pressure chamber very finely so that the pressure in the system increases slightly or decreases according to the direction of rotation. In addition, the pressure chamber can be vented so that ambient pressure prevails in the system. In this way, various pressures can be set. The measuring amplifier (2) receives a voltage signal from the pressure sensor to be calibrated, which voltage signal is passed on to a voltage measuring device (1). Thus the corresponding voltage signal can be read off and recorded for each set pressure. As a result, the relationship between the voltage signal and the applied pressure can be determined for each pressure sensor. This relation is shown for the pressure sensors used in the work in figure 4.4.

The sensors are used for all measurements at a fixed position on the test bed. *Sensor 1* is screwed into the bottom of the pressure vessel, *Sensor 2* is located downstream of the valve, and either *Sensor 3* or *4* is attached between the overflow basin and the valve. The positioning of the sensors is shown in Figure 4.5.

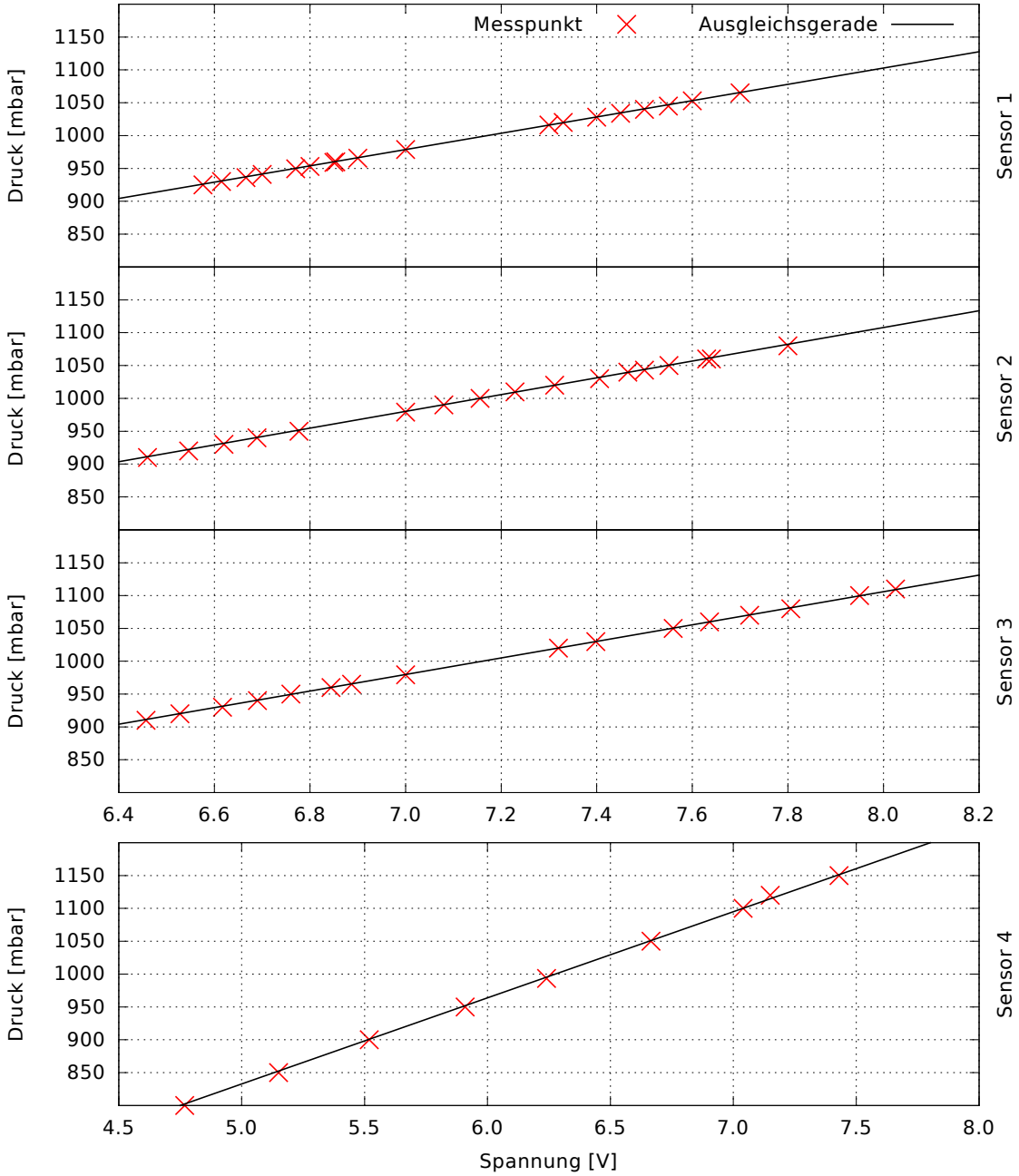

Figure 4.4: Relationship between set pressure and measured voltage signal

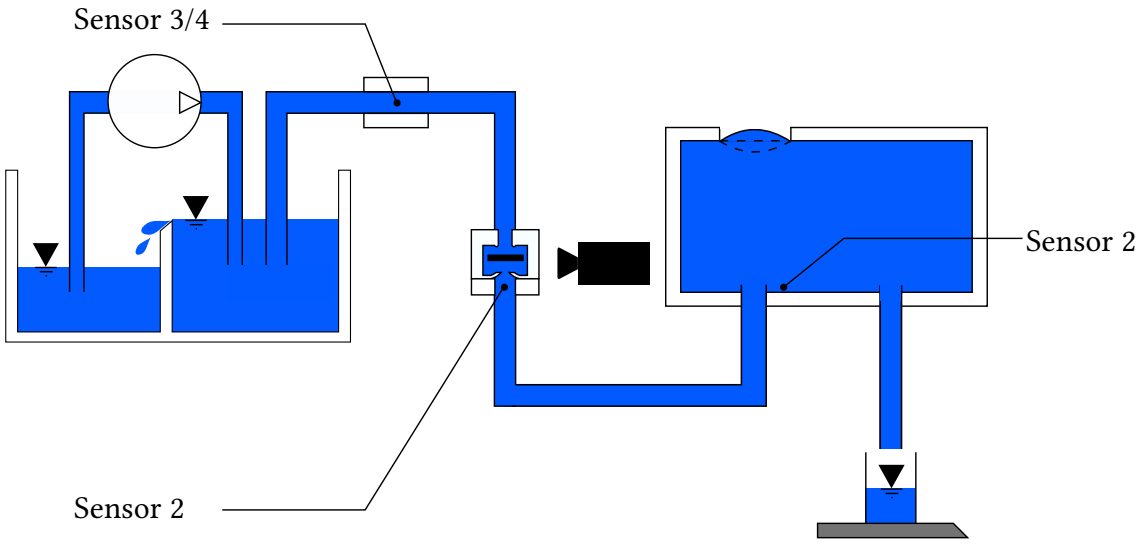

Figure 4.5: Positions of the pressure sensors

4.3 Measurements and evaluation

First, the deflection of the membrane on the pressure vessel is effected by means of an electric motor which operates an eccentric and thus produces a translational upward and downward movement of the membrane. With this experimental set-up, various operating points are measured, which are listed in table 4.1.

The first two experiments were performed with only two pressure sensors (*sensors 2* and *3*). From the third experiment on the additional *pressure sensor 1* was placed in the pressure vessel. In the videos for Experiment 2 and 10 it can be seen that the valve does not close because the disc appears to stick to the retainer. Thus, in these experiments, the disc is permanently completely opened, as a result of which the mass flow is very high compared to the other measurements. It is also noticeable that the pressure amplitude at *sensor 1* is in most cases lower than the amplitude of the other two sensors. This is astonishing in that the pressure amplitude should actually decrease with increasing distance from the location of the pressure generation. This is true for *sensors 2* and *3*, since *sensor 2* measured a higher pressure amplitude than *sensor 3* in each measurement, which is mounted in a larger distance from the pressure vessel where the pressure oscillation is generated. Accordingly, *Sensor 1* would have to measure an even greater amplitude directly in the pressure vessel than the other two sensors, since it is much closer to the pressure generation. The fact that this is not the case could be due to the position of the sensor. For installation reasons, this is not mounted directly in the flow channel, but is screwed through a bore into the

Table 4.1: Measurements with electric motor

Name	Frequency from video [Hz]	Frequency pressure file [Hz]	Mean mass flow [g/h]	pressure amplitude Sensor 1 [mbar]	Sensor 2 [mbar]	Sensor 3 [mbar]
Experiment01	40	40	12,00	-	120	95
Experiment02	-	61	43,80	-	70	64
Experiment03	34	37	15,60	16	91	80
Experiment04	34	30	9,96	25	95	60
Experiment05	32	32	15,60	54	100	75
Experiment06	33	33	15,60	53	95	90
Experiment07	54	57	19,80	65	70	45
Experiment08	53	53	24,00	84	100	75
Experiment09	64	62	24,00	85	65	40
Experiment10	-	57	27,96	75	30	10
Experiment11	42	36	12,00	15	40	30
Experiment12	18	14	7,98	83	100	75
Experiment13	32	31	9,96	45	85	65
Experiment14	60	-	19,98	-	-	-
Experiment15	24	22	7,98	45	45	35
Experiment16	52	-	19,98	-	-	-
Experiment17	66	64	24,00	70	40	20
Experiment18	8	9	7,89	25	46	20

bottom of the vessel, as shown in Figure 4.6. Thus, it is only about 3.6 millimeters above the vessel bottom.

In this arrangement, the hose which connects the pressure vessel to the check valve lies directly on the center axis of the circular membrane. As a result, the pressure oscillations find their way largely undisturbed directly into this hose. In the case of the pressure sensor *1*, on the other hand, the assumption can be made that the pressure oscillations are reflected on the container bottom, which results in the superposition of the incoming wave and of the reflected wave. The resulting wave then results from the superposition of the incoming wave and the reflected wave. Reflection at the bottom of the container results in a phase jump of half a period between the reflected wave and the incoming wave. Accordingly, the sum of incoming and reflected wave directly at the wall is equal to zero at all times, resulting in a wave-knot of the resulting vibration. The resulting wave can be represented mathematically as a function of the distance x to the wall and the time t as

$$p_{res}(x,t) = 2 \cdot \hat{p} \cdot cos(2\pi\frac{x}{\lambda} + \frac{\lambda}{2}) \cdot sin(2 \cdot \pi\frac{t}{T} - \frac{\pi}{2}) \tag{4.1}$$

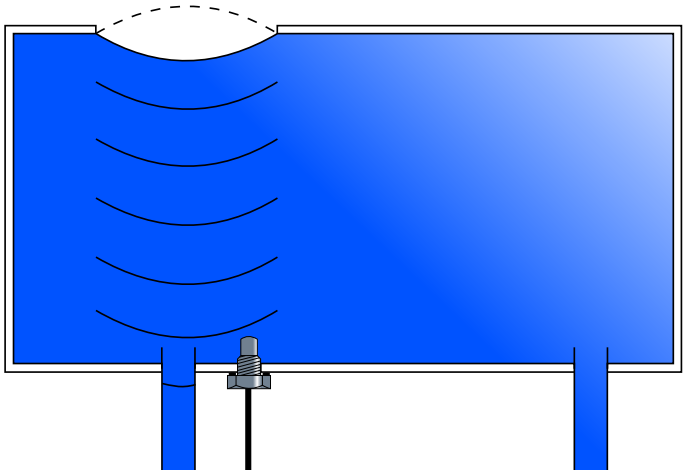

Figure 4.6: Position of the pressure sensor within the vessel

The membrane is deflected upwards and downwards from the zero point in each case one distance x_{Hub}. This gives the wavelength of the oscillation to $\lambda = 4 \cdot x_{Hub}$. With the distance of the pressure sensor of about 3.6 mm to the wall and the membrane deflection of 2 mm upwards and downwards, the resulting wave at the sensore is obtained as

$$p_{res}(x,t) = 2 \cdot 0,31 \cdot \hat{p} \cdot sin(2 \cdot \pi \frac{t}{T} - \frac{\pi}{2}) \tag{4.2}$$

The derivation of the wave equations can be found in [BD16].
In this example, at the position of the pressure sensor an amplitude of the resulting wave is obtained, which is only about 62% of the amplitude of the incoming wave. For this case, Figure 4.7 shows the temporal progression of incoming, reflected and resulting pressure wave.

Depending on the individual deflection in each experiment, the assumption is plausible and the pressure amplitude measured for this sensor differs significantly from the pressure amplitude of the actual incoming wave. Because of this, the pressure measurements in the pressure vessel are not further considered.

The *Experiment7* is used as an example for the evaluation of the measured data. After a stationary running behavior of the test bed has been reached, a high-speed recording over three seconds with an image frequency of 3600 fps as well as the pressure over time is recorded. A section of 0.5 s of the video is evaluated slowed down with a factor of 120. The number of closing movements resulted in 27, leading to the frequency $f_s = 54$ Hz. This frequency is checked using the pressure values from figure 4.8, by reading the period duration from the pressure curves.

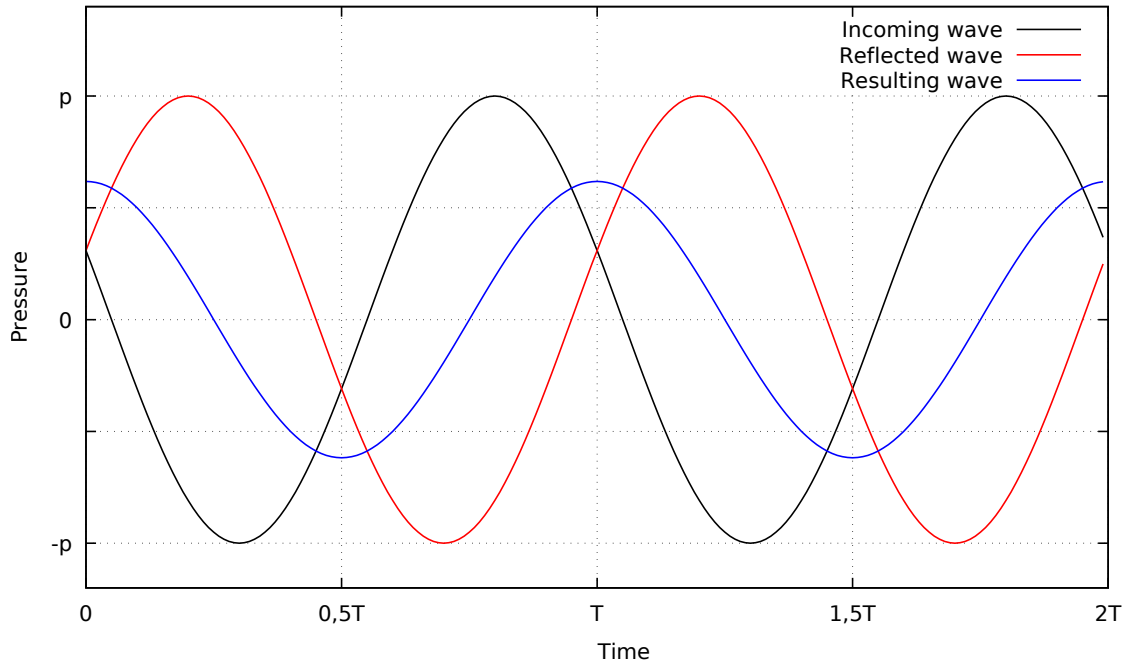

Figure 4.7: Incoming, reflected and resulting wave at the position of the pressure sensor with $x = 3,6$ mm distance from the vessel bottom at a wavelength of 8 mm

For this purpose, the time difference between two adjacent maxima is determined and the reciprocal value is formed. This results in the frequency $f = 1/T = 1/0.0175 \text{ s} \approx 57 \text{ Hz}$. This frequency corresponds to a rotational speed of approximately 3425 rpm, which is above the idling speed of a carburetor in hedge trimmers. Also the pressure amplitude downstream of the valve in some of the experiments corresponds approximately to the actual pressure amplitude in the intake duct during real operation, which is about $A = \pm$[redacted]* mbar.

From the video, the movement curve of the disc can be derived by means of a point tracing. For this purpose, tracking points are placed on the disc and further tracking points are applied to the resting geometry of the valve, in order to later filter out and smooth the vibrations of the camera or the valve holder. For example, Figure 4.9 shows the positioning of the tracking points on the disc and on the geometry.

For experiment 7 the motion curve, which is shown in the figure 4.10a, is initially not smoothed. In contrast the smoothed motion curve of the disc is shown in Figure 4.10b.

In order to obtain meaningful measured values for the average mass flow, this is measured over a period as long as possible. Since, however, the electric motor can not hold a stationary operating point indefinitely for a long time and the rotational speed changes

*Information surpressed due to confidentiality

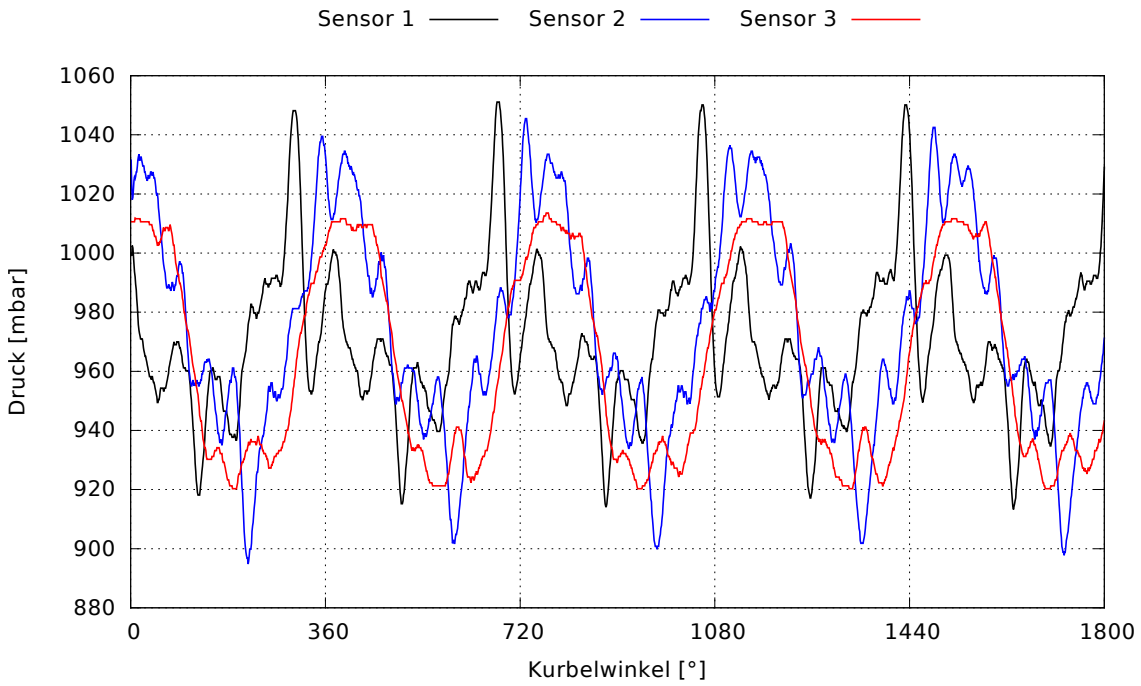

Figure 4.8: Pressure measurements in Experiment7

during operation without external interference, the mass flow was measured and averaged over 30 s or 60 s depending on the operating point and running behavior. However, the experimental setup described so far has some weaknesses. On the one hand, this is the already mentioned non-stationary behavior of the motor with unintended speed changes. The attainment of a stationary operating point is difficult under these circumstances. This is directly linked to uncertainties in the mass flow measurement since the mass flow can only be measured over small time periods of constant speed. In addition, the rotational speed can not be set arbitrarily, but can only be adjusted by adapting the electrical voltage and current intensity and the acoustic estimate of the rotational speed. Another reason for a change in the test bed is the achievable speeds. These are below or just above the idle speed of the engine. However, rotational speeds in the area of coupling ([redacted]* to [redacted]* rpm) and higher, which still have unexplained effects associated with the geometry of the check valve, are striven for. The approach for a modified design of the test bed is described in chapter 6.2.

*Information surpressed due to confidentiality

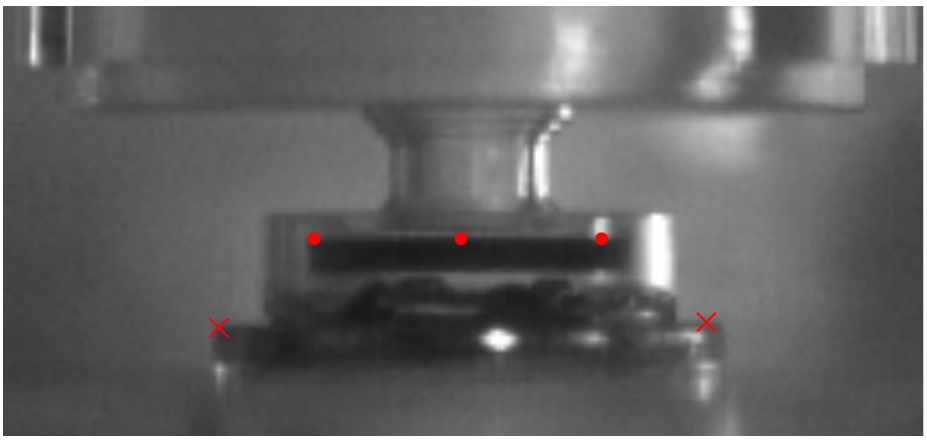

Figure 4.9: Tracking points in video evaluation

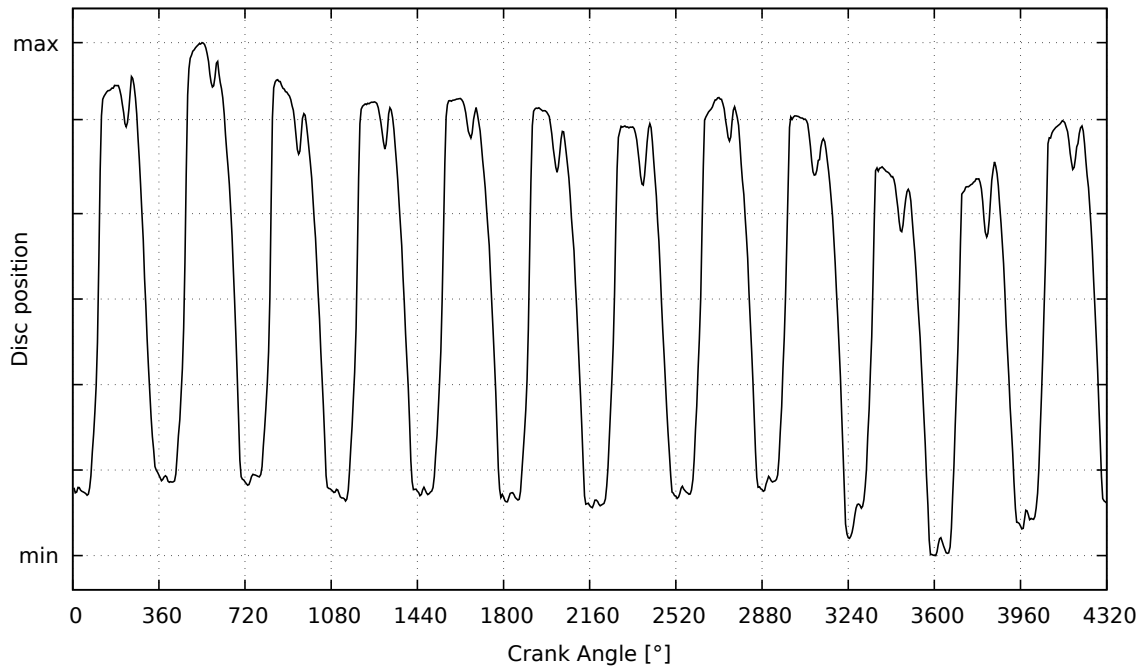

(a) Directly from video

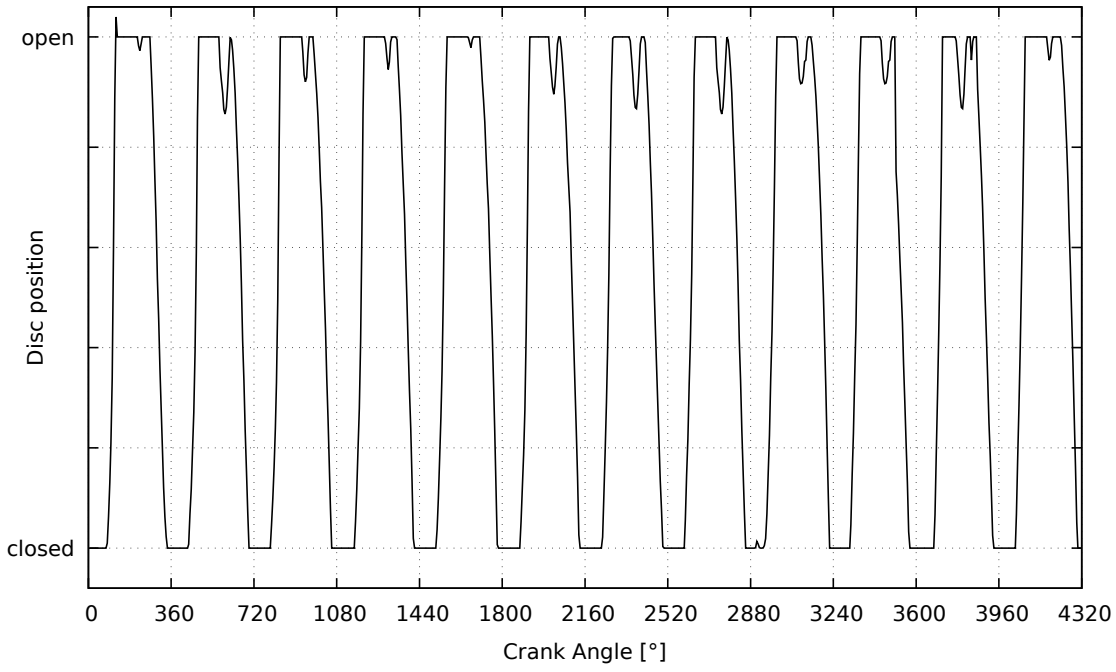

(b) After smoothing

Figure 4.10: Motion curve of the disc from the video (values surpressed due to confidentiality)

5 Validation

For the validation, the one-dimensional model was compared with both three-dimensional calculations and the measurements from chapter 4. This chapter first gives an overview of the 3D calculations and describes the geometric and flow-mechanical matching of the 1D model to the 3D model. This is done by means of a stationary and a periodic-stationary simulation. Subsequently, the matched 1D model is validated using a further periodic-stationary simulation. The validation based on the measurements carried out is also described in this chapter. The comparison with the periodic-stationary measurements from chapter 4 leads to further measurements with corresponding comparisons.

5.1 3D Simulation

In order to obtain a comparison basis for the validation and further development of the one-dimensional model, the flow through the check valve has already been simulated three-dimensionally using the software ANSYS Fluent. Since this is a fluid-structure interaction in which fluid flow and disc movement influence each other, such a three-dimensional calculation of the considered system is extremely time-consuming and cost-intensive. Already the creation of the geometry, the networking and finally the simulation itself take many working and calculation hours or days. For this reason, the 3D simulation is not suitable for extensive parameter studies. Instead, a one-dimensional model can deliver results from a few seconds to minutes, which take into account the most important effects. This allows the effects of system changes to be identified in extensive parameter studies. In order to achieve this, it must first be ensured that the one-dimensional model delivers results that are consistent with 3D simulation. In the first step, the 1D model is throttled by mechanical means via the matching from 3D to 1D, in order to reproduce the pressure distribution and the mass flow of the 3D model. 3D effects such as directional changes in bends, sudden cross-sectional jumps or direction-dependent constrictions that produce a pressure loss can thus be included in the more abstract 1D model. In the second step, a further calculation is carried out under modified boundary conditions both in 3D as well

as with the matched 1D model. A comparison of the results is used to validate the 1D model. In the following firstly the already performed 3D calculations are presented.

5.1.1 Description of the 3D model

The 3D simulation was performed for different boundary conditions. Initially, boundary conditions which reflect the real carburetor operation as good as possible are aspired to. However, there are numerical problems due to the high frequencies. In order to show this, the calculation is performed with a sinusoidal pressure boundary condition $p_{RB1}(\alpha) = p_U - 200\ Pa + 800\ Pa \cdot sin(\alpha)$ with the low frequency of 5 Hz upstream and a constant pressure $p_{RB2} = p_U$ downstream of the valve. The resulting mass flow and the movement of the disc are shown in Figure 5.1.

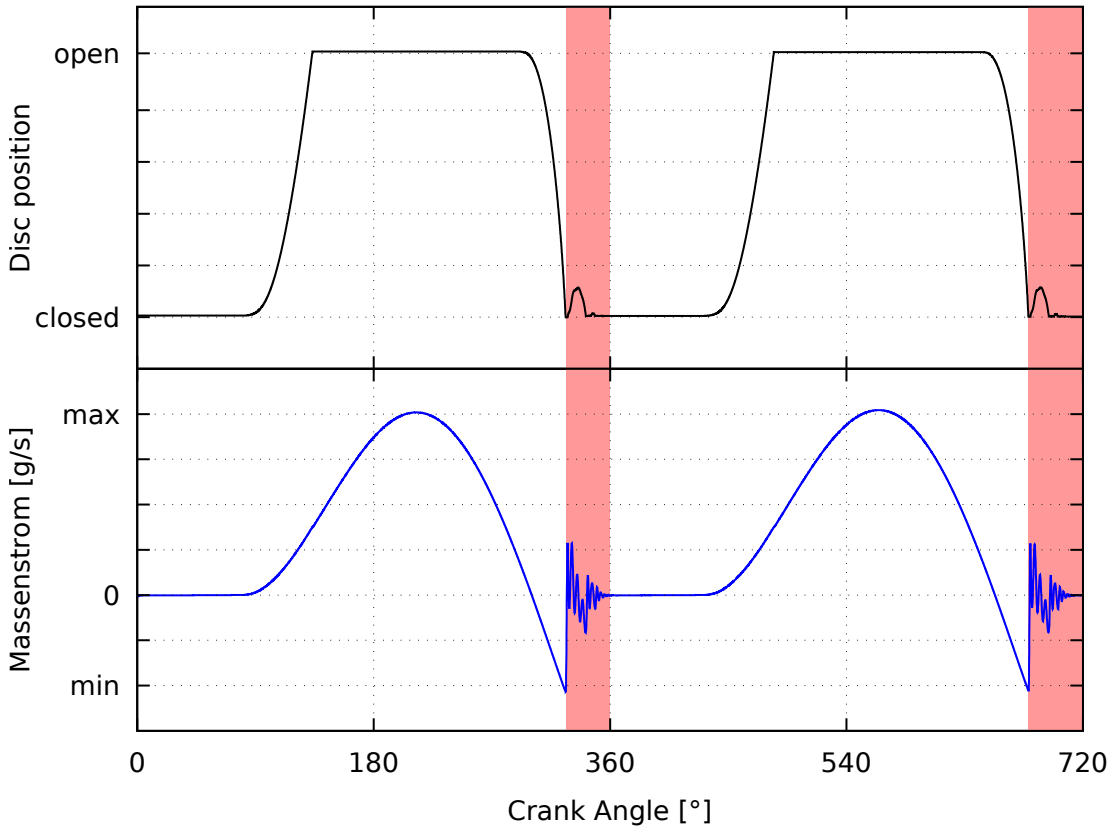

Figure 5.1: Fluctuations in mass flow at closing movement of the disc (values surpressed due to confidentiality)

It can be seen in the areas marked in red that there is a sudden change in the mass flow when the disc closes. These fluctuations are presumably numerically justified and the values pendulate to *zero* in the following time. At higher frequencies, however, there is

not enough time between the closing of the disc and the lifting back from the valve seat, so that these vibrations can subside. If the disc is lifted before the disturbance has subsided, the initial value of the mass flow corresponds to a randomly generated value other than *zero*. For this reason, only small frequencies such as the 5 Hz from Figure 5.1 lead to periodically stationary solutions which provide sufficient time for the abatement of the numerical oscillations. For the geometry of the investigated check valve, two calculations were performed with periodic solutions, the periodic pressure boundary condition of which in form of

$$p_{BC1}(\alpha) = p_{BC2} + \Delta p + A \cdot sin(\alpha) \tag{5.1}$$

are listed in table 5.1 each.

Table 5.1: Boundary conditions of 3D simulations with periodic results

Number	Amplitude A [Pa]	Pressure difference Δp [Pa]	Frequency [Hz]
1	800	-200	5
2	8000	-2000	10

Based on the test bed, the check valve is modeled in the 3D simulation between the hoses, which represent the inflow from the overflow basin and the hose to the pressure vessel. The boundary conditions are placed at the ends of these hoses. The modeled section of the test bed and various views of the 3D model are shown in Figure 5.2.

The pressure distribution on the disc resulting from calculation 1 and the velocity distribution in the fluid are shown in Figure 5.3. This shows that the distribution of the one-dimensional model corresponds well to the distributions of pressure and velocity. The high speeds prevail in those areas of the valve, which are modeled as pipes in DAVE+. In the sections of the flow channel, which are depicted as volumes in DAVE+, the fluid moves only slowly or is at rest. The pressure distribution on the disc also reveals two significant zones of different pressures. A high pressure is applied to the inner red part of the disc. This inner part corresponds approximately to the area delimited by the circular valve seat. On the outer, green colored part of the disc, the pressures are significantly lower.

In order to ensure good comparability between the one-dimensional and three-dimensional calculations, the state variables calculated in Fluent were spatially averaged over different sections. The sections depend on the division in the one-dimensional model, since DAVE+ only calculates a mean pressure in each element for each time step, and only differentiates between the inlet and outlet flow rates with constant values across the cross-section.

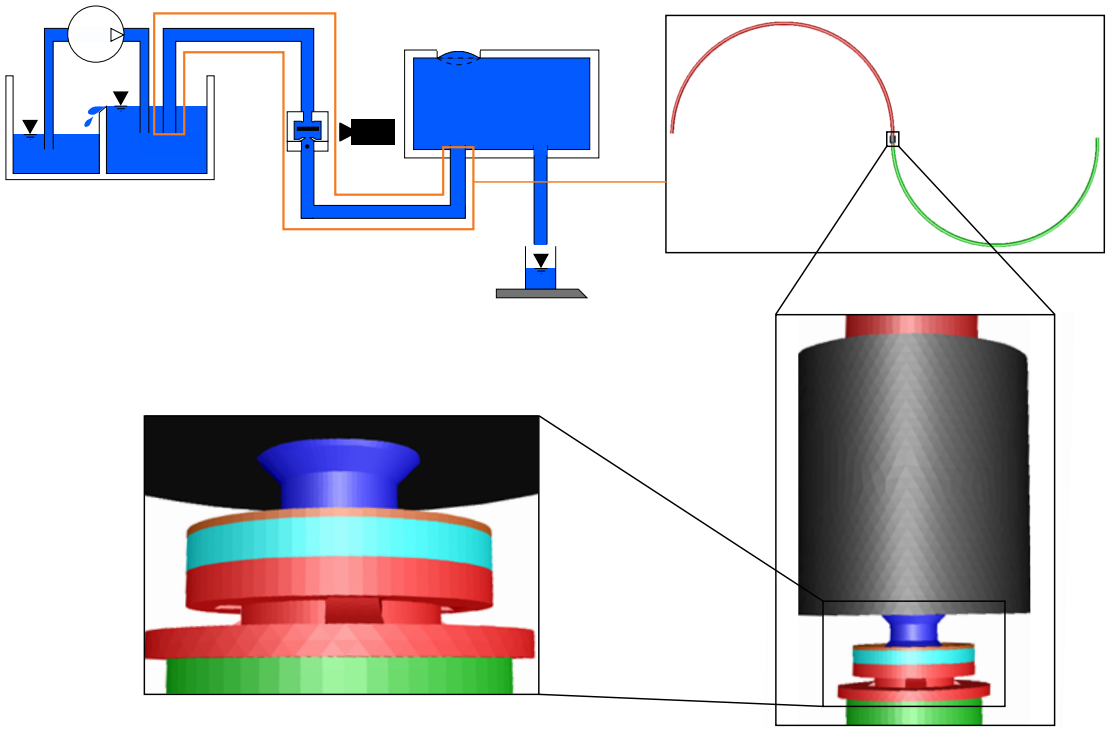

Figure 5.2: Section of the test bed modelled in 3D

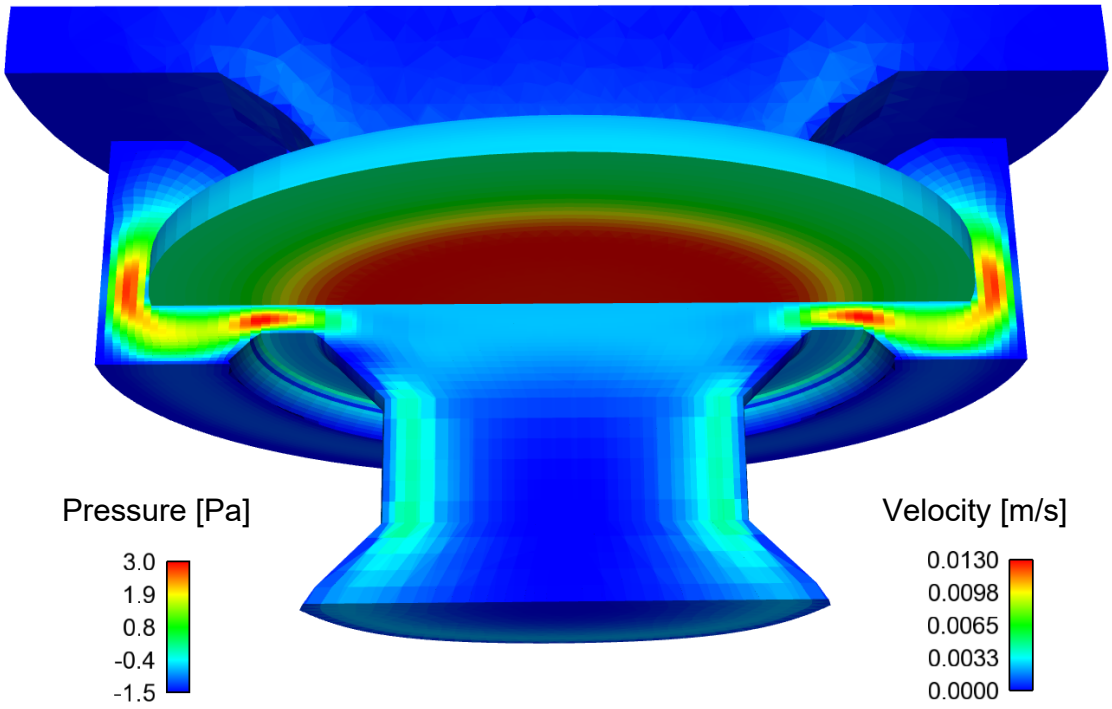

Figure 5.3: Pressure distribution on the disc and velocity distribution of the fluid seen from the valve seat side

5.1.2 3D-1D-matching

For the preparation of the validation, the mass flow and the pressure profile of the one-dimensional model in DAVE+ are compared with those of the three-dimensional model in ANSYS Fluent in a first step. Three-dimensional effects such as vortex formation can not directly be represented in the one-dimensional model. Therefore, the effects of such effects are considered as pressure losses in the 1D model. During the matching process, an optimizer performs an automated variation of the pressure loss coefficients of predetermined elements until target mass flow and pressure are reached. There is a stationary matching in which constant pressure boundary conditions are used and a periodic-stationary matching using periodic pressure boundary conditions.

5.1.2.1 Stationary matching

The approach of the stationary matching of 3D simulation and 1D simulation is performed according to the scheme shown in figure 5.4.

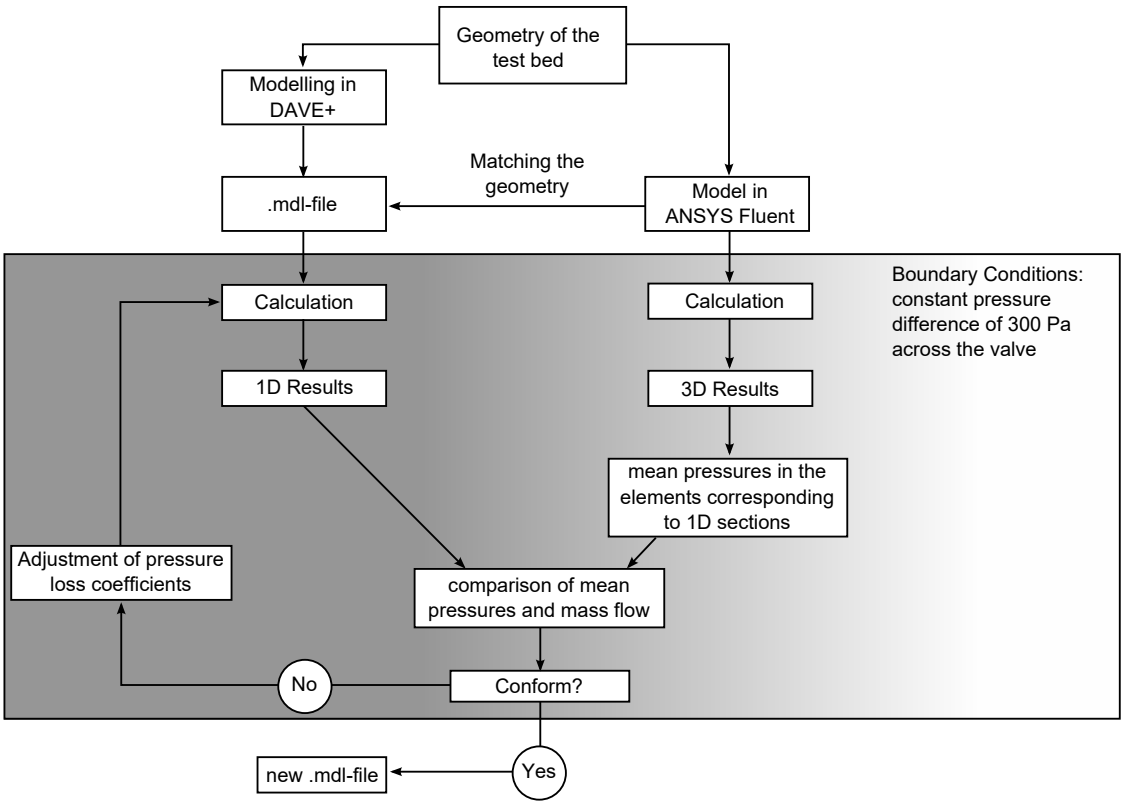

Figure 5.4: Approach of stationary 3D-1D-matching

In order to ensure good comparability, the geometric values from the 3D model are first transferred to the 1D model so that the identical geometry is considered in both calculations. Then a calculation case with the same constant pressure boundary conditions is performed in both DAVE+ and ANSYS Fluent. Here a pressure difference of $\Delta p = 300\ Pa$ is used between the boundary conditions. From the results of the three-dimensional simulation, the average pressures for the valve sections are calculated according to the division in DAVE+ and compared with the one-dimensionally calculated pressures. In addition, a comparison of the average mass flows is carried out. An optimizer finds an iterative change in the pressure loss coefficients of all elements in the 1D model. The modified model is used for a further calculation, the results of which are again compared with the 3D results. This process is repeated until a satisfactory correspondence of the mass flow and the pressures in the elements is achieved. The mass flow in 3D and in 1D is $\dot{m} = 1640\ g/h$ after the end of the matching process. The pressures in the elements are also very good after the matching of the pressure loss coefficients with an average relative deviation of 0.0003676 %, as shown in the figure 5.5.

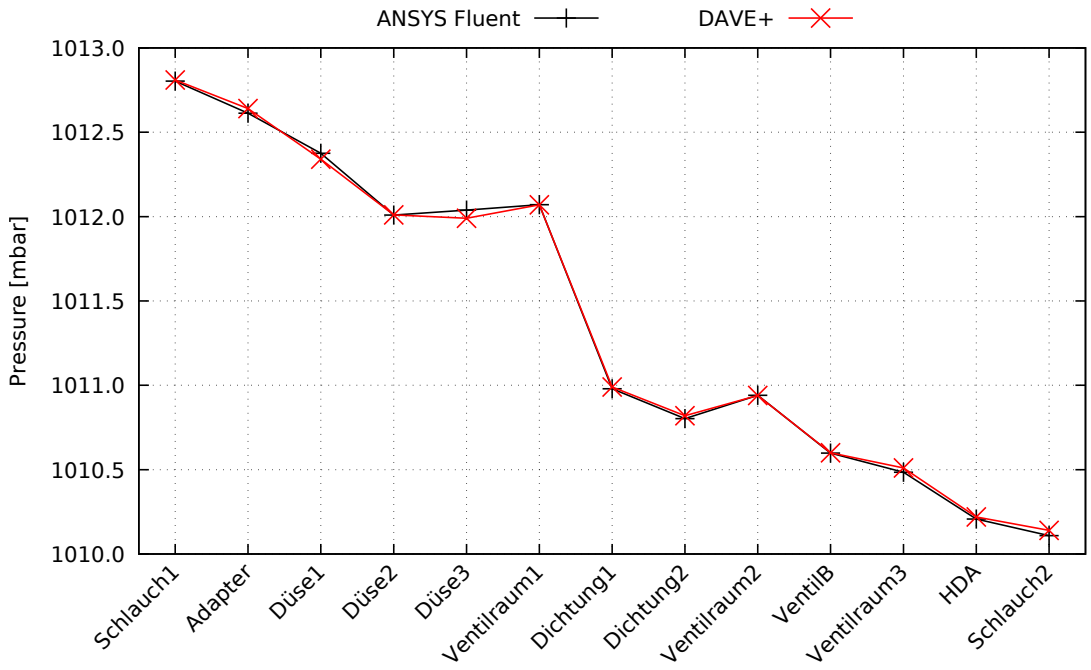

Figure 5.5: Comparison of pressure in the elements in the stationary 3D-1D-matching

The .mdl file for DAVE+ resulting from the stationary matching with the determined pressure loss coefficients will be referred to as *stationary-matched model* in the further work.

5.1.2.2 Periodic-stationary matching

Analogous to the stationary matching, a periodic-stationary matching is also carried out. Subsequently, a new calculation with periodic-stationary pressure boundary conditions is performed with the one-dimensional models from both calibrations and compared with 3D results under the same boundary conditions. The procedure of periodic-stationary matching and the subsequent comparison are shown schematically in figure 5.6.

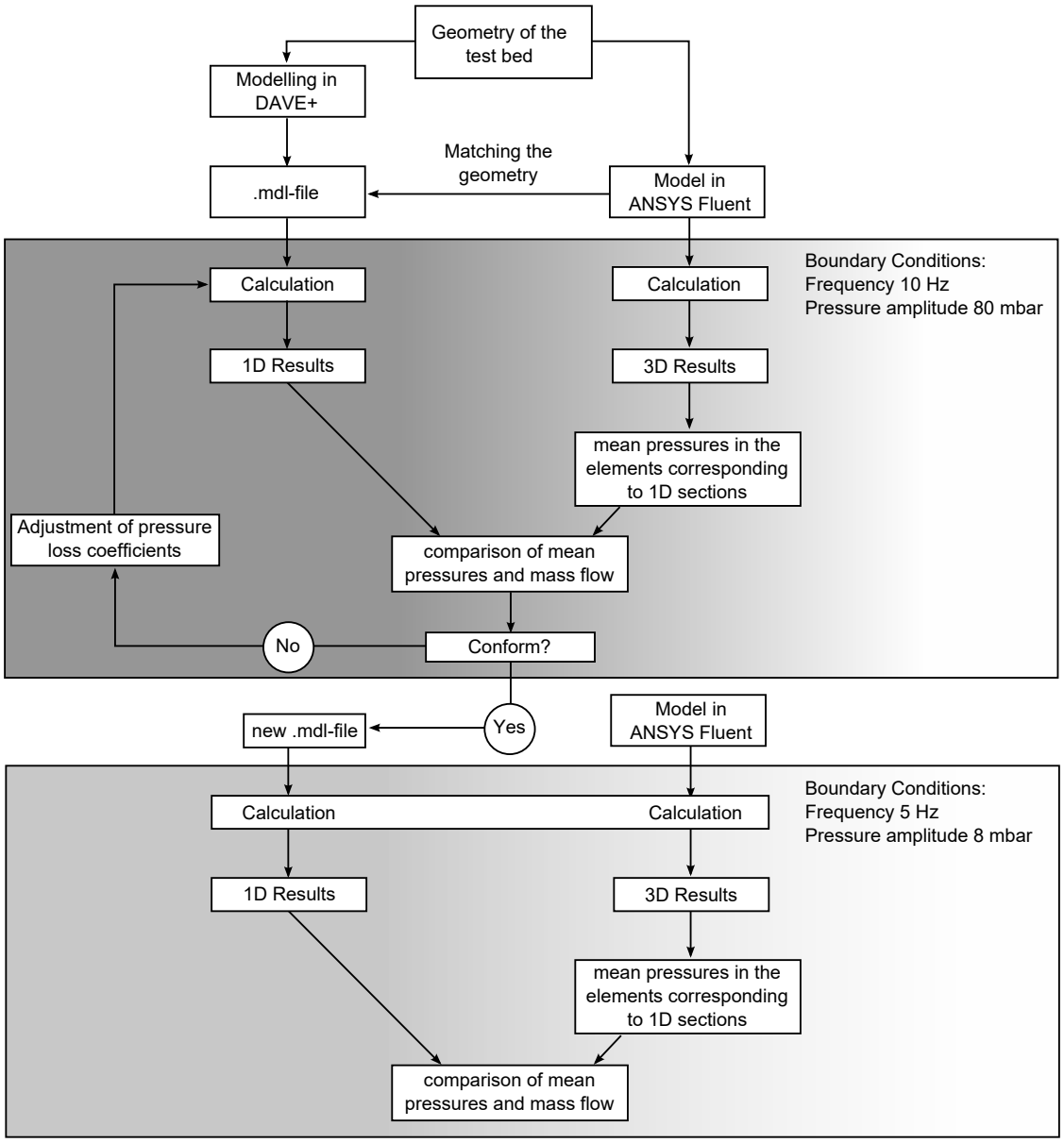

Figure 5.6: Schematic procedure at periodic-stationary matching and subsequent comparison of 1D and 3D calculations

A calculation for the sinusoidal pressure oscillation with the amplitude 80 mbar, a frequency of 10 Hz and an average pressure difference of 20 mbar is performed with the geometrically matched model in DAVE+ and with the 3D model in ANSYS Fluent. From the results of the three-dimensional computation, the average pressures are again calculated in sections corresponding to the average pressures in each element of the 1D model. Iteratively, the pressure loss coefficients of all elements in the 1D model are adapted in such a way that the average pressures of the 1D model correspond as far as possible to the average pressures previously determined in 3D. Other target variables are the mass flow and the disc movement. These are also decisively influenced by the pressure loss coefficients and thus are approximated by their change to the mass flow and the disc movement of the 3D simulation. Due to the transient boundary conditions, in contrast to the stationary case, the pressure profile across the elements is not constant in time, but changes with each time step. By way of example, the figure 5.7 shows the pressure over the elements for selected instances of a period. It is clearly visible that the pressure over the elements changes in time and the deviations at different times are of different sizes.

In order for the pressures, the disc movement and the mass flow in the elements to agree at all times, a new pressure loss coefficient would have to be determined for each element at every timestep. This would result in a dependence of the pressure loss coefficients on the crank angle or on the position of the disc. Physically, this is useful, but the effort to determine and implement a crank angle or disc movement dependent function for the pressure loss coefficients would be very high. In addition, Figure 5.7 shows that the deviations between 1D and 3D are very small during a large part of the period and are only increased for a short time when the valve is closed (about 300 ° KW). For this reason, an optimal, constant pressure loss coefficient is determined for each element using the method of the least squares. If the consistency is good, the calculated pressure loss coefficients are stored in a new *.mdl* file. The model with the pressure loss coefficients determined in this way is hereafter referred to as *periodically-stationary-matched model*. The consistency in this case can be seen in figure 5.8 on the basis of the mass flow and the disc movement. This results in an average relative deviation of 1.61 % in the disc movement and 3.19 % in the mass flow.

To check the quality of the matching processes, a further calculation with changed boundary conditions is carried out and compared without re-adjustment of the pressure loss coefficients with a corresponding three-dimensional calculation. A pressure oscillation of the form $p_{BC2,2}(\alpha) = p_{BC1} - \Delta p + \hat{p} \cdot sin(\alpha)$ at a frequency of 5 Hz with the pressure amplitude $\hat{p} = 800$ Pa and the mean pressure difference $\Delta p = 200$ Pa. This calculation is

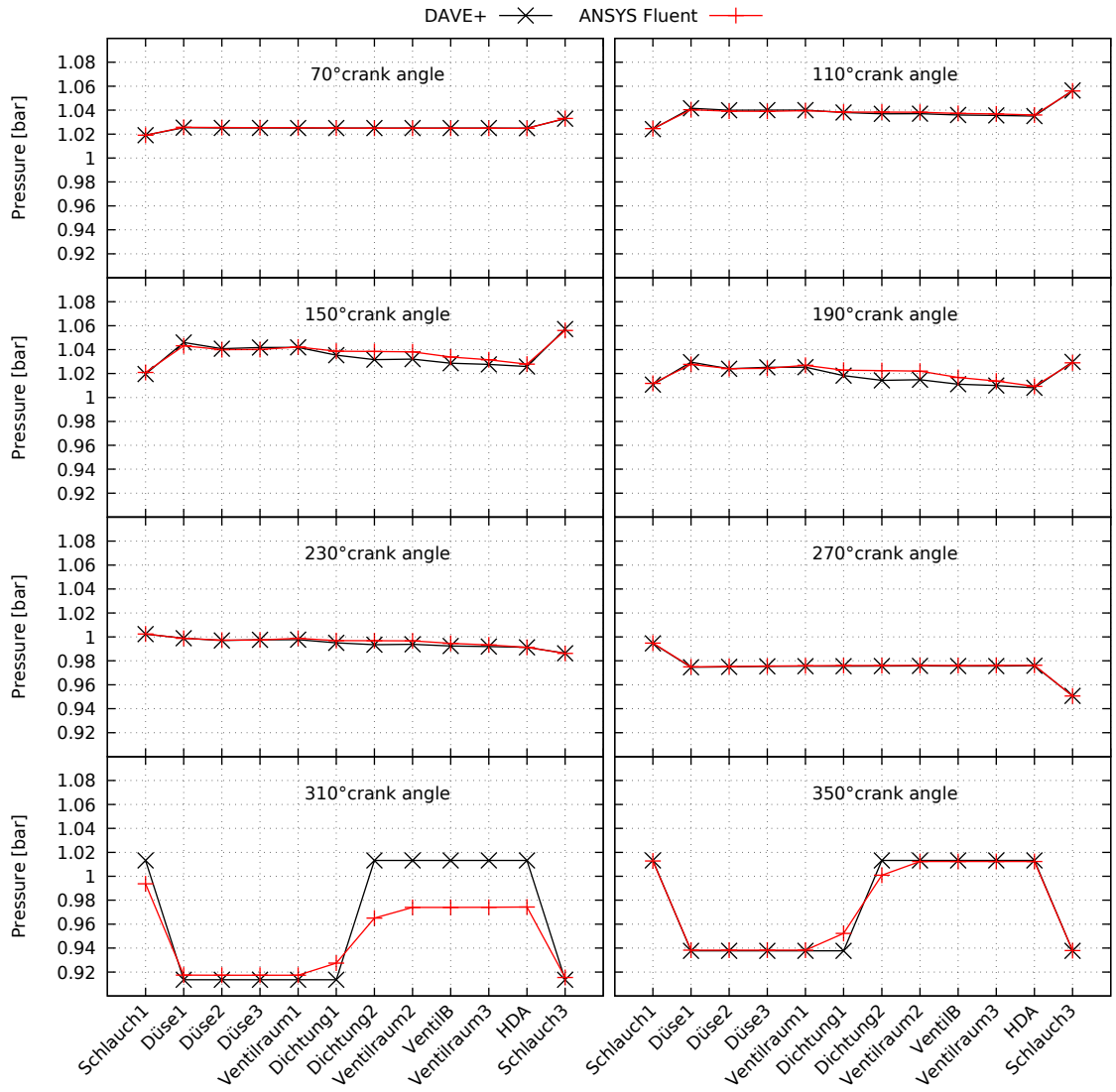

Figure 5.7: Pressure over the elements at selected instances of a periods for a simulation with the frequency 10 Hz and pressure amplitude 80 mbar

performed with both the *stationary* and the *periodic-stationary* model. A comparison of the calculation results from both 1D models and the 3D simulation are shown in figure 5.9.

It can be seen that the pressure loss coefficients from the *stationary* and the *periodic-stationary* matching give very similar results and a good approximation to the 3D calculations. The temporal progression of the disc position is very similar for all three types of calculation. The mean relative deviation with respect to the 3D calculation is around 2.256% for the simulation with the *stationary matched system* and 0.91% for the simulation with the *periodic-stationary matched model*. Qualitatively, the course of the mass flows agrees very well with all calculations. However, the relative deviation of the average mass

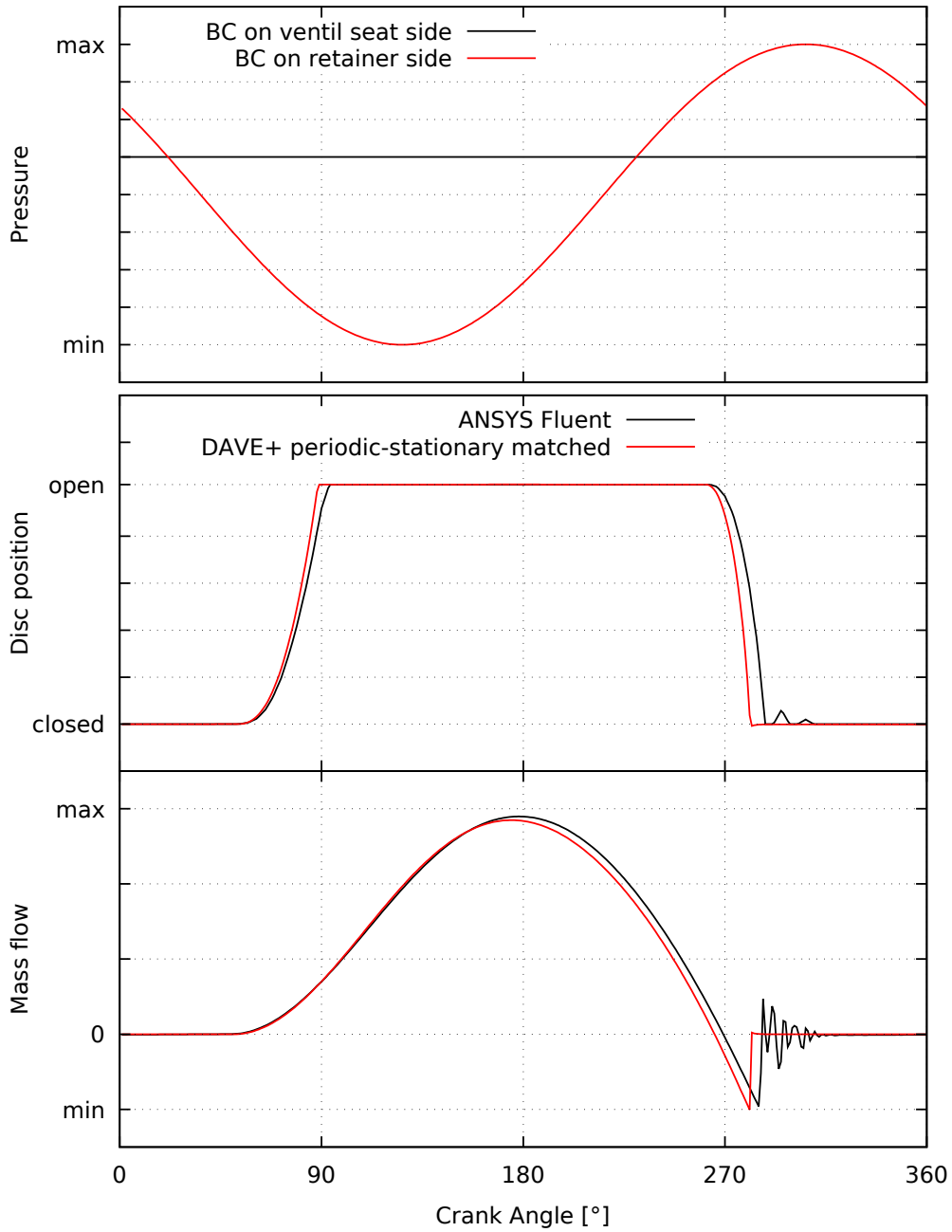

Figure 5.8: Pressure boundary conditions and simulation results of the periodic-stationary matching for the frequency 10 Hz and pressure amplitude 80 mbar (values surpressed due to confidentiality)

flow between the 3D simulation and the stationary-matched 1D model is about 13.4%, while there is a mean deviation of 15.2% between the 3D simulation and the calculation with the periodic-stationary 1D model. It can be seen that both target functions can not be fulfilled at the same time. Since the disc movement is pressure-controlled and is of

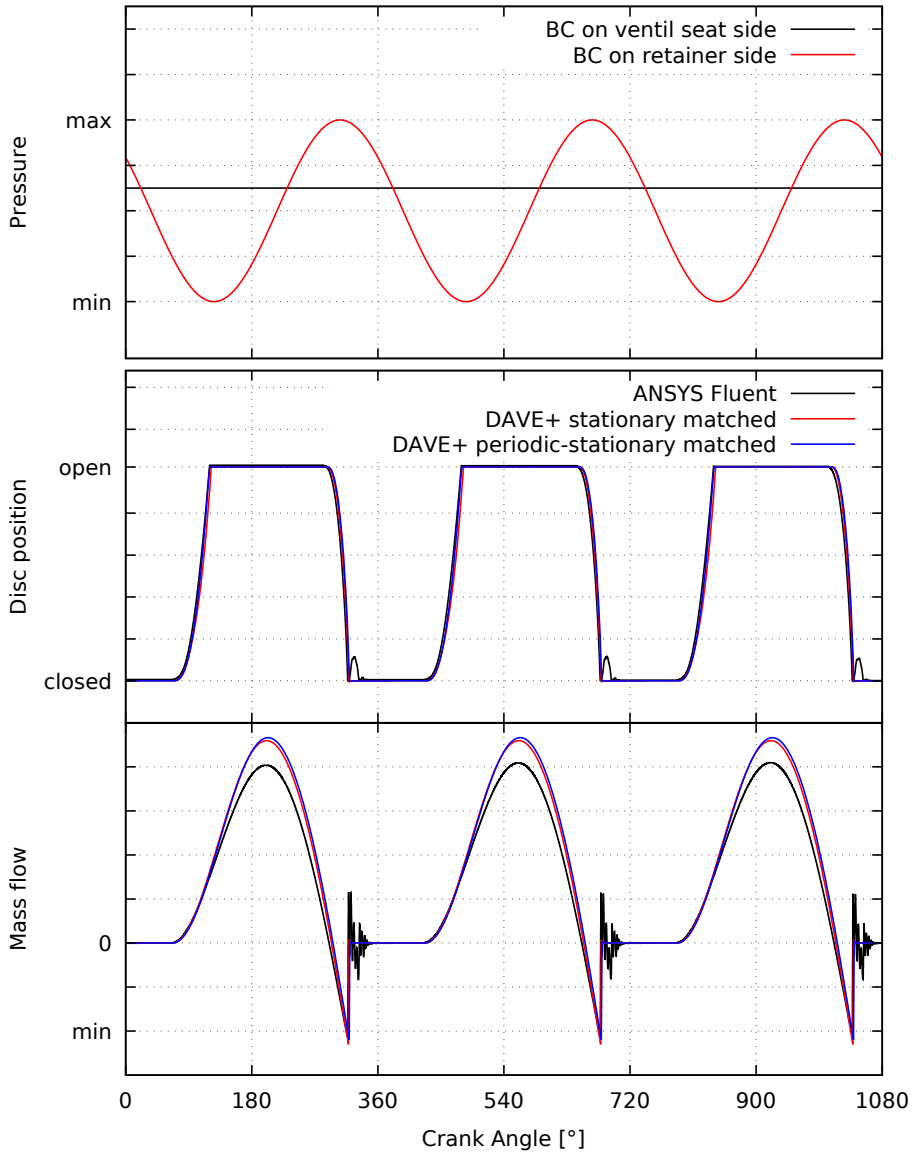

Figure 5.9: Comparison of simulation results; 3D simulation with ANSYS Fluent and 1D simulation with both *stationary matched* and *periodic-stationary matched* model in DAVE+ (values surpressed due to confidentiality)

greater interest since the geometry should be conform between 3D and 1D at any time, the mass flow is deliberately given a lower weighting at this point. With an average relative deviation of the disc position of 1.3% and the mass flow of 2.03%, the calculation results with the *stationary* and the *periodic-stationary* model are very close together. This is also evident from the pressure loss coefficients, which were determined during the adjustments and are listed in table 5.2.

Table 5.2: Pressure loss coefficients of all elements for the different 1D models

	Type of matching		
Element	no matching	stationary	periodic-stationary
Schlauch3	0,5	50,002081	50,002081
Düse1	0,5	1,1727922	1,1727922
Düse2	0,5	0,2347233	0,2347233
Düse3	0,5	0,6	0,6
Dichtung1	0,000305	2,505272	2
Dichtung2	0	0	0
VentilB	0	1,79	0,9
HDA	0,306661	2,8053067	2,8053067
Schlauch1	0,306661	30,002574	30,002574

It can be seen that the pressure loss coefficients differ only very slightly between *stationary* and *periodical-stationary* matching. Towards the unadjusted model, on the other hand, there are large differences. The simulation results and the pressure loss coefficients show the necessity of a matching. At the same time, however, the simpler *stationary* matching seems to be sufficiently accurate for the simulation of the test bed, and the more complex *periodic-stationary* matching therefore does not appear to be necessary.

However, since the overriding goal is the integration of the valve model *in the carburetor* instead of *on the test bed*, it is necessary to check whether the stationary pressure loss coefficients also provide sufficiently accurate results in the carburetor or, under these boundary conditions, the periodic-stationary matching is necessary. Since the main difference from the test bed to the carburetor valve is in the geometry of the connecting lines, this is adjusted step by step to the carburetor dimensions. In the case of the 1D simulation, the tube lengths are shortened stepwise upstream and downstream in steps of 10% starting from the actual length at the test bed. The original length of the hose upstream of the valve is 464 mm, the hose downstream of the valve 364 mm. This parameter study is carried out for the three calculation models *without adjustment*, with *stationary matching* and with *periodic-stationary matching*. All of them are geometrically exactly identical and differ only in the pressure loss coefficients used according to table 5.2. This results in the graphs in Figure 5.10, which represent the mass flows of the three models depending on the hose length.

From this parameter study it becomes clear that the hose length has a great influence on the calculation results. On the one hand, the mass flow increases as the hose length is shortened. On the other hand, the curves with different pressure loss coefficients are much closer together in the case of long hoses than in short hoses. This is also clear considering

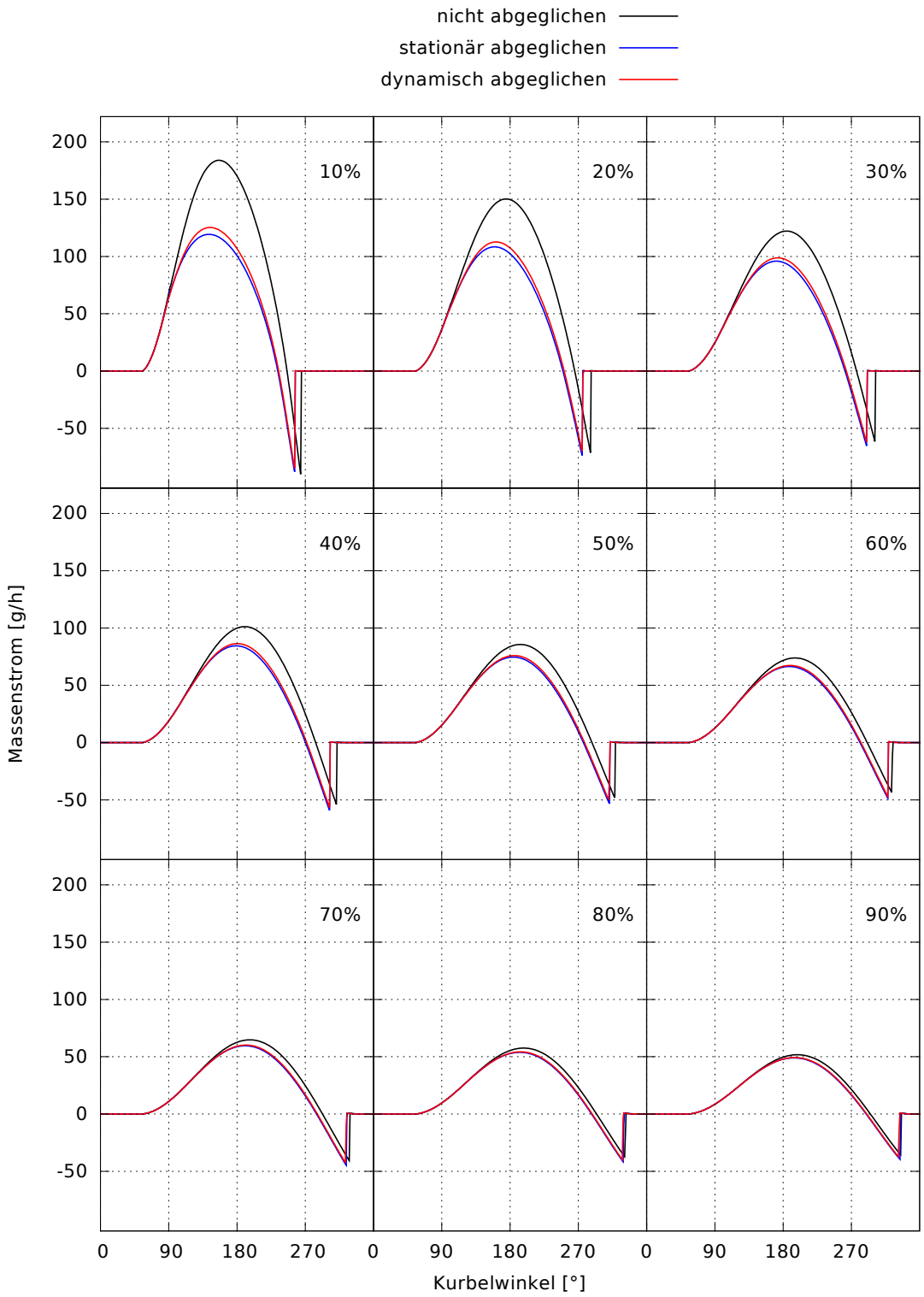

Figure 5.10: Mass flows for different hose lengths with same boundary conditions; the labels within each graph specify the percentaged length of the hoses with respect to the actual lengths at the test bed.

the average mass flows in Figure 5.11. The average mass flow increases for all calculation models for shorter hoses. Also, the average mass flows show big deviations for short hoses, so the different pressure loss coefficients have a great influence in short hoses. The longer the hoses are, the closer the mean mass flows of the different models are to each other. This is due to the inertia of the fluid. With short hose lengths, there is less fluid in the system, the inertia of which must be overcome. In the case of long hoses, on the other hand, the inertia of the system is so great that its effect prevails over the effect of the pressure loss coefficients. For the short distances in the carburetor, the pressure loss coefficients must therefore be selected as close as possible to the results of the 3D simulations. However, the results of the *stationary* and *periodic-stationary* models are so close to each other that the *stationary* matching is sufficient for the short distances corresponding to the distances in the carburetor and the *periodic-stationary* adjustment is not necessary.

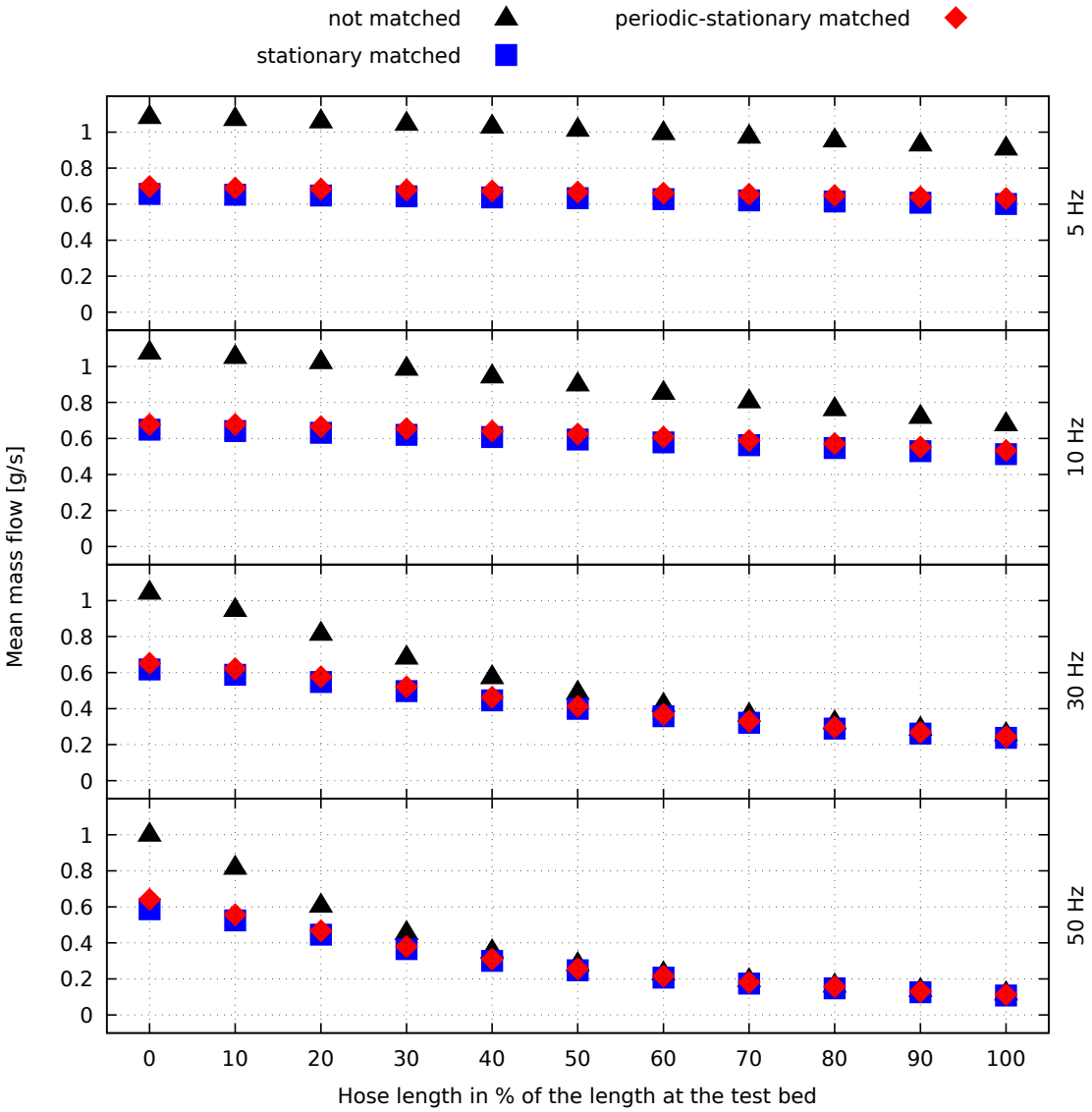

Figure 5.11: Mean mass flows with respect to the length of the hoses for all three models and different frequencies

5.2 Comparison of measurements and 1D simulations

In addition to validation using the 3D calculations, a validation of the 1D simulation is also carried out on the basis of measurements at the test bed. For this purpose, the periodic-stationary measurements described in chapter 4 are first used. These lead to further measurements under stationary conditions at the test bed with a corresponding comparison with 1D calculation results.

5.2.1 Periodic-stationary operation

The measurements from chapter 4 are used to validate periodic-stationary operation. For this purpose, the section of the test bed marked in the figure 5.12 is modeled in DAVE+, which extends from the overflow basin to the pressure measuring point downstream of the valve. This type of modeling simplifies the definition of the boundary conditions in 1D by directly entering the measured pressures.

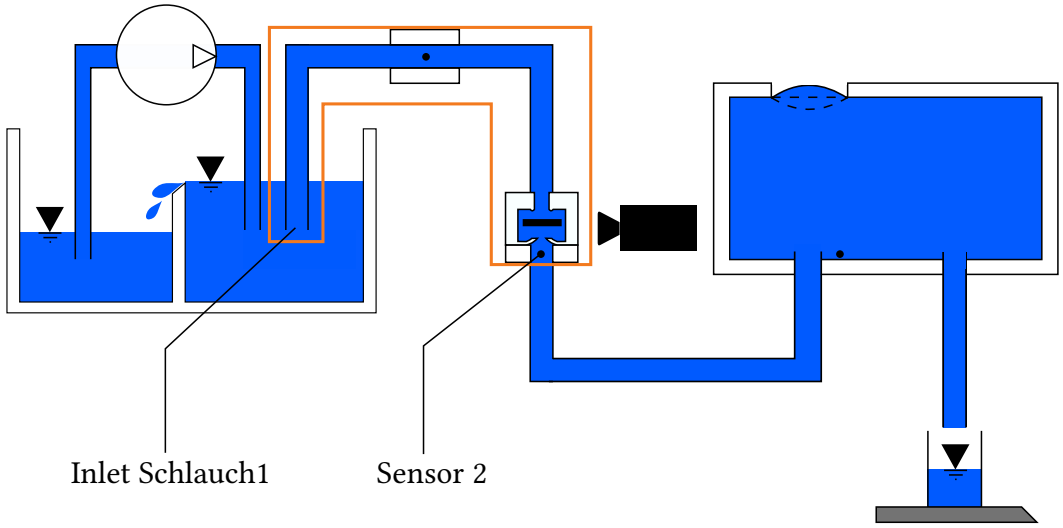

Figure 5.12: Section of the test bed modelled in DAVE+ for validation purpose

The comparison of 1D calculations and measurements is performed according to the scheme shown in Figure 5.13.

For this purpose, the pressure profile measured by *sensor 2* is determined as a pressure boundary condition downstream, i.e. on the retainer side of the valve. A constant pressure p_{const} is defined upstream of the valve at the entry into the *Schlauch1* from the overflow tank. As a connection between the boundary conditions and the valve in the 1D model, the hoses are used as line elements with the actual length at the test stand. In this way,

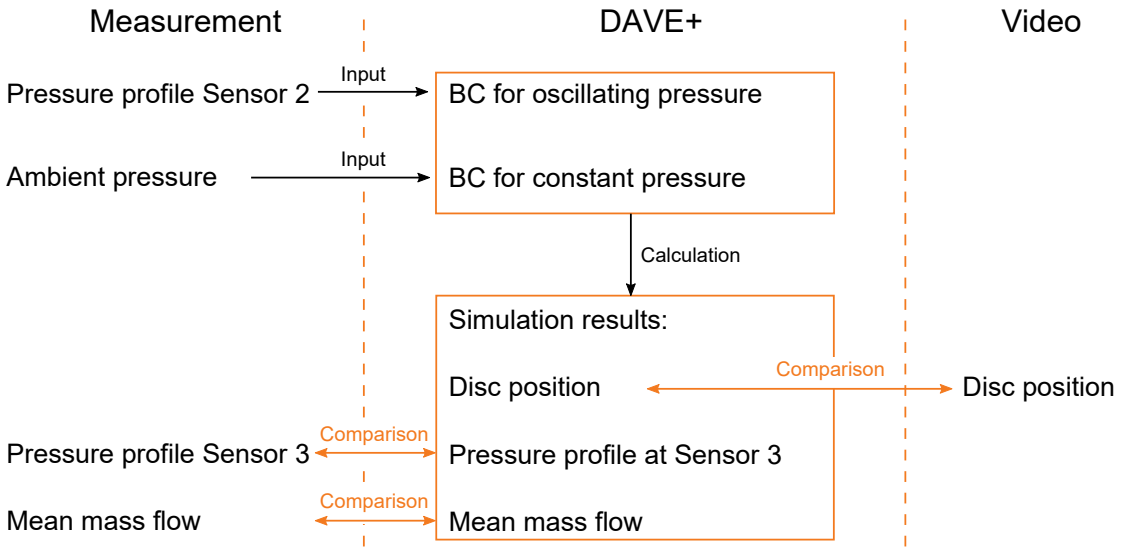

Figure 5.13: Scheme of approach at the comparison of measurements and 1D simulations

a one-dimensional calculation is performed for each measured experiment from chapter 4, table 4.1. Based on a comparison of the calculation results and measured values, it is judged whether the 1D simulation, given the pressure signal at *pressure measuring point 2*, represents the behavior of the valve on the test bed with sufficient accuracy. Three comparison parameters are used for this purpose. One is the motion curve of the disc which is on the one hand derived from the high-speed video of all experiments and on the other hand calculated in DAVE+. In addition, the calculated and measured mean mass flow is compared. The third comparison parameter is the temporal course of the pressure, which *Sensor 3* records in the measurement and calculates DAVE+ for the same point in the system.

As an example, this comparison for *Experiment 8* with the frequency 53 Hz is considered in more detail. Figure 5.14 shows the measured pressure curve at *Sensor 2*, which is used as the pressure boundary condition for the 1D calculation. In addition, the time profiles of the disc position are shown, which are determined from both this calculation and the video.

It can be seen that the disc movements match each other qualitatively well. However, a clear difference in the opening and closing speed can be seen. The opening process takes place much faster in the movement from the video than in the calculation. The closing process also reflects the faster movement of the disc in the video. Overall, the valve is closed a shorter period of time in the 1D calculation, but is also shorter fully opened than on the test bed.

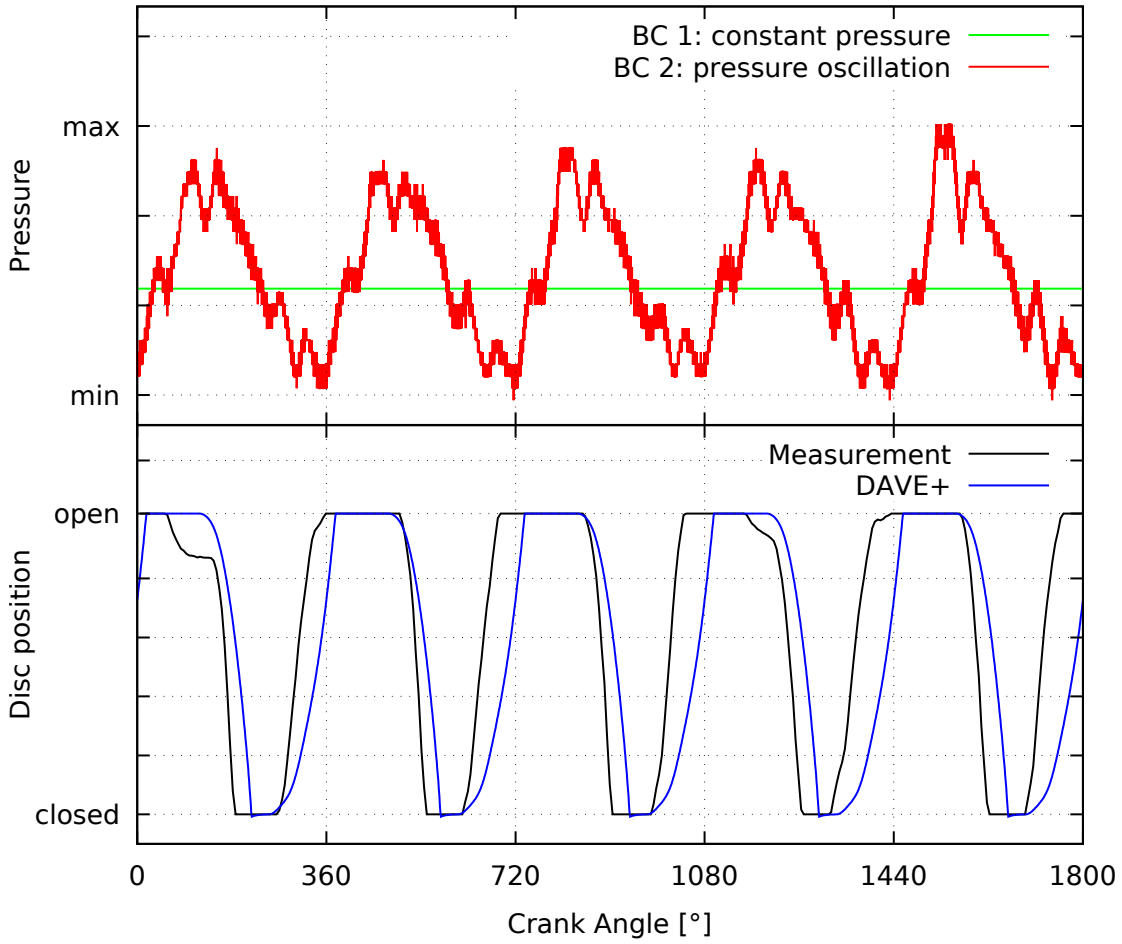

Figure 5.14: Measured Pressure at *Sensor 2* in *Experiment 8* as pressure boundary condition for 1D simulation; comparison of the disc movement from highspeed video and simulation in DAVE+ (values surpressed due to confidentiality)

For some measurements, however, using the ambient pressure p_U as a constant boundary condition, disc movements are calculated which do not fit the motion of the disc derived from the video. An example is shown in Figure 5.15a for *Experiment 13*. In these measurements, however, an offset of the constant pressure in the boundary condition can be used to qualitatively approximate the disc movement from the video, as shown in the figure 5.15b.

The constant pressures used in DAVE+ for each experiment as constant pressure boundary conditions, which have led to a disc movement similar to the video, are listed in table 5.3. It becomes clear that the necessary offset is not a systematic deviation.

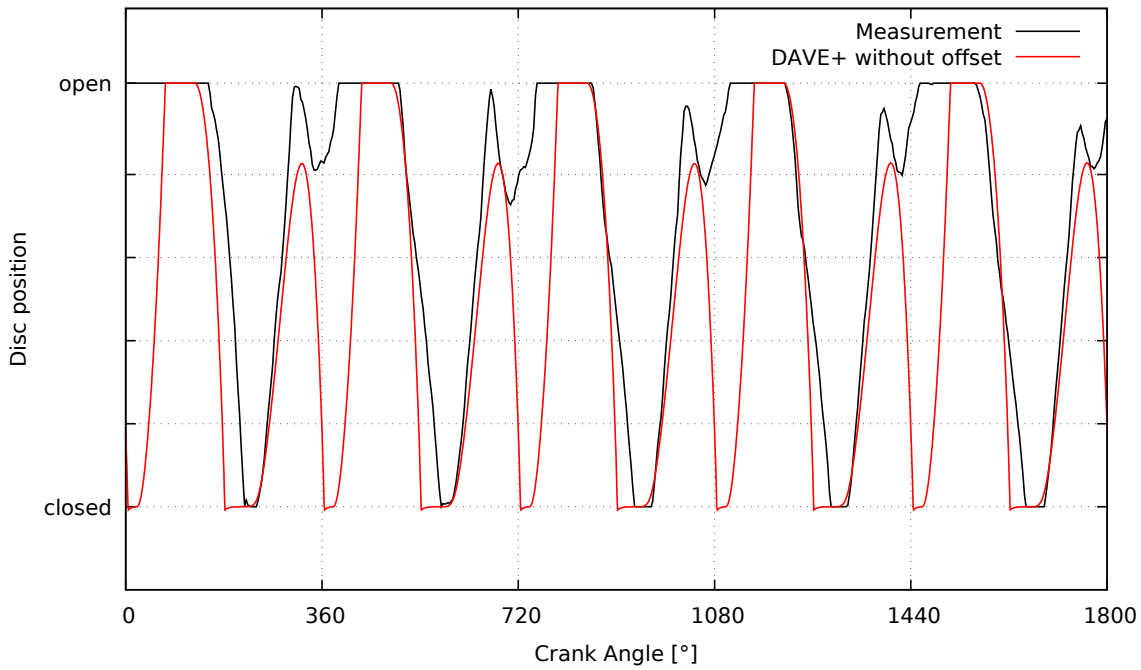

(a) DAVE+ calculation without pressure offset

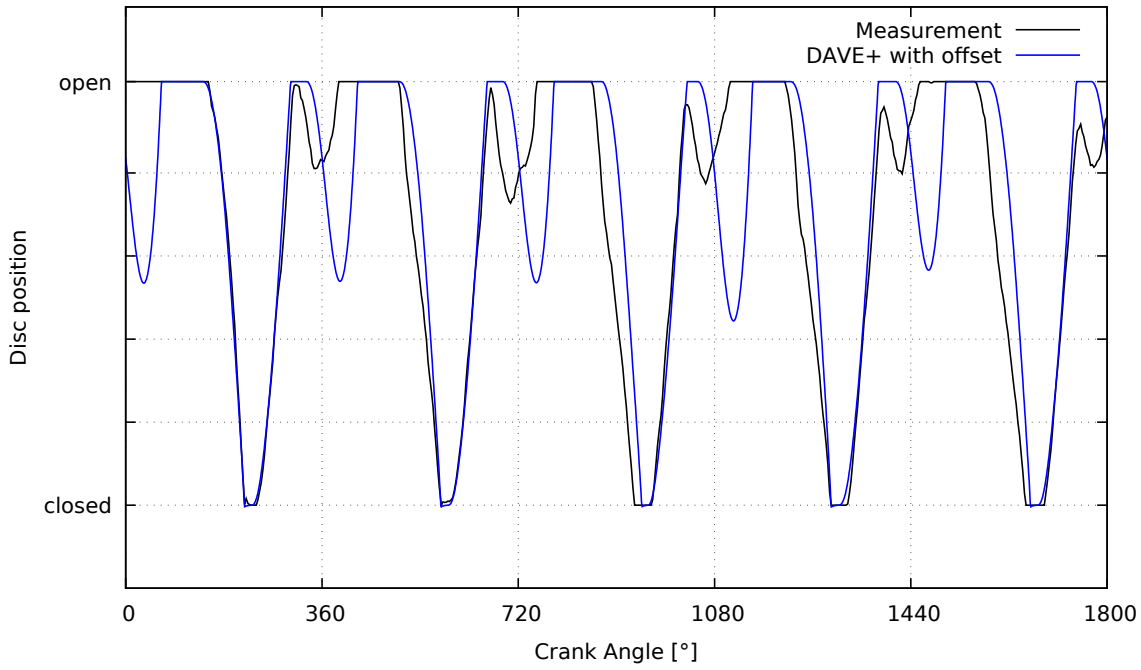

(b) DAVE+ calculation with pressure offset

Figure 5.15: Disc movement in Experiment 13 compared between measurement and DAVE+ without and with pressure offset (values surpressed due to confidentiality)

Table 5.3: Changed constant pressure boundary conditions, which lead to disc movements which are comparable to the highspeed videos

Name	pressure boundary condition constant [mbar]
Experiment1	951
Experiment2	953
Experiment3	957
Experiment4	963
Experiment5	953
Experiment6	966
Experiment7	965
Experiment8	964
Experiment9	972
Experiment10	985
Experiment11	981
Experiment12	984
Experiment13	981
Experiment14	-
Experiment15	979
Experiment16	-
Experiment17	986
Experiment18	983

Contrary to the comparison with 3D simulations, for the comparison of 1D simulations and measurements the mass flow through the valve is more important than the exact movement of the disc. Therefore, it is necessary to determine how much the difference in the disc position affects the mass flow through the valve. To do this, firstly the calculated and measured mean mass flow of the test series in table 5.4 are compared.

It should be pointed out that the very high mass flow in Experiment *2* is based on the fact that the disc remains attached to the retainer in this experiment. Since the differences between the average mass flows from calculation and measurement with relative deviations from 11% to 99% are very large, possible causes are discussed in the following. For this purpose, the test bed is simplified as far as possible and operated in a stationary manner. The measurements are then compared with calculations in DAVE+.

5.2.2 Stationary operation

First, the 1D model is adapted to the test bed performing stationary measurements. For stationary operation, the valve, the short hose pieces and the *pressure measuring points 1*

Table 5.4: Comparison of mean mass flows measured and calculated

	mean mass flow [g/s]	
Name	Measurement	DAVE+
Experiment1	0,2	0,138
Experiment2	0,73	0,064
Experiment3	0,26	0,153
Experiment4	0,166	0,147
Experiment5	0,26	0,080
Experiment6	0,26	0,036
Experiment7	0,33	0,032
Experiment8	0,4	0,131
Experiment9	0,4	0,001
Experiment10	0,466	0,084
Experiment11	0,2	0,139
Experiment12	0,133	0,183
Experiment13	0,166	0,133
Experiment14	0,333	-
Experiment15	0,133	0,019
Experiment16	0,333	-
Experiment17	0,4	0,004
Experiment18	0,133	0,157

and 2 are replaced by a long hose at the test stand. The length of this hose corresponds to the total length of the replaced elements. The electric motor is switched off during stationary operation so that the volume of the pressure vessel is constant. This structure is referred to in the following as *reduced system without valve* and is shown in figure 5.16.

By adjusting the height difference between the water level of the overflow basin and the end of the discharge hose, a constant mass flow is set and measured. For the modeling in DAVE+, the hoses are divided into several pipes, each of which represents vertical or horizontal sections of the hose. The fluid in the vertical ducts is charged with the acceleration due to gravity in the form of an acceleration factor *pipename*.B = $\pm 9.81 N/kg$. Since a stationary point is examined, there is only one flow direction from the overflow basin in the direction of the pressure vessel. Accordingly, the acceleration factor for the vertical pipes (1) and (3) is negative because the acceleration due to gravity counteracts the moving direction of the fluid. In the other vertical lines (2) and (4), however, the acceleration due to gravity is positively defined since its direction coincides with the flow direction. No gravitational acceleration acts on the fluid in the horizontal line sections. The hose division into horizontal and vertical pieces is always carried out in such a way

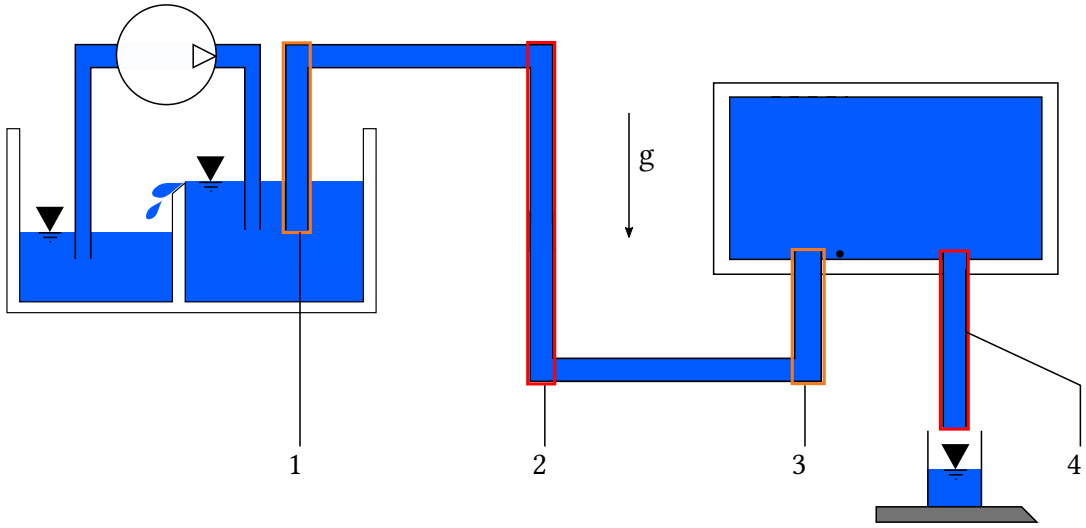

Figure 5.16: Structure of the reduced system without valve

that the total length L of the hose and the height differences are maintained. This principle is illustrated in simplified form in Figure 5.17.

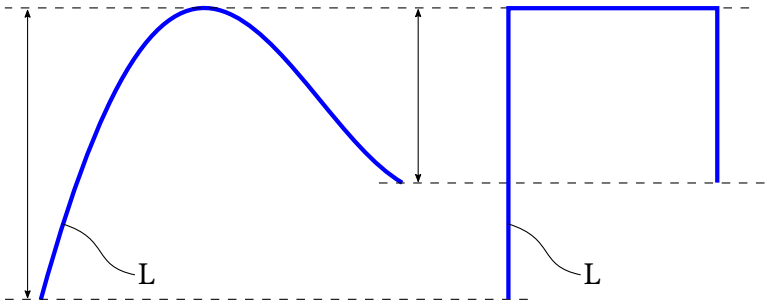

Figure 5.17: Division of hoses into vertical and horizontal sections

For the elevation difference $\Delta h = 400mm$, a mass flow $\dot{m} = 7.331$ g/s and at sensor 1 a pressure of $p_{Sensor1} = 984$ mbar is measured. The ambient pressure p_U is 987 mbar. This measurement is used to adjust the pressure loss coefficients for the transition from the overflow basin into the hose, for the hose itself and for the transition from the hose into the pressure vessel so that the measured values are taken into account in the calculation. Subsequently, two further measurements with a changed elevation difference are used to validate the determined pressure loss coefficients. Table 5.5 shows the results of this validation.

The model for the *reduced system without valve* is validated with the very slight deviations in both pressures and mass flows. In a further step, the valve is reinstalled, but the pressure

Table 5.5: Comparison of measured and calculated values for the reduced test bed without valve

		Measurement	DAVE+	relative deviation
Measurement 1	Pressure Sensor1	984,22 mbar	984,54 mbar	0,0033%
	Mass flow	7,341 g/s	7,347 g/s	0,0817%
Measurement 2	Pressure Sensor1	984,10 mbar	982,65 mbar	-0,1473%
	Mass flow	6,316 g/s	6,192 g/s	-2,0026%
Measurement 3	Pressure Sensor1	982,98 mbar	981,7 mbar	-0,1302%
	Mass flow	5,419 g/s	5,546 g/s	2,2900%

vessel and discharge hose are removed. This structure is hereinafter referred to as *reduced system with valve* and is shown in the figure 5.18.

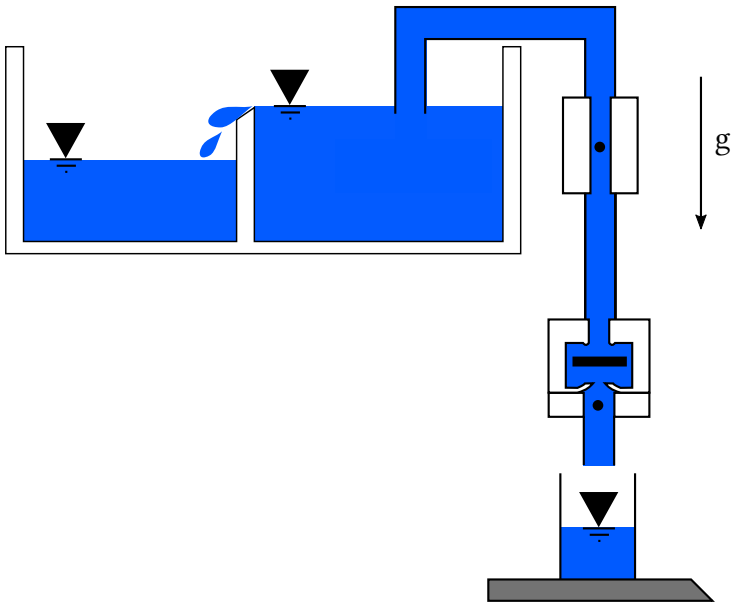

Figure 5.18: Structure of the reduced system with valve

Again, a measurement is used to adjust the pressure loss coefficients of the additional elements which have not yet been determined by the 3D simulation or the reduced system without a valve. Such an additional element is, for example, the cross-sectional constriction through the adapter for the pressure sensor upstream of the valve. The values from the *stationary* match 1D-3D from table 5.2 are used for the pressure loss coefficients within the valve. For the hoses, the pressure loss coefficients of the *reduced system without valve* are determined. Table 5.6 shows the measured and calculated values for the *reduced model with valve*.

Table 5.6: Comparison of measured and calculated values for the reduced test bed with valve

	Measurement	DAVE+	relative deviation
Pressure Sensor2	983,02 mbar	982,91 mbar	-0,0112%
Pressure Sensor3	1006,27 mbar	1005,59 mbar	-0,0676%
Mass flow	0,626 g/s	0,629 g/s	-0,4792%

Thus, with the aid of the two reduced systems, pressure loss coefficients are determined for all elements of the complete system. These are taken into the model for periodic-stationary calculations. This model will be referred to as the *measurement-matched model*. This again simulates the periodic-stationary measurements from chapter 4. A further slight approximation of the mean mass flows to the measured values is shown. This can be seen in the table 5.7 in comparison to the measured values and the 1D model, which has been adjusted from 3D in the stationary state, using the experiments *5* to *8*.

Table 5.7: Comparison of mean mass flows from measurements and calculations with the 3D stationary matched model and the stationary measurement-matched model

	Measurement	3D stationary matched	measurement-matched
Experiment 5	0,26 g/s	0,074 g/s	0,102 g/s
Experiment 6	0,26 g/s	0,038 g/s	0,071 g/s
Experiment 7	0,33 g/s	0,035 g/s	0,058 g/s
Experiment 8	0,4 g/s	0,13 g/s	0,15 g/s

Nevertheless, the differences in mean mass flows are very large, which is examined in more detail below.

5.2.3 Analysis of potential causes for the deviations

When the simulation results are examined in detail, it becomes clear that the low mass flow is mainly due to a strong backflow through the valve. This is shown in Figure 5.19. The area below the x-axis enclosed by the curve corresponds to the mass of water which flows through the valve counter to the desired flow direction.

With a disc movement in DAVE+, which follows the mass flow faster, a significant increase in the average mass flow would be expected. In this case, the area enclosed by the curve above the x-axis is larger by a faster opening movement, and the area under the x-axis is smaller. This results in a greater mass flow in the desired direction through

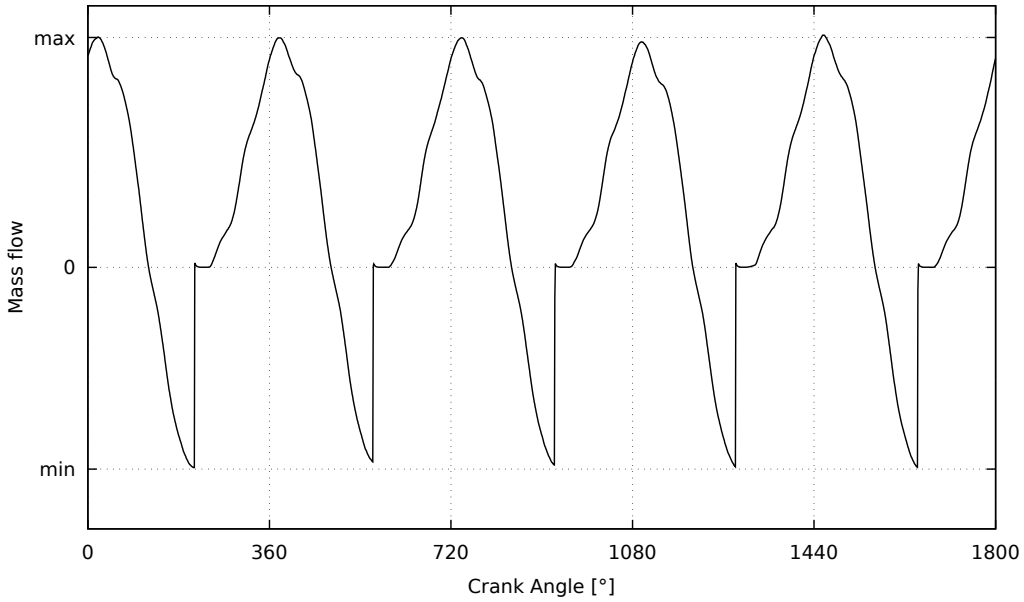

Figure 5.19: Temporal course of mass flow from simulation for *experiment 8*

the valve caused by the fact that the valve is fully open for a longer period of time and a smaller mass flow counter to the desired flow direction in that the valve closes faster during a backflow movement. When adjusting the closing time t_2 in the simulation to the earlier closing time t_1 from the measurement in each period, the reduction of the backflow becomes clear as shown in figure 5.20. In this case, the average mass flow already increases by 17% to 0.189 g/s. However, this value is still significantly distant from the measured 0.4 g/s.

In addition to the uncertainties on the model side, the difference in mean mass flow between measurement and simulation can also be due to measurement errors. It is possible that the measured mass flow is probably too high because of leakages in the hoses and the pressure vessel. After a short measuring time, it can already be seen that an air bubble has formed in the initially air-free pressure vessel with increasing volume $V_{air}(t)$. The same volume of water was thus displaced from the air out of the pressure vessel. On the assumption that only a very small backflow takes place through the valve, this displaced volume flows into the measuring container on the scale. Accordingly, the mass is weighed by $m_{scale} = \rho_{water} \cdot (V_{valve} + V_{air})$ where V_{valve} is the water volume that actually flows through the valve in desired direction. It follows that the mass flowed through the valve $m_{valve} = \rho_{water} \cdot V_{valve}$ is less than the weighed mass

$$m_{scale} = \rho_{water} \cdot (V_{air} + V_{valve}) > \rho_{water} \cdot V_{valve} = m_{valve}. \tag{5.2}$$

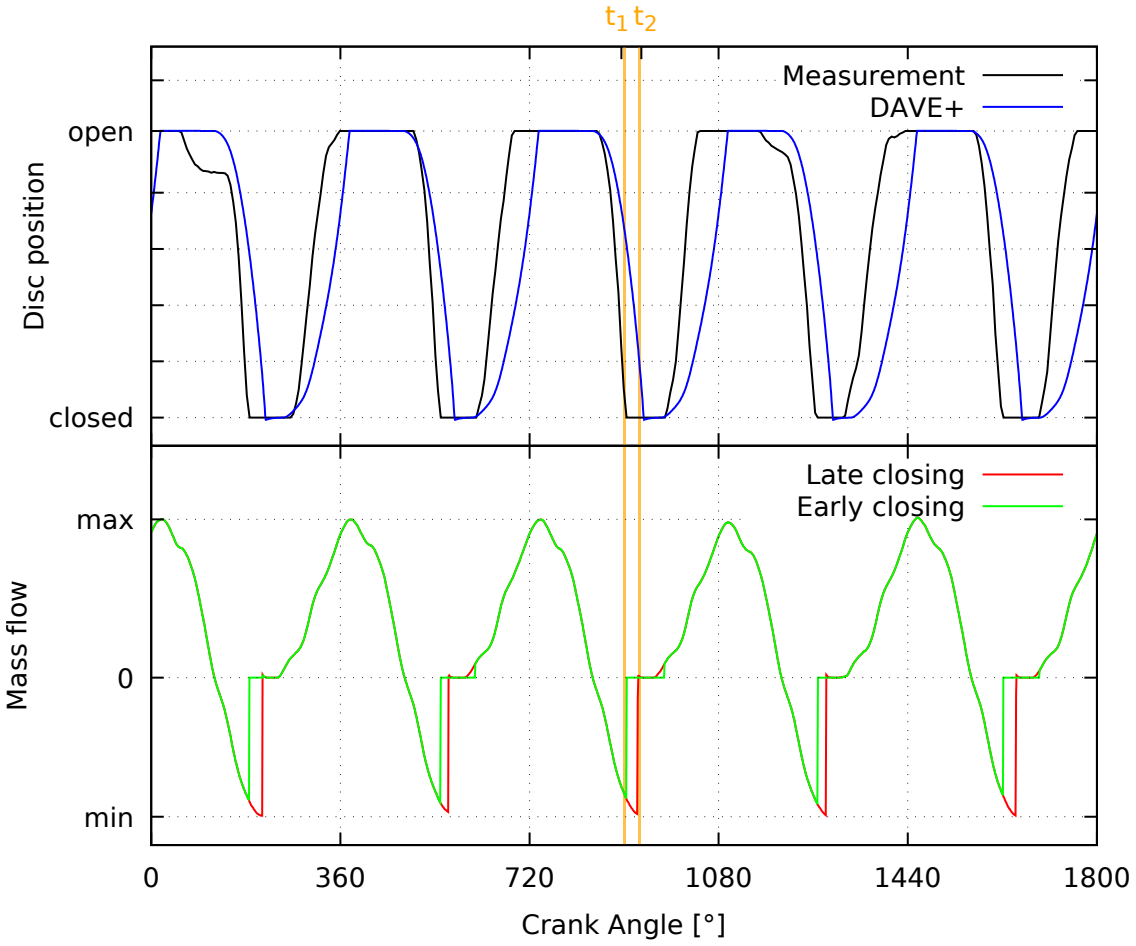

Figure 5.20: Calculative reduction of backflow due to adapting the closing time in experiment 8 (values surpressed due to confidentiality)

This effect is to be excluded in following measurements,by filling the pressure vessel with water again completely after each measurement run. The filled volume should then be recorded and the corresponding mass removed from the mass in the measuring container. On the other hand, the mass flow at the test bed can only be measured as a mean value over time. In doing so, efforts must be made to measure over a period as long as possible and to carry out several measurement repetitions. As explained in chapter 4, the speed of the motor fluctuates considerably. Therefore, no rotational speed can be kept constant for a sufficiently long time. In order to obtain reliable measured values for the mass flow, a new concept for the test bed is necessary, which provides the possibility of keeping the frequency of the pressure oscillation constant over a long period of time. The concept is described in chapter 6.2.

6 Conclusion and outlook

On the basis of the previous studies, the model quality of the 1D model is evaluated in this chapter. From this assessment, possible steps for future investigations can be derived, which are also contained in this chapter. This includes the change of the test bed as well as an approach to improve the quality of the 1D model.

6.1 Evaluation of the model quality

It is clear from the observations made that the principle of operation of the model is fulfilled. All possible positions of the disc can be reproduced. Stationary flows through the valve can also be imaged in comparison to 3D simulations as well as in comparison to measurements. The imaging of periodic-stationary states leads to only partially satisfactory results.
The criteria relevant to the model assessment are the pressures, the disc movement and the mass flow. A validation based on the 3D simulations shows that the relative deviations in the disc movement are very low with 2% and in the mass flow with a maximum of 15%. Accordingly, it is to be assumed that the 1D model takes into account the essential effects of the 3D simulation and provides corresponding results. Thus one-dimensional simulation can already be used in a very short time to obtain insights that can be achieved three-dimensionally only with greater expenditure of time.
Compared to the measurements, however, there is a high deviation with respect to the mass flow. The 1D model can not reliably simulate the processes at the test bed with the current design. The high consistency of the 1D and 3D simulation suggests that either both numerical models do not consider significant effects at the test bed, or that the measurements are strongly defective. There is also the possibility that the adjustment of the 1D model to the stationary measurements only provides equal mass flows coincidentally. Therefore, it is important to find out whether other combinations of the pressure loss coefficients lead to a satisfactory image of both the stationary and the periodic-stationary measurement.

6.2 Further development of the test bed

Instead of the mechanical deflection of the membrane from the eccentric driven by the electric motor, the membrane is now deflected by means of a subwoofer. The following section briefly discusses the operation of a subwoofer. A subwoofer is a loudspeaker, which in the case of music systems reproduces the low frequencies of about 25-200Hz, which corresponds to the bass. The simplified structure of a subwoofer is shown in Figure 6.1.

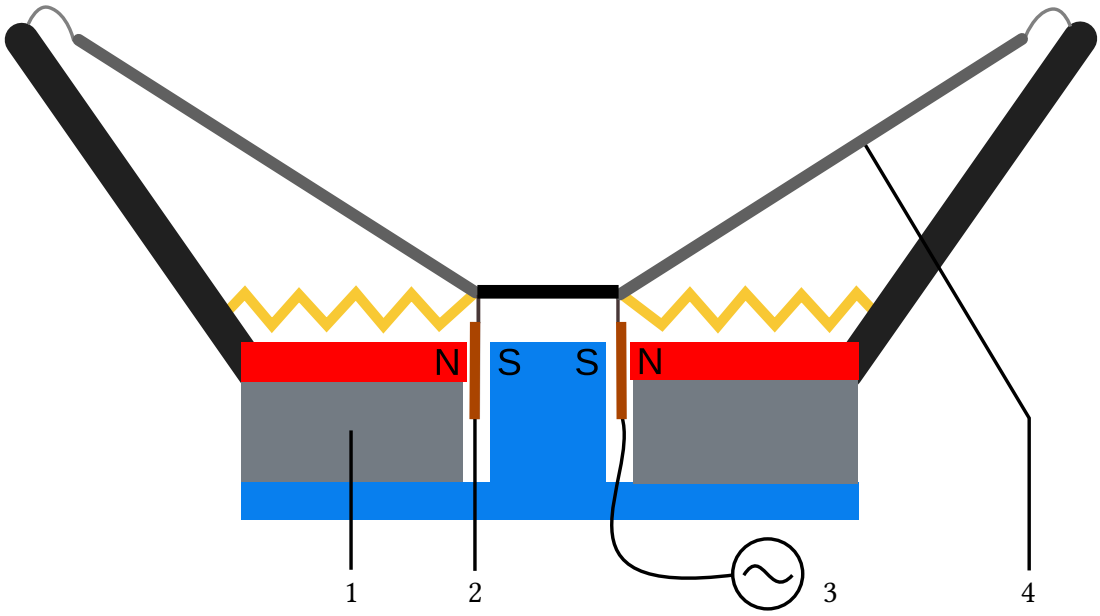

Figure 6.1: Strongly simplified structure of a subwoofer following [Wik]

The principle of a loudspeaker is based on the fact that a coil through which an alternating current flows oscillates in the magnetic field of a permanent magnet. This oscillating translational movement deflects a membrane, which then displaces a certain air volume depending on the stroke and diameter, which leads to a sound pressure and thus to an audible sound. The translatory deflection of the oscillating coil is based on the Lorentz force F_L, which is calculated from the current strength I, the length of the coil wire l and the strength of the magnetic field B:

$$\vec{F_L} = I \int d\vec{l} \times \vec{B} \tag{6.1}$$

As can be seen from the formula (6.1), the Lorentz force and thus the deflection of the oscillation coil is directly dependent on the current strength [Hei16]. In practice, a higher current intensity means a larger displaced air volume and thus a higher volume of the

sound. The pitch of the reproduced sound is determined by the frequency of the applied voltage. Low frequencies lead to deep tones. The applied current can influence the deflection of the oscillating coil. The oscillation frequency can also be determined by the frequency of the applied alternating voltage. This makes a subwoofer suitable for the measurements on the test bed. The translatory movement of the oscillating coil is not intended to be used for displacing air by means of the loudspeaker membrane, but rather the deflection of the membrane on the pressure vessel of the test bed (Figure 4.1, 4) and thus the displacement of water. Since, for this purpose, the counter pressure of the water in the container is significantly greater than the counter pressure of the air in free space, it was firstly estimated whether a subwoofer can apply a sufficiently large force. For this purpose, a simple 1D model was created in DAVE+, which roughly simulates the conditions at the test bed. This model is used to simulate the entire test bed shown in Figure 6.2.

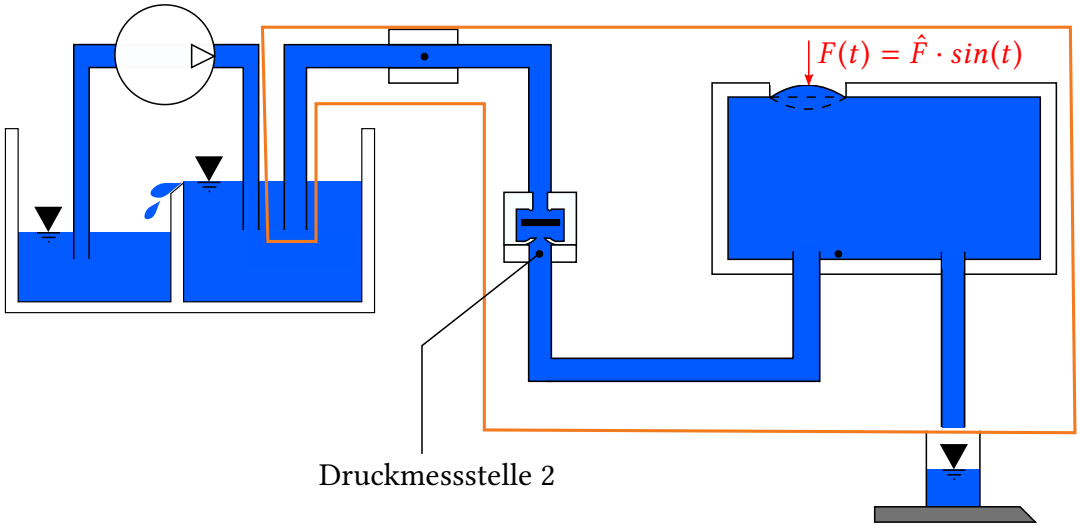

Figure 6.2: Modelled part of the test bed for the estimation of the force amplitude needed for desired pressures

The pressure vessel was represented by a volume, which is separated from the environment by a flexible wall. A sinusoidal force $F(t) = \hat{F} \cdot sin(t)$, which deflects the membrane upwards and downwards and thus produces pressure oscillations. The amplitude $\hat{F}$ of this force is assumed as the force to be applied by the subwoofer. In the case of a variation of this force amplitude, the generated pressure amplitude which is established at the pressure measuring point 2 is observed. In this rough estimate, a required force amplitude of about 30 N for the generation of pressure oscillations with the desired amplitude [redacted]* mbar

*Information surpressed due to confidentiality

was determined with some inaccuracies. The choice of the subwoofer was made with the help of the Thiele-Small-Parameter [JBL]. These contain values for the maximum stroke of the oscillating coil as well as for a force factor B_L. The force factor indicates which force the oscillation coil can apply for a specific current intensity. This is also evident from the unit of the force factor:

$$[B_L] = Tm = \frac{N}{Am} \cdot m = \frac{N}{A} \tag{6.2}$$

Relevant Thiele-Small parameters of the selected subwoofer are shown in table 6.1.

Table 6.1: Thiele-Small-Parameter of the selected subwoofer [JBL]

Name	Symbol	Unit	Value
Moved mass	m	g	155,00
Force Factor	B_L	Tm	13,90
Maximum stroke	X_max	mm	10,25

With a maximum hub $X_{max} = 10.25mm$ it is a long-stroke subwoofer whose deflection is sufficient for the desired deflection of 4 mm even without maximum permissible current. From the force factor $B_L = 13.90N/A$ it is possible to calculate which current is necessary for the applied force $F = 30N$:

$$I = \frac{F}{B} = \frac{30N}{13,9N/A} \approx 2,16A \tag{6.3}$$

This current is below the maximum permissible current of the subwoofer. The frequencies of the selected subwoofer are below 175 Hz, which corresponds to speeds of up to 10500 rpm and thus lies within the range of engine speeds, which are to be investigated.

In summary, the subwoofer fulfills the criteria which are important for the experiment setup. The frequency of the membrane deflection is controllable via the voltage frequency and reaches the frequencies interesting for the carburetor operation. In addition, the deflection and force of the oscillating coil can be adjusted via the current intensity, as a result of which the pressure amplitude in the pressure vessel can be varied. The maximum deflection and the attainable force are sufficiently large. A frequency generator and a powerful amplifier must be connected to the subwoofer in order to be able to adjust the current intensity and the frequency of the voltage at will. With the frequency generator, the temporal progression of the current intensity can be adjusted as desired. Only sinusoidal vibrations are to be generated within this work. For further investigation, however, there is the possibility to program any oscillating forms on the frequency generator. This could,

for example, be used to achieve the actual pressure profile in the intake duct as shown in Figure 6.3.

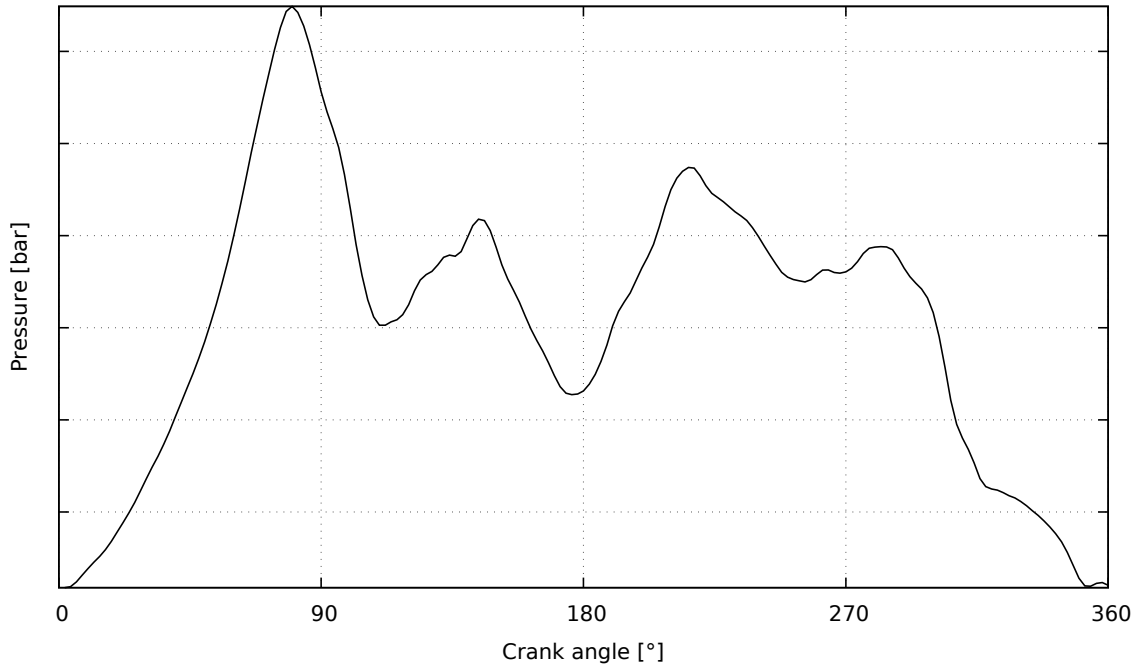

Figure 6.3: Example for the pressure profile in the intake duct at 8000 rpm (pressure values surpressed due to confidentiality)

The subwoofer concept has already been implemented during this work. For this purpose, some components for connecting the subwoofer with the membrane of the pressure vessel were designed and manufactured. The built-in subwoofer on the test stand is shown in Figure 6.4.

Some test runs with the modified structure have already been carried out. The pressures shown in figure 6.5 were measured on the sensors *1* and *2* for the presetting of $10Hz$ on the frequency generator and a voltage amplitude of $9V$.

The frequency corresponds precisely to the predetermined frequency of 10 Hz. The pressure values are shown over a period of 500 ms. Five exact periods can be seen. A pressure amplitude of ±[redacted]* mbar is recorded for the *Sensor 2*, which is directly on the retainer side of the valve, which corresponds to the desired amplitude. In addition, the set operating point could be kept constant for any length of time. This makes the test bed very suitable for future measurements with higher frequencies.

*Information surpressed due to confidentiality

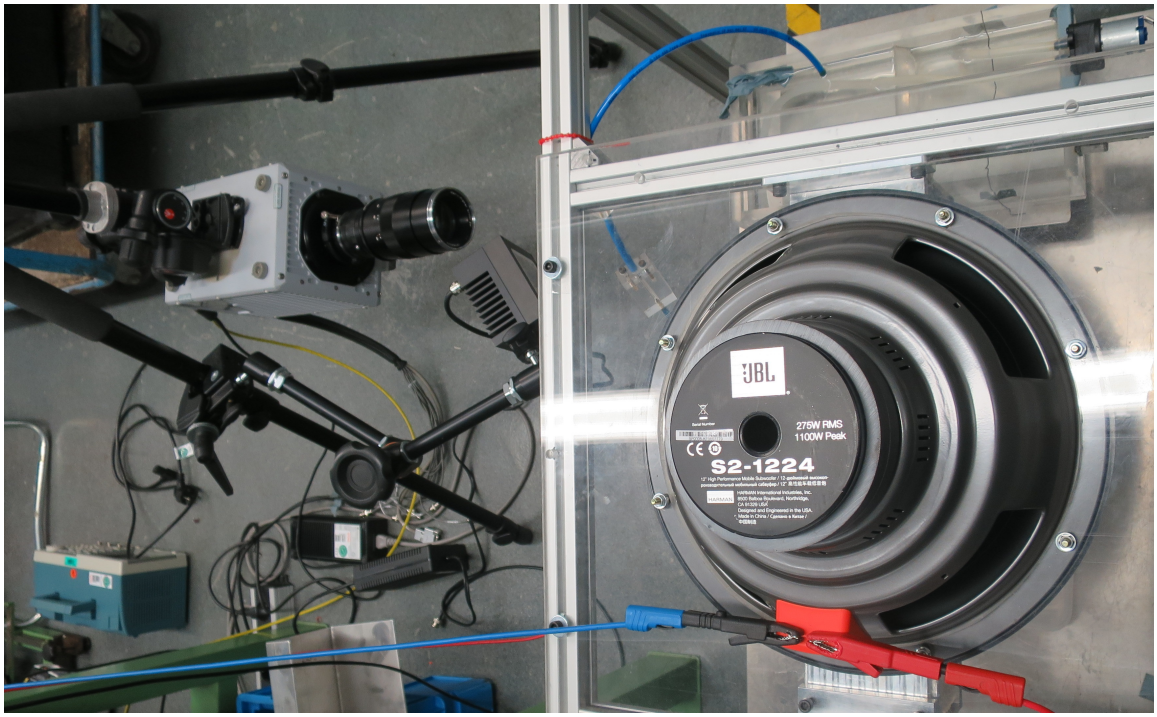

Figure 6.4: Subwoofer built onto the test bed

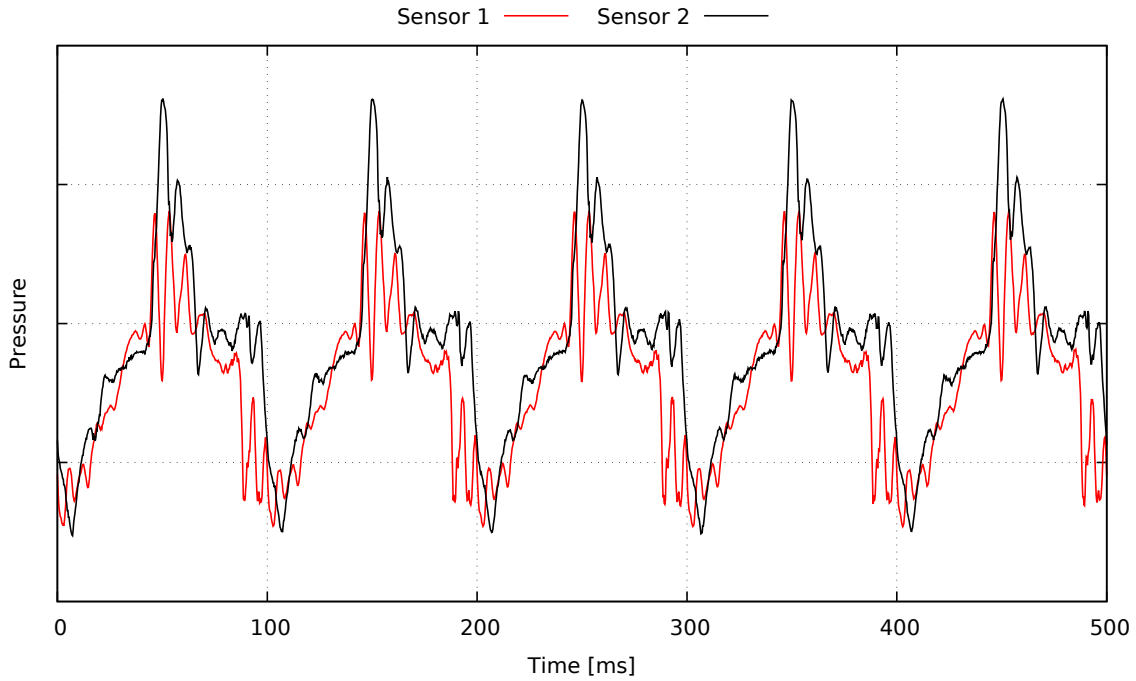

Figure 6.5: Measured pressure profiles with the subwoofer on the test bed at a frequency of 10 Hz (values surpressed due to confidentiality)

6.3 Further development of the 1D model

In order to improve the quality for the one-dimensional calculation of the disc behavior, there is a development approach. The 3D calculations show that there are three significant zones of different pressures on the disc side facing the valve seat. The interior extends to the inner radius of the valve seat bead, a transition zone from the inner radius to the outer radius of the valve seat bead, and a third zone from the outer radius of the valve seat bead to the outer radius of the disc. On the side facing the retainer, on the other hand, a constant pressure is applied over the entire radius of the disc in a good approximation. This is shown again in the figure 6.6.

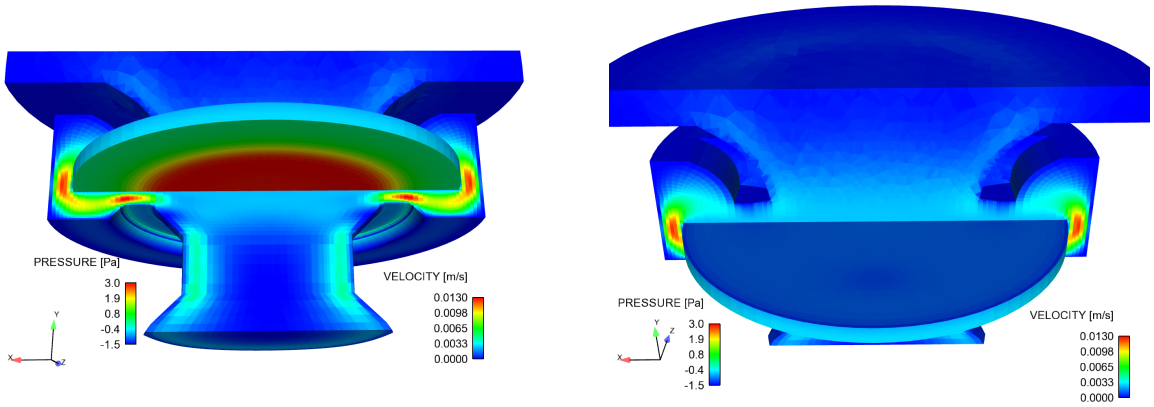

(a) Side facing the valve seat

(b) Side facing the retainer

Figure 6.6: Pressure distribution on the disc derived from 3D simulation

In the 1D model, on the other hand, only two zones of different pressure are connected to the disc as shown in Figure 6.7. Thus, for the inner part of the transition zone, the same pressure $p_{Ventilraum1}$ is assumed which acts on the inner zone. For the outer part of the transition zone, however, the pressure $p_{Ventilraum2}$ is assumed, which acts on the outer zone. This represents a strong simplification, which only very roughly reflects the pressure conditions on the disc.

In order to investigate whether a finer division of the disc is meaningful, the pressure in the elements *Ventilraum1*, *Dichtung1*, *Dichtung2* and *Ventilraum2* is considered. By way of example, in the figure 6.8, the pressure profile of these elements over one revolution is represented as the boundary conditions $BC1$ and $BC2$ for the calculation with the pressure measurement values from *Experiment 3*.

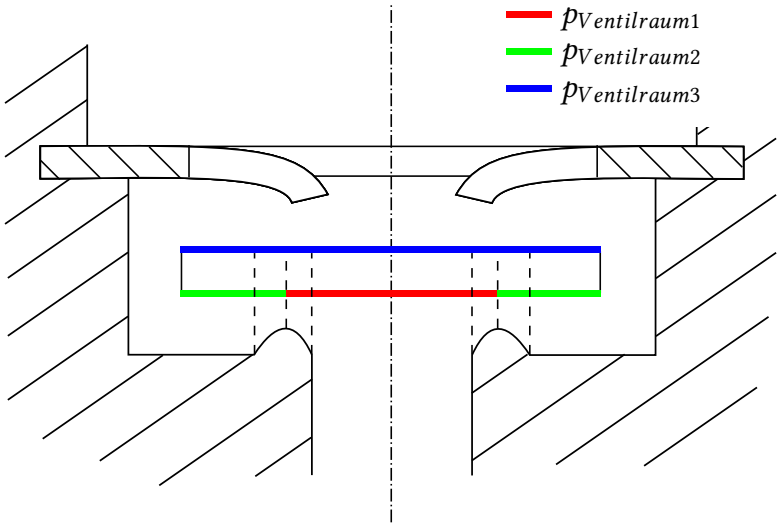

Figure 6.7: Pressure distribution on the disc in 1D model

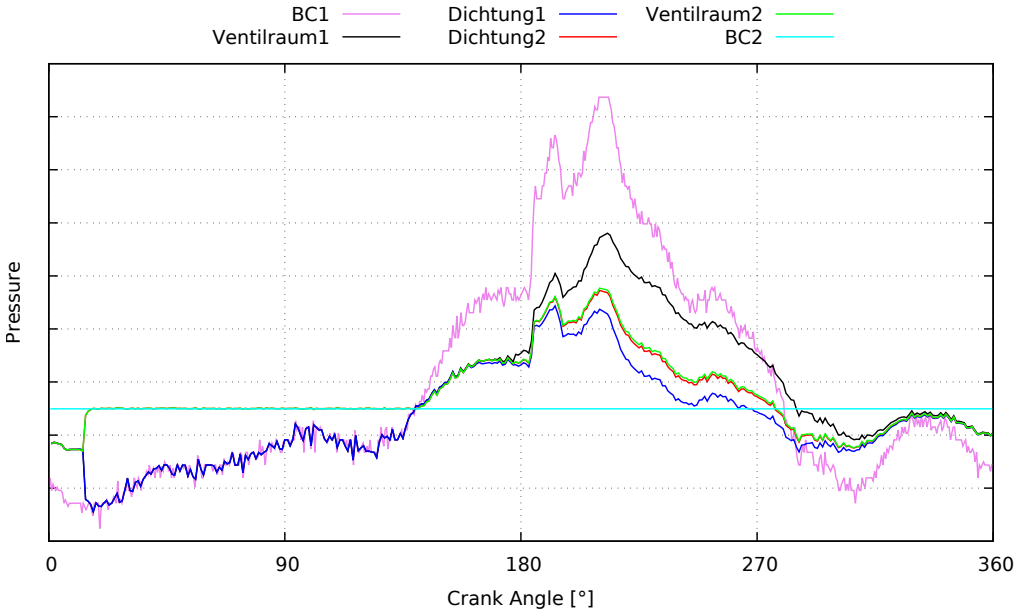

Figure 6.8: Pressures in elements *Ventilraum1*, *Dichtung1*, *Dichtung2* and *Ventilraum2* in the 1D simulation for *Experiment 3* (values surpressed due to confidentiality)

The pressure in *Dichtung2* and *Ventilraum2* is approximately the same at all times with a relative deviation of 0.03%, the curves are nearly congruent. For the pressure in *Dichtung2* the pressure from *Ventilraum2* can therefore be assumed in good approximation. However, the other two elements show significant pressure differences. These two elements *Ventilraum1* and *Dichtung1* differ significantly from each other. From this it can be concluded that a division into three zones according to figure 6.9 could be useful.

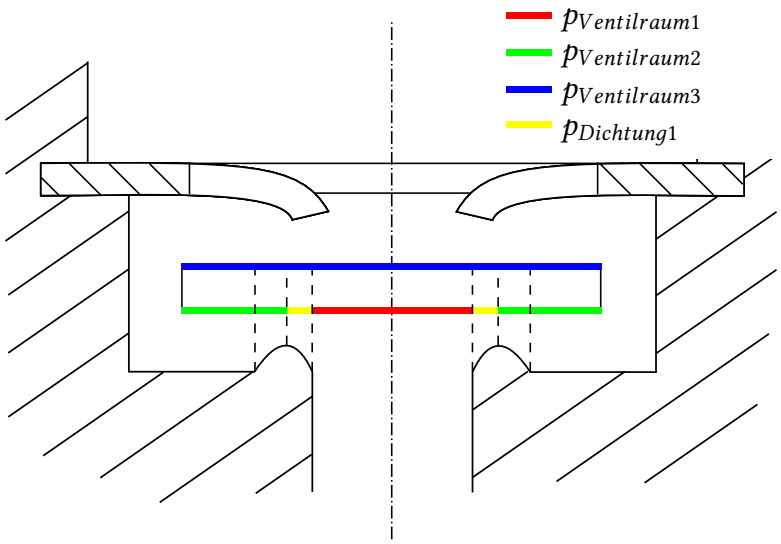

Figure 6.9: Aspired pressure distribution on the disc in a new 1D model

The effect of a finer discretization is also shown in a study using a stationary 3D simulation with the pressure difference of 300 Pa across the valve. For this purpose, the pressures are distributed according to the 1D model in Figure 6.10 and spatially averaged.

These average pressures are applied to the disc in two different ways as a compressive force. The calculation method with *2 zones* calculates the pressure force as the current 1D model by the pressure from the *Ventilraum1* acting on the inner part of the plate and the pressure from the *Ventilraum2* on the outer part. The compressive force is thus calculated as in DAVE+ from

$$F_{2Zones} = (p_{Ventilraum1} - p_{Ventilraum3}) \cdot (A_1 + A_2) + (p_{Ventilraum2} - p_{Ventilraum3}) \cdot (A_3 + A_4) \quad (6.4)$$

In the calculation type with *4 zones*, the disc is divided into four areas. The pressure from *Ventilraum1* is again applied to the innermost part, and the pressure from the *Ventilraum2* to the outermost part. In between, however, there are two circular surfaces on which the pressures of *Dichtung1* and *Dichtung2* act in this calculation. Thus, the compressive force is calculated

$$\begin{aligned} F_{4Zones} = {} & (p_{Ventilraum1} - p_{Ventilraum3}) \cdot A_1 + (p_{Dichtung1} - p_{Ventilraum3}) \cdot A_2 \\ & + (p_{Dichtung2} - p_{Ventilraum3}) \cdot A_3 + (p_{Ventilraum2} - p_{Ventilraum3}) \cdot A_4 \end{aligned} \quad (6.5)$$

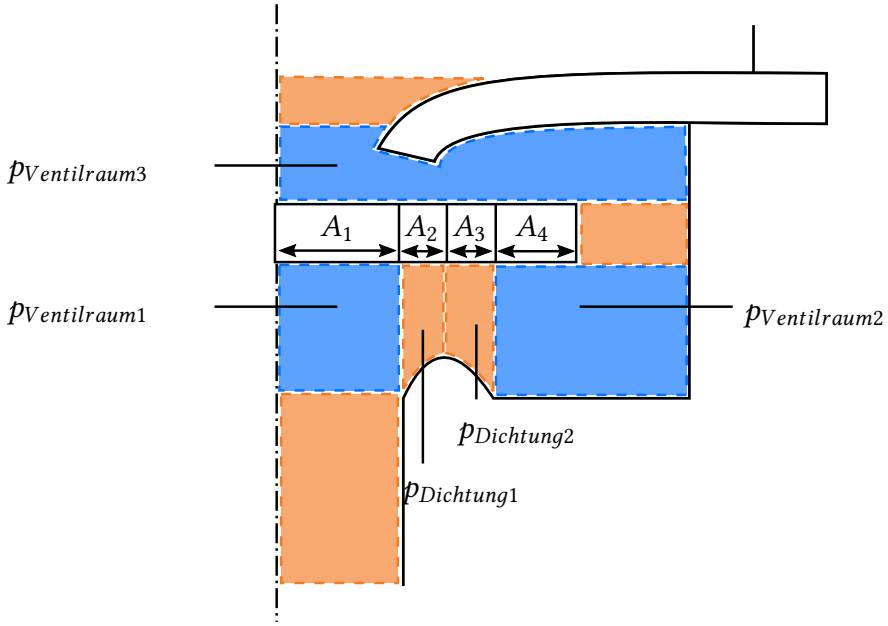

Figure 6.10: Disc division in the 1D model

With these two forces, the closing movement of the disc is calculated and compared with the closing movement from the 3D calculation. This comparison is shown in Figure 6.11.

This shows that the 2-zone calculation leads to a much faster closing movement than the calculation with 4 zones or and the 3D simulation. The calculation with 4 zones, on the other hand, shows a high agreement with the 3D calculation.

Within the scope of this work it was already strived to implement such a finer discretization on the disc. The challenge is that pipes in DAVE+ can not be connected to elastic walls. For this reason, a third elastic wall can not be simply created and connected to the pipe *Dichtung1*. For this, a programming effort with intervention on the code of the flow solver would be necessary. There are two different approaches to avoid this. The pressure in *Dichtung1* can be accessed at any time. Thus, the first approach is to multiply this pressure by the corresponding area A_{Z1} on the disc and apply this as an external force $F = p_{Dichtung1} \cdot A_{Z1}$ to one of the two existing disc parts. The second approach is to create a boundary condition RB_3, which accesses the pressure from *Dichtung1*, and connects it to a third elastic wall.

Both of these approaches, however, lead to numerical problems so that DAVE+ can not perform the calculation with these models. This is due to the calculation method in DAVE+.

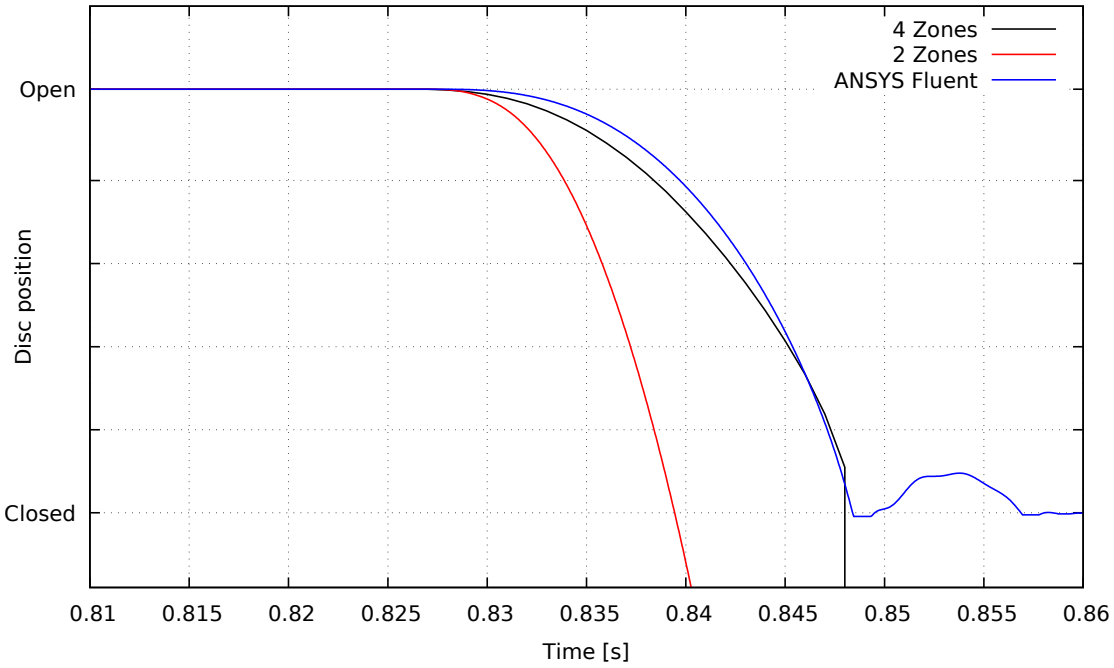

Figure 6.11: Closing movement from 3D simulation compared to analytically calculated closing movement with both the 2 zones and the 4 zones division for a stationary pressure difference from 300 Pa across the valve (values surpressed due to confidentiality)

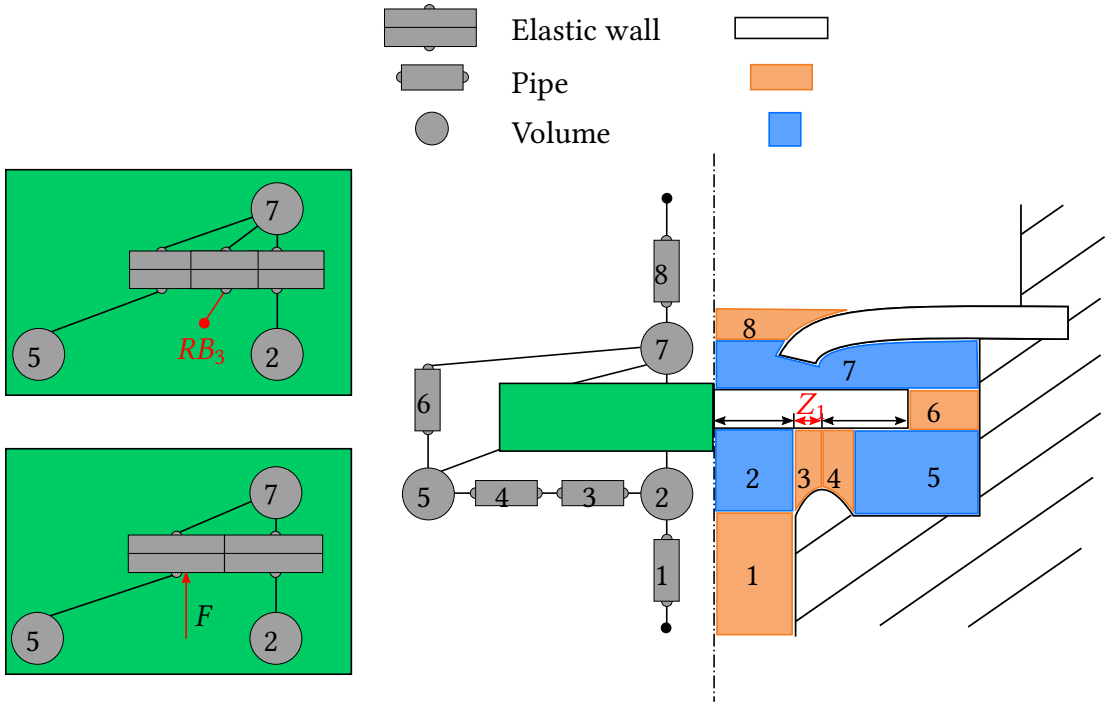

Figure 6.12: pressure from *Dichtung1* as boundary condition or external force

As an example, let us refer again to the through-flow of the aperture from chapters 2.2.3, for which the following discretized, one-dimensional conservation of momentum results.

$$\frac{\mathrm{d}w_c}{\mathrm{d}t} = \frac{1}{\rho_c}\left[-\frac{p_r - p_l}{\delta x_{lr}} + f\right] - \frac{1}{2}\frac{w_r^2 - w_l^2 - sign(w_c)\xi w_c^2}{\delta x_{lr}} + g \tag{6.6}$$

DAVE+ is programmed to convert the equation in a way that the sought quantities p_r and p_l are on the left side, while all other terms are on the right side of the equation. An external force or boundary condition is introduced by the term f. If, then, one of the pressures to be solved is at the same time a component of such an external force or boundary condition, it remains on the right side instead of on the left side of the equation on which the pressures should actually be. This results in DAVE+ obtaining a non-solvable equation system.

In order to make possible a more subtle discretization, it is considered to change the source code of DAVE+ in such a way that pipes can be connected to elastic walls. If this is implemented in the future, the finer discretization should be implemented and investigated by connecting *Dichtung1* to a third wall element. It is to be expected that this change in the disc leads to a changed opening and closing speed and thus also has an influence on the mass flow.

7 Summary

The aim of the present work is to gain a better understanding of the processes in check valves and to transfer this into a one-dimensional model. To understand the purpose and tasks of the check valves considered, the *principles* of the function of the combustion engines are summarized. The focus is on the two-stroke engines of hand-held work equipment. Within the STIHL company, membrane carburetors are usually installed, which in turn contain check valves. The structure and operation of these carburetors and check valves are also described in the chapter *principles*. Since the check valves are described in a one-dimensional replacement model, this chapter also contains the basics of the STIHL internal simulation software DAVE+ used.

In this software a model for the check valves is implemented, which is described in the chapter *One-dimensional Model*. After the detailed description of the model, some numerical tests are carried out, which prove the function of the model. However, difficulties arise with the periodicity of the simulation results, which are remedied by the installation of a simple mass oscillator. The structure and the effects of this oscillator are explained in this chapter.

Parallel to this, various investigations are carried out on a test bed for the validation of the model. The structure of this test bed as well as the measurement instrumentation used are described in the chapter *Experimental Investigation*. Both the procedure for the evaluation of the tests as well as their results are also contained in this chapter. Some measurements already correspond to the conditions of the carburetor. The test bed itself, however, has some weaknesses, which are also discussed in chapter 4.

The validation of the one-dimensional model is described in the corresponding chapter *Validation*. For this purpose, in addition to measurements at the test bed, 3D flow simulations are used, which are therefore described at the beginning of the chapter. In order to ensure good comparability between 1D and 3D calculations, a geometric and flow-mechanical matching is necessary, which is therefore also described. Subsequently

the *stationary* and *periodic-stationary* matched 1D model are compared to corresponding 3D simulations on the basis of further calculations. The 1D model provides both qualitative and quantitative good results. This shows that the 1D model is already able to deliver important insights that so far had to be acquired with time and cost-intensive 3D simulations. The subsequent comparison of measurements and 1D simulations also shows a good qualitative agreement. However, large quantitative differences become clear, especially in the calculation of the mass flow. In order to determine the cause of this, some analytical and experimental investigations are carried out, which however can not conclusively explain the deviations.

Finally, the discussion of possible causes leads to the development, construction and implementation of a new test bed concept for future measurements. This is described in the chapter *Conclusion and Outlook*. Initial experiments are already being carried out and the principle function of the concept is demonstrated. Additionally, some potential improvements of the 1D model are described. An implementation of this is partly already pursued within this work. However, a revision of the simulation software DAVE+ is necessary in order to be able to include it in the 1D model.

Bibliography

[Bas15] R. van Basshuysen. *Handbuch Verbrennungsmotoren*. 7th ed. Wiesbaden: Springer Vieweg, 2015.

[BD16] S. Brandt and D. Dahmen. *Schwingungen und Wellen - Phänomene in Mechanik und Elektrodynamik*. 1st ed. Wiesbaden: Springer Fachmedien, 2016.

[BE05] W. Bohl and W. Elmendorf. *Technische Strömungslehre; Stoffeigenschaften von Flüssigkeiten und Gasen, Hydrostatik, Aerostatik, Inkompressible Strömungen, Kompressible Strömungen, Strömungsmesstechnik*. 13th ed. Würzburg: Vogel Buchverlag, 2005.

[Han12] C. Hankh. "Simulation von inkompressiblen Rohrströmungen unter Berücksichtigung von Beschleunigungen". STIHL-interner Bericht. 2012.

[Hei16] J. Heintze. *Lehrbuch zur Experimentalphysik Band III: Elektrizität und Magnetismus*. 1st ed. Berlin Heidelberg: Springer, 2016.

[JBL] JBL. *S2-1024/S2-1224 Owner's Manual*. Harman Betriebsanleitung 2015.

[Jr17] H. Oertel Jr. *Prandtl - Führer durch die Strömungslehre*. 14th ed. Wiesbaden: Springer Vieweg, 2017.

[KF06] E. Köhler and R. Flierl. *Verbrennungsmotoren*. 4th ed. Wiesbaden: Vieweg & Sohn Verlag, 2006.

[Lag16] P. Lagaly. "Untersuchung des Betriebsverhaltens von 2-Takt-Ottomotoren". Skript zum *Motorenlabor* am Karlsruher Institut für Technologie (KIT). 2016.

[Lec14] G. Leccese. "Entwicklung eines 1D-Ersatzmodells für kompressible Gasblasen in einem inkompressiblen Fluid mit Hilfe einer schwingenden Membran". STIHL-interner Bericht. 2014.

[MS12] G. P. Merker and C. Schwarz. *Grundlagen Verbrennungmotoren; Funktionsweise, Simulation, Messtechnik*. 6th ed. Wiesbaden: Vieweg+Teubner, 2012.

[Pis02a] S. Pischinger. *Verbrennungsmotoren Band I*. Vorlesungsskript Rheinisch-Westfälische Technische Hochschule Aachen (RWTH Aachen). 2002.

[Pis02b] S. Pischinger. *Verbrennungsmotoren Band II*. Vorlesungsskript Rheinisch-Westfälische Technische Hochschule Aachen (RWTH Aachen). 2002.

[RK13] M. Rieber and R. Köhli. "Mathematische und physikalische Grundlagen von Dave". 2013.

[SA06] J. H. Spurk and N. Aksel. *Strömungslehre: Einführung in die Theorie der Strömungen*. 8th ed. Heidelberg/Dordrecht/London/New York: Springer, 2006.

[Wik] Wikimedia Foundation Inc. *Lautsprecher*. upload.wikimedia.org/wikipedia/commons/3/3c/Lautsprecher_Schema.svg, Zugriff: 17.05.2017.